

Influence of modifiers on Palladium based nanoparticles for room temperature formic acid decomposition

By

Simon Philip Jones

197711

Balliol College

A dissertation submitted for the degree of Doctor of Philosophy at the Inorganic Chemistry Laboratory, Department of Chemistry, University of Oxford

2013

Influence of modifiers on Palladium based nanoparticles for room temperature formic acid decomposition

By

Simon Philip Jones

197711

Balliol College

Supervisor

Professor S. C. E. Tsang

Internal Assessor

Professor J. S. Foord

A dissertation submitted for the degree of Doctor of Philosophy at the Inorganic Chemistry Laboratory, Department of Chemistry, University of Oxford

2013

Table of Contents

Table of Contents i
Declaration v
Dedication vi
Acknowledgements vii
Abstract ix
List of figures xi
List of abbreviations and symbols xiv
List of publications xvi
Chapter 1 Introduction 1
1.1 Catalysis 2
1.2 Theory of catalysis 7
1.3 Computational methods 15
1.4 Nanoparticle catalysis 18
1.4.1 Electronic effects 19
1.4.2 Geometric effects 25
1.4.3 Metal support interaction 35
1.5 Formic acid 38
1.5.1 Formic acid cycle 40
1.5.2 Formic acid synthesis 41
1.5.3 Formic acid decomposition 43
1.5.4 Decomposition mechanism 45
1.5.5 Developments in heterogeneous decomposition 49

1.6 Aims and objectives 53
1.7 Thesis overview 54
1.8 References 56
Chapter 2 Analytical Techniques 63
2.1 Introduction 64
2.2 X-ray powder diffraction 65
2.3 X-ray photoelectron spectroscopy 68
2.4 Thermogravimetric analysis 70
2.5 Transmission electron microscopy 71
2.6 Energy-dispersive x-ray spectroscopy 73
2.7 Pulse chemisorption 74
2.8 Fourier transform infrared spectroscopy 76
2.9 References 79
Chapter 3 Experimental and Characterisation Methods 80
3.1 Synthesis of colloidal nanoparticles 81
3.1.1 PVP stabilised nanoparticles 81
3.1.2 Non-PVP stabilised nanoparticles 82
3.1.3 Decoration of colloidal nanoparticles 84
3.2 Synthesis of functionalised supports 84
3.3 Synthesis of supported palladium catalysts 85
3.3.1 Polymer modification of Pd/C 85
3.3.2 Synthesis of supported palladium 85
3.3.3 Decoration of supported palladium 86
3.4 Characterisation 86
3.4.1 XRD 86

3.4.2 XPS 87
3.4.3 TGA 88
3.4.4 TEM/EDX 88
3.4.5 FTIR 88
3.4.6 CO chemisorption 89
3.5 Catalyst testing 89
3.6 Computational details 90
3.6.1 DFT calculations 90
3.6.2 XRD simulation 91
3.7 References 92
Chapter 4 Polymer Modification 94
4.1 Background 95
4.2 Objectives 97
4.3 Experimental details 98
4.4 Results and discussion 99
4.4.1 Colloidal synthesis method 99
4.4.2 Polymer stabilised palladium colloids 108
4.4.3 Polymer modified supported palladium 116
4.5 Conclusion 130
4.6 References 131
Chapter 5 Support Modification 135
5.1 Background 136
5.2 Objectives 138
5.3 Experimental details 139
5.4 Results and discussion 140

5.4.1 Silica functionalisation 140
5.4.2 Silica supported palladium..... 145
5.4.3 Alumina functionalisation..... 153
5.4.4 Alumina supported palladium..... 159
5.5 Conclusion..... 166
5.6 References 167
Chapter 6 Metal Decoration..... 170
6.1 Background 171
6.2 Objectives..... 173
6.3 Experimental details..... 174
6.4 Results and discussion 174
6.4.1 Decorated colloidal palladium..... 174
6.4.2 Bismuth decorated colloidal palladium 184
6.4.3 Silver decorated colloidal palladium 191
6.4.4 Silver decorated supported palladium 195
6.5 Conclusion..... 203
6.6 References 205
Chapter 7 Conclusions and Future Perspectives..... 208
7.1 Conclusions 209
7.2 Future perspectives 210
7.3 References 211

Declaration

I confirm that this is my own work and the use of all material from sources has been properly and fully acknowledged.

Simon Philip Jones

Dedication

To my family.

Acknowledgements

First and foremost, I would like to thank Professor Edman Tsang for his support and guidance throughout the course of my DPhil. project. Additionally I would like to thank him, the University of Oxford and the Engineering and Physical Sciences Research Council for providing me with the opportunity to undertake this project and for the provision of facilities and funding.

The research presented in this thesis would not have been possible without the training and assistance I received throughout the project. I would like to thank Dr Nick Rees, Dr Phil Wiseman and Dr Neil Young for their training in and assistance with NMR, XRD and TEM, respectively. Extensive training in the synthesis of nanoparticles and the use laboratory based characterisation equipment (such as FTIR, gas chromatography and TGA), used within this thesis was provided by Dr Kai Man Kerry Yu and Dr Karaked Tedsree. I must also thank Jin Qu for performing DFT calculations and aiding the analysis and discussion of the results. My gratitude must be expressed to Dr Jingping Hu and Ashley Shepherd for performing XPS experiments and assisting with the analysis of the results provided. Along with all of these people who trained and aided my understanding in scientific techniques, I must also give great thanks to the staff of the inorganic chemistry department, who assisted me with solving the administrative and facilities problems faced along the way, and the staff of the ICL stores who facilitated the procurement of all the materials used throughout this work.

I would also like to thank all the members of the Tsang research group, past and present, who aided and supported my work throughout my time as part of the group. I would like to especially thank Amy Kolpin and Dr Aaron Chan for assistance with TEM and Dr Simon

Fairclough for assistance with TEM and XRD modelling, and express my gratitude to them all for in depth discussions pertaining to this work. Furthermore, I need to express my gratitude to Hanif Mahadi, Clive Eley, Cheng-Tar Wu, Ieuan Ellis, Alexander Gilchrist, Richard Dear, Ian Coulter and Jamie Wolstenhulme for general discussion, assistance and entertainment they provided throughout my time in Oxford. Thanks must also go to the Part II students that I supervised during this project, particularly Maxwell Gordon-Brown for extensive collaboration in the work on metal decoration of Pd nanoparticles.

Abstract

Heterogeneous catalysts form a highly important part of everyday life, ranging from the production of fertiliser enabling the growth of crops that sustain much of the world's population to the production of synthetic fuels. They constitute a key part of the chemical industry and contribute towards substantial economic and environmental benefits. Heterogeneous catalysts are also believed to have an important role to play in a future hydrogen economy, reducing our requirements for fossil fuels. To this end, formic acid has been proposed as a potential hydrogen storage material for small portable devices. Additionally, formic acid has historically been used as a probe molecule to study catalyst materials and recent developments in the knowledge of its decomposition pathways and the preferred sites of these reactions, establish a good foundation for further study. This work explores a range of novel modification techniques that alter the activity of Pd nanoparticles to decompose formic acid to H_2 and CO_2. The methods used are the addition of polymers, attaching various functional groups to the surface of the catalyst support and decoration of nanoparticles with sub-monolayer coverages of another metal. Using a range of characterisation methods including FTIR of an adsorbed CO probe, XRD and XPS coupled with computational modelling, it is found that these methods result in some significant electronic and/or geometric alterations to the Pd nanoparticles. For polymer modification, the nature of the pendent group is highly important in determining the effects of the polymer on the Pd particles, with all the tested polymers resulting in varying degrees of electronic donation to the Pd surface. The geometric modifications caused by the polymers also varied with pendent groups; with amine containing pendent groups found to selectively block low coordinate sites, preventing the undesired dehydration of formic acid which results in poisoning of the Pd catalyst by the resulting CO. Attachment of amine groups to the surface

of metal oxide catalyst supports, is demonstrated to result in dramatic electronic promotional effects to the supported Pd nanoparticles, and when an amine polymer is attached to the support surface the geometric modification is again observed.

Finally decoration of Pd nanoparticles with a sub-monolayer coverage of a second metal is examined, resulting in some similar electronic and geometric effects on Pd nanoparticle surfaces to those observed with polymer modification with corresponding changes in formic acid decomposition activity. Overall, a number of methods are displayed to tune the catalytic activity and selectivity of Pd nanoparticles for formic acid decomposition, resulting in catalysts with some of the highest reported TOF's at room temperature. These modification methods are believed to be potentially applicable to a wide range of other catalytic reactions that operate under mild conditions.

Keywords: Heterogeneous catalyst, Geometric modification, Electronic modification, Formic acid dehydrogenation, Selective decomposition, Hydrogen production.

List of figures

Figure 1.1– Reaction profile of the catalysed and un-catalysed synthesis of ammonia from the elements. Modified from reference[34] 8
Figure 1.2– Volcano plot of formic acid conversion temperature against enthalpy of formation of the metal formate. Reproduced from reference[4] 10
Figure 1.3– A schematic of slab and cluster representations of H_2 on a surface. Shaded and un-shaded circles show atoms in super cell and in repeating cells, respectively. Small circles are H_2. Reproduced from reference[44] 16
Figure 1.4– Effect of CO coupling to a transition metal d-band. Reproduced from reference[61] 20
Figure 1.5– Variation of Pd $3d_{5/2}$ binding energy on changing particle size, with respect to bulk Pd. Reproduced from reference[65] 21
Figure 1.6– Illustration of some common bimetallic structures; (a) core-shell, (b) heterojunction, (c) alloy. Reproduced from reference[69] 23
Figure 1.7– (a) Model cubo-octahedron reproduced from reference[60]; (b) calculated % of sites (corner, edge, terrace, and total surface sites) with respect to the total number of atoms for different size Pd cubo-octahedron 27
Figure 1.8– TOF of different size Pd particles for the activity of allyl alcohol hydrogenation, normalised by the fraction of different surface sites. Reproduced from reference[59] 28
Figure 1.9– (Left) MCP reactions. (Right) dependence of the MCP reaction products on Pt particle shape. Modified from reference[74] 31
Figure 1.10– Schematic diagram of a hydrogen PEM fuel cell. Reproduced from reference[91] 39
Figure 1.11– Hydrogen storage cycle based on formic acid/carbon dioxide[90] 41
Figure 1.12– Bridging and monodentate binding modes of formate from dissociative adsorption of formic acid on a transition metal surface 46
Figure 2.1– Schematic diagram of constructive interference from a crystalline structure. Modified from reference[10] 66
Figure 2.2– Schematic diagram of the photoelectric emission of a core 1s electron. Reproduced from reference[7] 68
Figure 2.3– Schematic of TGA Q50[11] 71
Figure 2.4– Typical pulse chemisorption spectra 74
Figure 2.5– Schematic of an ATR crystal with multiple internal reflections. Reproduced from reference[7] 78
Figure 3.1– Structures of polymer monomers used to stabilise colloidal Pd nanoparticles and to modify type 87L 83
Figure 4.1– Schematic diagram of colloidal nanoparticles stabilised with (a) ligands and (b) polymer. Modified from references [9] and [1] respectively 96
Figure 4.2– XRD pattern of Pd-PVP 1:10, reduced by ethylene glycol and ICDS peaks of Pd^0 and $Pd(NO_3)_2$, red and green lines respectively 100
Figure 4.3– Activity plot of Pd-PVP 1:10 reduced by ethylene glycol at 120°C, $0.15x10^{-3}$ moles of Pd in 15.86 mL 1.4 M formic acid at 25°C 103
Figure 4.4– Illustration of the reaction mechanism of formic acid decomposition on different Pd surface sites. Reproduced from reference[23] 105
Figure 4.5– FTIR of CO adsorbed on Pd-PVP 1:10 reduced by different methods 106
Figure 4.6– FTIR of Pd-PVP synthesised by ethylene glycol reduction (red) and NaBH4 reduction (green). Black stars indicate boron species 107

Figure 4.7– FTIR of CO adsorbed on polymer stabilised Pd nanoparticles, with a 1:15 ratio. Normalised by CO bridging peak 113
Figure 4.8– Calculated stable binding modes of polymer pendent groups and their energy of adsorption (E_{ads}). N.D=Not determined 114
Figure 4.9– XRD of type 87L as received, type 87L reduced at room temperature and type 39 (PdO/C). Triangles mark peaks of a support impurity 118
Figure 4.10– Widescan XPS spectra of reduced type 87L 119
Figure 4.11– TEM micrograph and size distribution histogram of type 87L Pd/C 120
Figure 4.12– XPS spectra of type 87L and type 87L modified PAAmine, using a 1:5 ratio of Pd to PAAmine monomer unit 124
Figure 4.13– Calculated d-band density of states for Pd(111) and amine modified Pd(111) 125
Figure 4.14– Activity plot of PAAmine modified type 87L. 4.25 mg of Pd stirred in 10.575 mL of 1.4 M formic acid at 25°C 127
Figure 5.1– Schematic of silane functionalised surface with and without water. Modified from reference[17] 140
Figure 5.2– TGA of SiO_2 and (3-aminopropyl)trimethoxysilane functionalised SiO_2 with and without the addition of water 142
Figure 5.3– FTIR of SiO_2 and functionalised SiO_2 144
Figure 5.4– XRD of 5% Pd on silica and position of Pd metal peaks from ICSD 146
Figure 5.5– TEM micrograph of 5% Pd/SiO_2 and size distribution histogram 147
Figure 5.6– TEM micrograph of 5% Pd/SiO_2+3Amine+H_2O and size distribution histogram 147
Figure 5.7– Activity plot of 5% Pd on silica supports, 4.25 mg of Pd stirred in 10.575 mL of 1.4 M formic acid at 25°C 149
Figure 5.8– FTIR of CO adsorbed on Pd-PVP with ethylamine or triethylamine. Intensity normalised by bridging CO peak 151
Figure 5.9– Quantity of acidic -OH groups of the surface. Modified from reference[14] 154
Figure 5.10– TGA of γ-alumina and γ-alumina treated in water or NaOH 155
Figure 5.11– Mechanism of GLPTMS coupling to surface hydroxyl species and subsequent reaction with an amine group of PEI. Modified from reference[15] 158
Figure 5.12– XRD pattern of γ-Al_2O_3 and 5% Pd/γ-Al_2O_3 159
Figure 5.13– TEM micrograph and size distribution histogram of 5% Pd/γ-Al_2O_3 160
Figure 5.14– TEM micrograph and size distribution histogram of 5% Pd/γ-Al_2O_3+3Amine+H_2O 160
Figure 5.15– Activity plot for formic acid decomposition of a range of supported Pd catalysts. 4.25 mg of Pd stirred in 10.575 mL of 1.4 M formic acid at 25°C 165
Figure 6.1– TEM micrograph and size distribution histogram of Pd-PVP 1:10 175
Figure 6.2– Model cubo-octahedral nanoparticle reproduced from reference[19] 176
Figure 6.3– FTIR of CO adsorbed on Pd-PVP decorated with a 1:0.15 molar ratio of group 11 metals 178
Figure 6.4– FTIR of CO adsorbed on Pd-PVP decorated with a 1:0.15 mole ratio of Sn and Co 180
Figure 6.5– FTIR of CO adsorbed on Pd-PVP decorated with a 1:0.15 mole ratio of Te and Bi 181
Figure 6.6– Activity plot of Pd-PVP decorated with 1:0.15 molar ratios of Ag, Bi, and Te. $0.15x10^{-3}$ moles of Pd in 15.860 mL of 1.4 M formic acid stirred at 25°C 182
Figure 6.7– Position of the (111) peak for Pd-PVP, decorated Pd-PVP+Bi particles and the calculated position of the (111) peak for PdBi alloys 185
Figure 6.8– TEM micrograph and EDX spectrum of Pd-PVP+Bi 1:0.60 186
Figure 6.9– FTIR of CO adsorbed on Pd-PVP decorated with various ratios of Bi 188

Figure 6.10– Schematic of the electronic effects at different levels of Bi decoration on Pd nanoparticles. Grey, yellow and turquoise atoms represent Pd, electronically modified Pd, and Bi, respectively 189
Figure 6.11– Total gas production over 2 hours for Pd-PVP decorated with various ratios of Bi. $0.15x10^{-3}$ moles of Pd in 15.860 mL of 1.4 M formic acid stirred at 25°C 189
Figure 6.12– Position of (111) peak for Pd-PVP+Ag particles, with Ag reduced by ethylene glycol at 120°C or N_2H_4 at room temperature, and calculated Pd@Ag core-shell particles 191
Figure 6.13– FTIR of CO adsorbed on Pd-PVP decorated with various ratios of Ag 193
Figure 6.14– Total gas production over 2 hours for Pd-PVP decorated with various ratios of Ag. $0.15x10^{-3}$ moles of Pd in 15.860 mL of 1.4 M formic acid stirred at 25°C 194
Figure 6.15– TEM micrograph and size distribution histogram of 10% Pd/C 196
Figure 6.16– XRD pattern of Pd/C, Ag/C and Pd/C decorated with various ratios of Ag 197
Figure 6.17– Position of Pd(111) peak of Pd/C+Ag particles, Ag(111) peak where present and calculated PdAg alloy (111) 198
Figure 6.18– XPS spectra of Pd 3d region of Pd/C and Ag decorated Pd/C 199
Figure 6.19– Total gas production over 2 hours for Pd/C decorated with various ratios of Ag. 4.25 mg of Pd in 10.575 mL of 1.4 M formic acid stirred at 25°C 200
Figure 6.20– Illustration of Pd particles decorated with Bi, Te and Ag (left to right) 204

List of abbreviations and symbols

Ag/C	Silver nanoparticles supported on carbon
APTMS	(3-Aminopropyl)trimethoxysilane
ATR	Attenuated total reflectance
CCD	Charge-coupled device
CO FTIR	Fourier transform infrared spectroscopy of adsorbed CO
DEAPTMS	[3-(diethylamino)propyl]trimethoxysilane
DFAFC	Direct formic acid fuel cell
DFT	Density functional theory
DoE	Department of energy
DOS	Density of states
E_a	Activation energy
EDX	Energy-dispersive x-ray spectroscopy
E_F	Fermi level
eV	Electron volt
FCC	Face-centred cubic
FID	Flame ionisation detector
FTIR	Fourier transform infrared spectroscopy
ΔG	Change in Gibbs free energy
GC	Gas chromatography
GLYPTMS	(3-glycidoxypropyl)trimethoxysilane
ICL	Inorganic chemistry laboratory
ICSD	Inorganic crystal structure database
IR	Infrared
JM	Johnson Matthey
MCP	Methylcyclopentane
NMR	Nuclear magnetic resonance
PAAcid	Poly(acrylic acid)
PAAmide	Polyacrylamide
PAAmine	Poly(allylamine)
Pd/C	Palladium nanoparticles supported on carbon
Pd/C+M	Metal (M) decorated Palladium nanoparticles supported on carbon

Pd-PVP	PVP stabilised Palladium nanoparticles, similar forms for other polymer stabilised nanoparticles
Pd-PVP+M	Metal (M) decorated PVP stabilised Palladium nanoparticles
PEI	Polyethyleneimine
PEM	Proton Exchange membrane
PSSA	Poly(4-styrenesulfonic acid)
PTM	Post-transition metal
PVP	Polyvinylpyrrolidone
RDS	Rate determining step
R	Gas constant (8.314 J K^{-1} mol^{-1})
SAM	Self-assembled monolayer
SMSI	Strong metal-support interaction
T	Temperature
TCD	Thermal conductivity detector
TEM	Transmission electron microscopy
TGA	Thermogravimetric analysis
TOF	Turnover frequency
XPS	X-ray photoelectron spectroscopy
XRD	X-ray diffraction

List of publications

1. K. Tedsree, C. W. A. Chan, S. Jones, Q. Cuan, W.-K. Li, X.-Q. Gong, S. C. E. Tsang, Science, **2011**, 332, 224-228.

2. K. Tedsree, T. Li, S. Jones, C. W. A. Chan, K. M. K. Yu, P. A. J. Bagot, E. A. Marquis, G. D. W. Smith, S. C. E. Tsang, Nature Nanotechnology, **2011**, 6, 302-307.

3. S. Jones, J. Qu, K. Tedsree, X.-Q. Gong, S. C. E. Tsang, Angewandte Chemie International Edition, **2012**, 51, 11275-11278.

4. S. Jones, S. M. Fairclough, M. Gordon-Brown, J. M. Smith, S. C. E. Tsang, Angewandte Chemie International Edition, **2013**, Submitted

Chapter 1

Introduction

Chapter 1 Introduction 1

1.1 Catalysis 2

1.2 Theory of Catalysis 7

1.3 Computational Methods 15

1.4 Nanoparticle Catalysis 18

1.4.1 Electronic Effects 19

1.4.2 Geometric Effects 25

1.4.3 Metal support Interaction 35

1.5 Formic Acid 38

1.5.1 Formic acid cycle 40

1.5.2 Formic acid Synthesis 41

1.5.3 Formic acid decomposition 43

1.5.4 Decomposition mechanism 45

1.5.5 Developments in heterogeneous decomposition 49

1.6 Aims and Objectives 53

1.7 Thesis Overview 54

1.8 References 56

1.1 Catalysis

The term catalysis was first used by Jons Jacob Berzelius in 1836.[1] He used the term to describe a number of existing experimental observations, such as the decomposition of hydrogen peroxide by transition metal salts and the combustion of hydrogen over spongy transition metals, without the transition metal species undergoing any alteration. This phenomenon was also identified for a range of other reactions in organic, inorganic and biological systems. From these findings he proposed that many substances, in various states, possessed the "power" to promote certain reactions without the substance directly participating in it or necessary for it to occur. This power to promote reactions was designated "the *catalytic power* of bodies" and the decomposition it produced was called "*catalysis*".[1] He also proposed "although still too little known to be accurately explained, [the power] must play a far more important part though-out nature than we have hitherto been led to suppose."

The modern definition of a catalyst is "A substance that increases the rate of a chemical reaction without itself undergoing any permanent chemical change".[2] This definition varies somewhat from its first use, but the idea Berzelius had that catalysis played an important part throughout nature has been shown to be correct, which is highlighted by its increased importance in everyday life.[3] Since the first major breakthrough in industrial catalysis, the use and study of catalysis has expanded dramatically, both in terms of the amount of academic research and its application in industrial processes.[4]

In 1913 the first large scale industrial catalysis process was commercialised, it was the Haber-Bosch process to synthesise ammonia.[5] It involved the reaction of elemental nitrogen and hydrogen over an osmium catalyst, this was soon modified to a much cheaper iron based catalyst which is similar to what is used today.[6] Ammonia is a key material for the

production of fertiliser and the Haber-Bosch process is estimated to be involved in producing fertiliser that sustains a 40% of the world's population and consumes 1% of the world energy.[7,8] BASF who commercialised the Haber-Bosch process and produce a wide range of speciality chemicals - many of which are produced by catalytic processes - has developed into the 69th largest global company valued at $90 billion according to Forbes.[9]

Another historically important catalytic reaction is the Fischer-Tropsch synthesis in which carbon monoxide and hydrogen are converted to hydrocarbons. It was developed in the early 20th century and was used extensively by Germany during World War II, to produce synthetic fuel, due to their limited supply of crude oil.[10] The Fischer-Tropsch reaction typically uses a transition metal catalyst, such as iron or cobalt, with the exact catalyst composition dependent on the ratio of hydrogen to carbon in the feed gas.[11] The Fischer-Tropsch synthesis is still highly important in the petroleum industry as a key step in the conversion of coal or natural gas to sulphur free liquid fuels.[12] Coal and natural gas are converted to synthesis gas ("syngas", $CO + H_2$), and the water gas shift reaction is used to alter the ratio of $CO:H_2$ using steam. This syngas, with the desired ratio of carbon monoxide to hydrogen, can then be used in the Fischer-Tropsch synthesis.[10,12] Through tailoring the reaction conditions and the catalyst, the distribution of hydrocarbon products can be controlled; the Mossgas plant in South Africa produces gasoline and diesel whereas the Shell plant in Malaysia mainly produces waxes.[12]

Along with BASF, a number of other companies that are highly involved in the use and development of catalysts are in Forbes top 100 global companies.[9] As such, the global catalyst industry revenue is forecast to be $91 Billion by 2018, with substantial growth continuing.[13] The development of catalysts for new reactions, improving existing catalysts,

the study of catalytic reaction mechanisms, and the production of reactor systems, has developed catalysis into a wide ranging field that combines engineering, materials science and chemistry.

From the scale of the catalysis industry and the two examples discussed previously, it is clear that catalysis is highly important in our everyday lives. It has become vital to many industries and is heavily involved in food preparation, pollution control, production of inorganic materials, and in the drive for clean energy.[3,4,14] The environmental impact of human life on the earth, especially the effect of chemical processes, led Anastas to propose the concept of "Green Chemistry".[15] He set out twelve principles that give methods and goals to producing more environmentally friendly chemical processes. These principles include waste prevention, the use of catalytic rather than stoichiometric reagents, and energy efficiency by design, as well as a range of other factors. The development of effective catalysts has helped to achieve many of these goals and is seen as an important part of more environmentally friendly chemical processes.[3]

An example of the catalysis community striving to promote green chemistry has been the huge amount of research devoted to the development of hydrogen fuel cells, where the only waste products are water and heat to produce electricity.[16] Hydrogen has been proposed as a new energy storage material and, combined with use in a fuel cell, is proposed to replace traditional transportation fuels, substantially reducing pollution.[17] Hyundai has recently produced the first production car powered by a fuel cell, with performance highly comparable to the same model powered by a combustion engine.[18] Fuel cells are also more efficient than combustion engines, so less energy is wasted.[16]

All of the catalytic reactions mentioned thus far have described processes involving solid catalysts; however catalysis can be divided into three broad areas. These areas are: Biocatalysis, Homogeneous and Heterogeneous.

Biocatalysis is the use of biologically occurring catalysts, such as enzymes or micro-organisms, to perform catalytic reactions. There is much interest in this area, because nature has already developed highly active and selective catalysts for many industrially desirable reactions.[14,19] Such as, the creation of highly enantiomerically pure chiral centres and the conversion of light energy to chemical energy through photosynthesis.[14,19]

Homogeneous catalysis occurs with both catalyst and reactants in the same phase; typically the catalyst is an organometallic compound or a simple acid/base that is used in solution with the reactants and products. An example is the acid-catalysed Fischer esterification, where a carboxylic acid reacts with an alcohol to form an ester; the acid activates the carbonyl, creating a more reactive intermediate.[20] Organometallic catalysts are widely used for selective hydrogenation and polymerization reactions.[21,22] The activity and selectivity of the catalyst is highly dependent on the metal centre and the ligands surrounding it, modification of these ligands can provide a high degree of control over the catalytic properties through electronic or steric effects.[22,23]

Heterogeneous catalysis involves the catalyst and reactants in different phases, typically the catalyst is a solid and the reactant(s) are in the liquid or gas phase.[4] Heterogeneous catalysts are widely used in industrial processes and are often preferred to homogeneous systems due to higher stability and the ease with which the catalyst can be separated from reactants and products.[3,24] This allows the use of continuous flow reactors, resulting in constant operation

increasing output and saving energy on restabilising reaction conditions; or the use of batch reactors facilitating rapid and selective removal of the catalyst so another batch can be quickly started with very little loss of catalyst.[3] Heterogeneous catalysts can be produced that are stable even under extreme conditions (high temperatures or pressures), which would decompose or deactivate most homogeneous and biocatalysts. The dry reforming of methane, the reaction of CH_4 and CO_2 to CO and H_2, is such a reaction requiring temperatures around 800°C due to its endothermic nature.[25]

Whilst the three areas of catalysis are generally considered as separate, attempts have been made to combine the advantages of heterogeneous and homogeneous/biocatalysts.[26,27] Heterogenising solution phase catalysts by attaching them to metal oxide or resin supports has been used to impart the desirable properties of the initial catalysts, such as high selectivity, with the benefits of a heterogeneous catalyst.[24,27] As a result, an interesting area of research combing the knowledge and advantages of the various parts of catalysis science has developed. Substantial advances are still required, as for example, tethering of homo/biocatalysts to a support often results in decreased performance of the initial catalyst and is often reversible.[27] Even with the ability to heterogenise soluble catalysts, heterogeneous catalysis still demonstrate a number of advantages, such as higher stability. As such, they are widely used in large scale industrial processes and often preferred for commercial applications.[3]

Another common factor to all areas of catalysis is the tailoring of the active sites in the catalyst to optimise the activity of a reaction or change the preference of different reactions.[23,28] In homogeneous and biocatalysis, modification of the electronic and steric properties of the active centre can alter activity and selectivity systematically; heterogeneous

catalysts may be tailored in a similar way.[29,30] Adjusting the properties (size, shape, metal, etc.) of heterogeneous catalysts has provided numerous routes for tuning their catalytic activities and selectivities, some of these methods will be discussed in the later sections.

1.2 Theory of catalysis

A catalyst works by providing an alternate route for a reaction; through interacting with reactants, intermediates, or products, they facilitate a reaction pathway with a lower activation energy than the un-catalysed reaction pathway.[4] From the definition of a catalyst it must not undergo any permanent change. To achieve a change in the reaction rate without a permanent change they must undergo a series of reaction steps which eventually result in the catalyst returning to its initial state, ready to perform the steps again.[3] In homogeneous catalysis this cycle is often drawn as a loop, with all the intermediate states depicted until the product is produced and the catalyst is regenerated.[31] This is not common with heterogeneous catalysis because the transition/intermediate states are less well defined, but the idea of a cycle still applies.[32] Advances in computational and surface science techniques are leading to much better understanding of the intermediate steps, so heterogeneous cycles depicting all intermediates are becoming more common.[33]

The first step in a heterogeneous catalytic cycle involves the adsorption of the reactant molecule(s) onto the surface.[4] When a molecule in solution or in the gas phase collides with a surface a number of events can occur, such as elastic/inelastic scattering or physisorption.[4] When the molecule is physisorbed it can move around on the surface or desorb back into the gas phase, once the molecule is physisorbed with the correct energy and geometry it can chemisorb, forming a chemical bond(s) to the surface.[4] Heterogeneous catalysis reactions

generally occur via an activated species, which is chemisorbed to the catalyst surface.[32] This can involve the breaking of bonds in the molecule, as seen in figure 1.1, termed dissociate adsorption.

A typical heterogeneous catalytic procedure is the synthesis of ammonia, the reaction path with and without a catalyst is shown in figure 1.1. The presence of a catalyst does not change the thermodynamic favourability of a reaction, which is determined by the relative energies of the reactants and products. Without a catalyst nitrogen and hydrogen must have a very high energy to react directly. In the presence of a catalyst, nitrogen and hydrogen undergo dissociative adsorption on the catalyst surface to form adsorbed nitrogen and hydrogen atoms, which are much more active than the molecular species. These species then react on the surface to produce ammonia which then desorbs, returning the catalyst to its original state.[34]

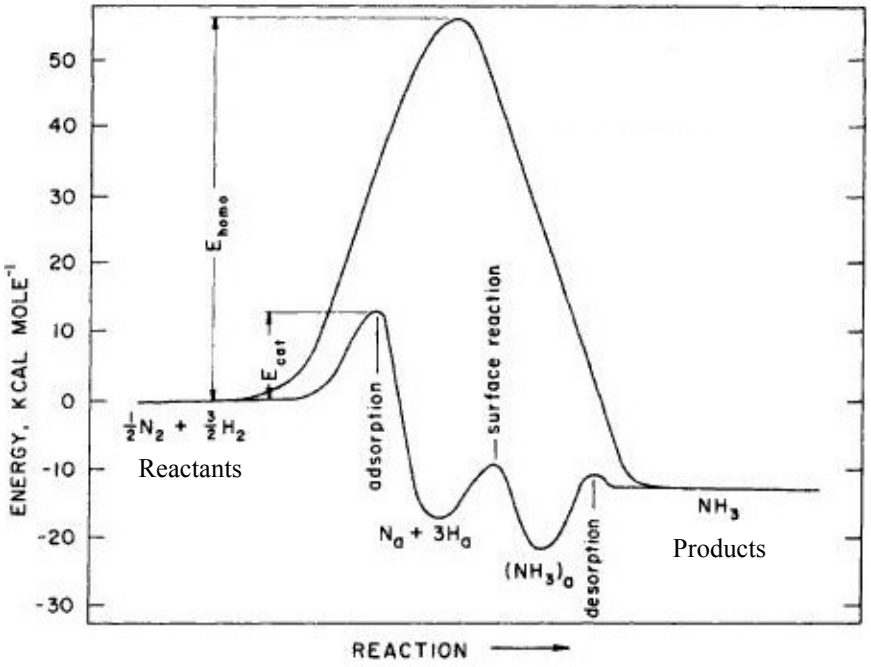


Figure 1.1– Reaction profile of the catalysed and un-catalysed synthesis of ammonia from the elements. Modified from reference[34]

From figure 1.1 it can be seen that the dissociative adsorption of nitrogen and hydrogen requires the most energy (E_{cat}) in the catalytic process, but is much less than required for the

direct reaction (E_{homo}), as the formation of surface nitrogen bonds assists the cleavage of the nitrogen triple bond. For the un-catalysed reaction, with a high activation energy (E_{homo}) only a small proportion of molecules will have sufficient energy to overcome this barrier and react, whereas the lower activation energy of the catalysed reaction (E_{cat}) allows more molecules to react. As such, the higher proportion of molecules with sufficient energy to react when a catalyst is present results in the reaction reaching equilibrium faster. As the energy of the gas molecules is dependent on temperature, a lower temperature can be used to achieve the same rate for the catalysed reaction compared to the un-catalysed reaction.[34]

Sabatier proposed the strength of a molecules' chemisorption to a catalyst surface is a key factor in determining the activity of a catalyst for a given reaction the adsorption of a molecule must be just the right strength.[32] If the molecule adsorbs too weakly, then it will desorb and not be present in high enough quantities to provide an activated surface intermediate for further reactions. If adsorbed too strongly the species will not be able to react or desorb from the catalyst surface resulting in blockage of the catalyst surface. The energy difference between the reactants and adsorbed species in figure 1.1 (N_a and H_a) is sufficient to cause the cleavage of the diatomic molecules and prevent desorption, but if it was much stronger the energy barrier for the surface reaction to occur would be very high and may slow or prevent the reaction from occurring.

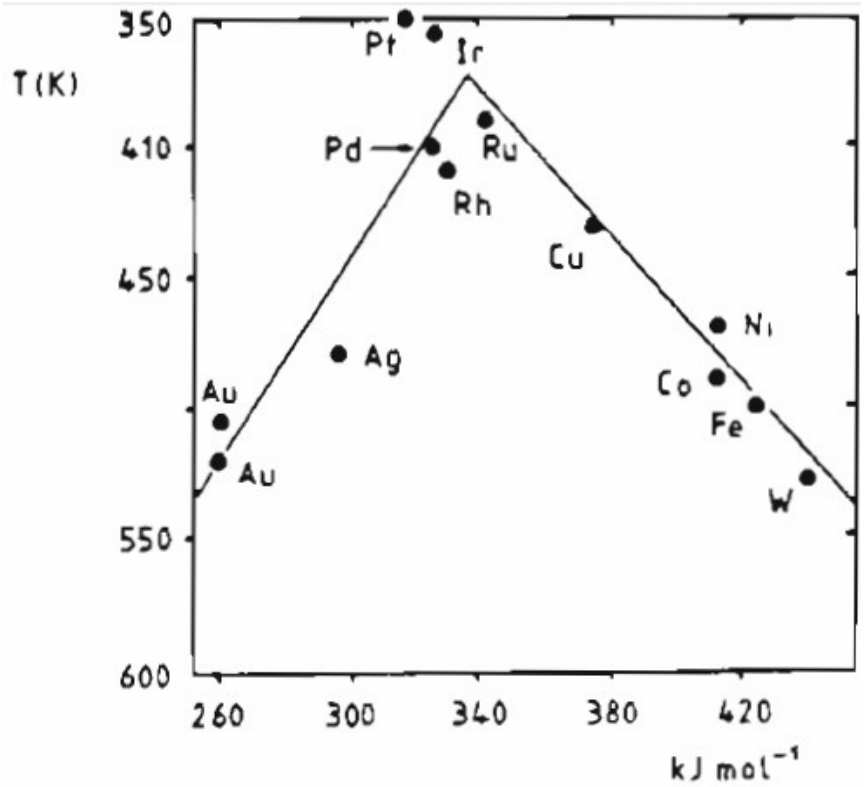


Figure 1.2– Volcano plot of formic acid conversion temperature against enthalpy of formation of the metal formate. Reproduced from reference[4]

The Sabatier principle was used to explain the volcano curves first reported by Balandin, in which a property related to the stability of the surface intermediate on a catalyst is plotted against a property related to the activity of the catalyst.[4] Figure 1.2 shows a typical volcano plot for the decomposition of formic acid; in the decomposition, a molecule is adsorbed dissociatively to adsorbed hydrogen and adsorbed formate which then undergoes further reactions to decompose to either carbon dioxide and hydrogen or carbon monoxide and water. Figure 1.2 displays the temperature required for a specified degree of conversion of formic acid against the heat of formation of the respective metal formate, and it can be seen that a maximum activity is found at an intermediate value of the heat of formation of the metal formate, indicating this is the point where adsorption strength is “just right”.

After adsorption of the reactant molecule, the surface bound species can then undergo further reactions, such as decomposition or reacting with another molecule that is either also bound to the surface or in close vicinity to it. Once formed the product molecule(s) desorbs from the surface, completing the catalytic cycle. The individual steps of a catalytic cycle are called elementary steps, if they are the most detailed sensible description of the processes occurring.[35]

Reaction kinetics is the study of the rates of processes or steps of a reaction cycle, depending on their time scale Ertl separated them into five categories ranging from a quantum level to a macroscopic level.[32] At the larger end of the scale, the pressure and temperature dependence of a reaction is fitted to empirical equations resulting in expressions for rate constants and activation energies of the overall reaction. At lower levels, studies of surface bound species on single crystals or the calculated stability of transition states allow detailed models of the specific reaction pathway to be produced. A number of assumptions and theories have been used to simplify the modelling of heterogeneously catalysed reactions, such as transition-state theory and the Bodenstein steady-state concept, that are widely found to be applicable.[32,35] Microkinetic studies use these theories and details of the reaction species and/or active sites on the catalyst surface to model rates and determine processes involved in the elementary reaction steps.[32] In most cases the rate of one elementary step in the reaction pathway is significantly slower than all of the other steps, this is defined as the "rate determining step" (RDS), and it controls the overall rate of the catalytic cycle.[35] The RDS can be described as an energy barrier the reactant(s) must cross for the reaction to proceed and identification of this step is an important factor in catalysis research, as increasing the rate of this step generally increases the activity of the catalyst.[32,35]

For the catalytic reaction in figure 1.1, the dissociative adsorption of nitrogen and hydrogen has a much higher energy barrier than any of the other steps and the fraction of molecules able to cross this barrier determines the rate of the reaction. The rate of a particular step in a reaction is given by its rate constant, k, this has a temperature dependence which is given by the Arrhenius' equation, shown in equation 1.1.[35]

$$k = Ae^{-\frac{E_a}{RT}} \qquad \text{Equation 1.1}$$

Where A is the pre-exponential factor, dependent on the frequency of molecular collisions that can be determined empirically and E_a is the activation energy. As the rate of the overall reaction is determined by the rate of the RDS, this relationship allows the activation energy of the entire reaction to be determined from the change in rate with different temperatures.

As the rate of the reaction is determined by a single elementary step in the catalytic cycle the rate can often be described in terms of the surface coverage of the reactant(s), θ_A is the fraction of surface covered with species A. There are a number of adsorption isotherms and limiting conditions used to model the surface coverage of reactants depending on: the relative strength of reactant, intermediate and product adsorption, what reaction is occurring, etc.[4] The Langmuir adsorption isotherm is one of the most commonly used isotherms.[4,32] For a unimolecular decomposition reaction, scheme 1.1, the rate of product formation can be expressed by equation 1.2, where k_2 is the rate determining step ($k_2 >> k_1$) and $K_A = k_1/k_{-1}$.

$$A_{(g)} \underset{k_{-1}}{\overset{k_1}{\rightleftharpoons}} A_{(ads)} \xrightarrow{k_2} Products \qquad \text{Scheme 1.1}$$

$$Rate = k_2\theta_A = \frac{k_2 K_A p_A}{(1+K_A p_A)} \qquad \text{Equation 1.2}$$

The Langmuir adsorption isotherm can be used to substitute θ_A in equation 1.2, this leads us to two extremes: (i) at low pressure the reaction rate is dependent on the pressure of A, or (ii) at high pressure the reaction rate is independent of A, the surface coverage is high so θ_A is approximately one. Similar models are used for bimolecular reactions, such as the Langmuir-Hinshelwood mechanism where the reaction occurs through two adsorbed species.[35] This mechanism applies for the synthesis of ammonia detailed in figure 1.1, with the reaction occurring between the adsorbed hydrogen and nitrogen atoms. An alternate bimolecular mechanism is the Eley-Rideal mechanism, where only one of the reactant species adsorbs and reacts with the other reactant that is not adsorbed.[35] It can be difficult to distinguish between the mechanisms; but by comparing the dependence of the reaction rate and species adsorbed on the catalyst surface with gas partial pressures, the mechanism can often be determined.[3]

A key assumption of Langmuir's adsorption isotherm, which is the basis for the Langmuir-Hinshelwood mechanism, is that the surface consists of identical non-interacting sites so adsorption can be treated with equal probability at each site and at all coverages.[36] For a real catalyst this assumption is not applicable, as Langmuir himself noted, but he proposed that it allowed a simplified model which would lead to more understanding of real surfaces.[32,36] Langmuir's model has been successfully used to accurately model a wide range of catalytic reactions over many different catalysts, but as new characterisation and computational techniques have shown, differences in catalyst surface structures are often very important in their activity.[4]

Taylor proposed the activity of the surface will vary from the case where only a few atoms are active to the case where they all are active, and thus the activity will depend on the reaction being catalysed.[37] It was later confirmed that the surface of catalysts consist of different sites

such as corners, edges, kinks, and terraces, and that these sites have different abilities to perform chemical reactions.[32,38] Some chemical reactions only occur on specific surface sites, so for different reactions the amount of catalytically active surface can vary greatly.[38] The sites that are catalytically active for a specified reaction are termed "active sites" and by normalising the rate of reaction by the number of active sites it is possible to calculate the relative activity of a site.[3,39] This "normalised activity" is called the Turnover Frequency (TOF) and is reported as moles of product per mole of active site per unit time. When the specific nature of active sites is not known or cannot be measured, the TOF is often reported with respect to the total surface area of the active phase of the catalyst, i.e. metal surface area.[3,39]

Whilst high activity is an important factor for a catalyst, ensuring production of the desired product is clearly another highly important factor. The ratio of a specified product to all other products gives the selectivity to the specified product.[3] Highly selective catalysts are desired to reduce the production of unwanted products that, even when produced at only a few percent can on industrial scale, result in large quantities of waste and have a significant economic impact. In some cases the production of undesired products or species present in the reactant stream block the active sites on the catalyst surface, these species are known as "poisons". These poisoning species bind very strongly to the catalyst and cause deactivation, which is a major cause of cost in industrial reactions.[3,4] As such, there has been much interest in the removal of feed gas impurities, preventing the formation of poisoning species and modifying reaction conditions to reduce the effects of catalyst deactivation through poisoning.[3,4,32]

The development of better catalysts, with increased activity, selectivity and poison resistance is a key area of catalysis research. Through knowledge of the rate determining step, adsorbed intermediates and active sites - obtained from fundamental studies of reactions and based on the theory presented above - the ability to engineer catalyst surfaces resulting in catalysts with desired catalytic properties has been demonstrated.[28,40] A wide range of methods have been utilised to provide more active and/or selective catalysts and catalysts with increased poison resistance, a number of these methods will be discussed in detail in section 1.4.[41–43]

1.3 Computational methods

In recent times the ability of computational methods to model catalysts and catalytic reactions has increased dramatically, due to the increasing speed and availability of powerful computers. Computational techniques have been widely used to model the adsorption strength of molecules on catalyst surfaces and the stability of the transition states/intermediates on catalyst surfaces.[44] The effects of modifying the electronic and geometric properties of catalyst surfaces through alloying, lattice expansion and other modifications, have been examined on the adsorbed species and reaction paths.[33,45–47] The results have both been used to explain experimental data and to independently predict new catalysts. Density functional theory (DFT) is commonly used for the description of adsorbate-surface interactions, as it allows for modelling of relatively large systems without being too computationally expensive, making it ideal for catalytic systems that may involve many atoms.[44]

DFT calculations describe the properties of a system using a set of one-electron Schrödinger equations.[44] These Kohn-Sham equations are solved to describe the electron density and total energy of the system. Catalysts are modelled as small sections of the surface, as performing

calculations on the huge number of atoms and sites present in real catalysts is often not practical. Two models are widely used to represent heterogeneous catalysts; they are the cluster model and the slab model (figure 1.3). In the cluster model a small group of atoms around the adsorption site is used to model the catalyst and it is assumed that atoms further away are not important. Whereas in the Slab model a repeating unit a few atomic layers deep with a surface area large enough to prevent interactions between adsorbates in adjacent units is used to model the catalyst surface, defined as a super cell.

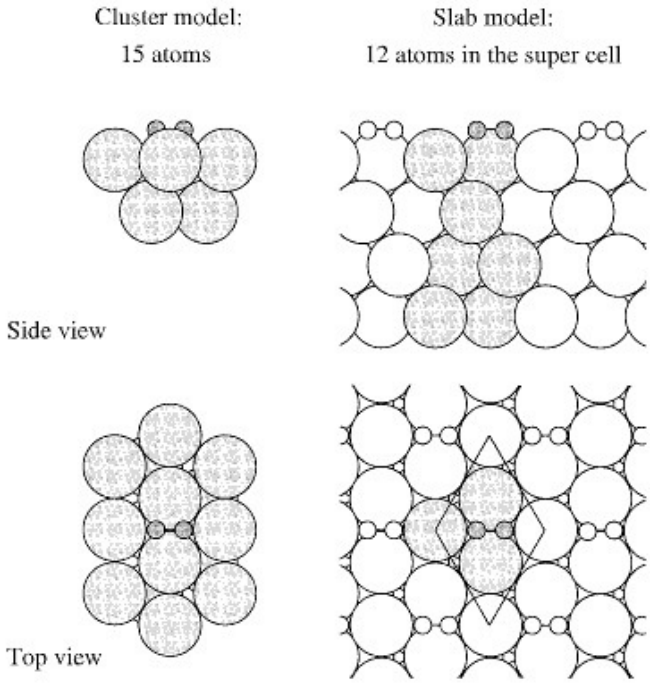


Figure 1.3– A schematic of slab and cluster representations of H_2 on a surface. Shaded and un-shaded circles show atoms in super cell and in repeating cells, respectively. Small circles are H_2. Reproduced from reference[44]

The other key parameters of DFT models are the basis set and the exchange-correlation function.[44] The basis set is an approximation used to simplify the Khon-Sham equations of the electronic orbitals of the system. Generally, for catalyst surfaces a pseudo-potential method is used to separate core and valence electrons. Valence electrons dominate bonding interactions and are modelled as a free electron gas in an infinite solid, mathematically

described as a plane wave. The main approximation in DFT is due to the exchange-correlation function, which is used to approximate the interactions between one-electron wavefunctions, and is used to reduce the impact of errors caused by the limitations of the slab/cluster size and basis set.

As the Sabatier principle explains, the strength of adsorption on the surface of heterogeneous catalysts is a key factor in determining their reactivity.[32] As DFT calculations give the electronic properties of the system the position of the d-band centre and the position of the Fermi level –the maximum energy of an electron at zero Kelvin– relative to an adsorbates bonding and anti-bonding orbitals can be used to determine the strength of an adsorbate-surface bond.[44] More details on this method are given in section 1.4.1. Nørskov and co-workers have successfully used this method to explain why Au is a noble metal and why other metals have varying degrees of reactivity.[48] Computational alterations to the electronic structure (through alloying, changing metal atom coordination number, changing the lattice parameter, etc.) can be elucidated in a highly controlled manner, which is often not possible experimentally, and the corresponding changes in adsorbate-surface interactions monitored.[45,46,49]

In a similar manner to calculating the adsorption strength of a single species, the mechanisms of reactions are computationally modelled from the relative stability of different adsorbed species on the catalyst surface and finding the lowest energy path from reactants to products.[33] The large number of variables determining the adsorption strength of each intermediate and transition state, such as surface site, adsorbate orientation, dissociation, etc., makes this a computationally heavy technique especially for reactions in solution where solvation or other solvent effects maybe important.[50] However, the increasing availability of

high power computer systems has recently led to a growth in mechanistic studies of more complex systems.[51]

1.4 Nanoparticle catalysis

Many heterogeneous catalysts consist of an active metal species on a support of carbon or a metal oxide.[12,41,52] The cost of the active metal is often very high, i.e. palladium with a cost of approximately £14 per gram is the active species in a large number of catalysts, therefore finely dispersing the metal to give a high surface area to volume ratio is highly desirable.[53,54] The drive for higher surface area to volume ratios meant that during early work on heterogeneous catalysis the nature the catalysts was unknown, as it was almost impossible to know what was occurring on the nano-scale.[55] This resulted in heterogeneous catalysis being named the "black art", however since development of the electron microscope and especially with recent developments in resolution and analytical techniques, such as energy-dispersive x-ray spectroscopy and high-angle annular dark-field imaging, the composition of catalysts has become much clearer.[55–57]

It is found that most heterogeneous catalysts containing precious metals, consist of particles on the nanoscale (1-100 nm) with most catalysts at the lower range of this scale.[58] The advancement of synthetic procedures and analytical techniques has resulted in the ability to create well defined and characterised nanoparticles.[43] Whilst developments in nanotechnology and nanoengineering have given access to a new level of control over properties of nanoparticles, such as size, shape, and composition; the application of these well-defined nanoparticles has resulted in new insights into catalysis.[55] Modifications can broadly be separated into electronic and geometric effects but it is often found that for a given

modification, such as particle size, both the electronic and geometric properties of the particles will be changed. Thus, it is often difficult to distinguish the role of the two effects but a number of results and analysis techniques have allowed the different influences on catalytic properties to be separated.[41,43,59] In sections 1.4.1-1.4.3, some commonly used methods of modifying nanoparticles will be discussed, highlighting the effects on catalytic activity and selectivity.

1.4.1 Electronic effects

Transition metal nanoparticles of 1-10 nm consist of less than 10^6 atoms, which results in them having properties between that of individual atoms and bulk metals.[39,60] In single atoms, i.e. in a complex, the electrons are isolated into atomic orbitals with discrete energy levels; the energies of the orbitals vary with the identity of the metal, oxidation state, type/number of ligands, amongst a range of other factors. For bulk metals, the orbitals of the individual metal centres overlap to form a continuum of possible electron energies known as a band structure. For transition metals, due to low coupling between d-states, the d-band is narrow relative to the s-band.[44]

Nørskov and Hammer proposed a theoretical model based on band theory for determining adsorption strength, which as we discussed previously is highly important in determining catalytic activity.[44,48] Their model involves two steps: the adsorbate first couples to the metals s-band, which due to the broad nature of the s-band only shifts the energy of the combined orbitals, this is the major factor in determining the overall adsorption energy. Secondly, bonding and anti-bonding states are formed by the coupling of the shifted adsorbate orbitals with the narrow metal d-band. As all transition metals have a half filled s-band (in the

metallic state), the coupling is the same for all transition metals. Thus coupling to the d-band differentiates the strength of binding between adsorbates and the transition metals. Therefore electronic modification of a metals d-band will modify the strength of adsorption and, as such, the catalytic properties.[46]

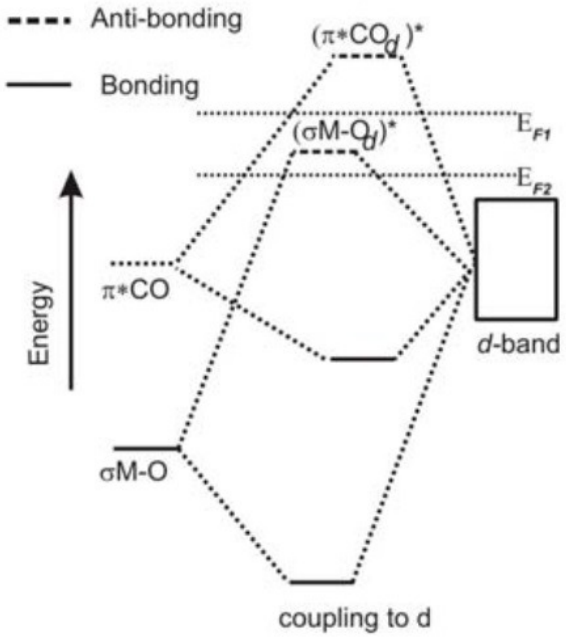


Figure 1.4– Effect of CO coupling to a transition metal d-band. Reproduced from reference[61]

As was mentioned in section 1.3 changing the position of the d-band centre and/or the Fermi level, alters the filling and position of the bonding and anti-bonding orbitals with the adsorbate, and thus modifies the adsorption energy. Figure 1.4 illustrates the coupling of CO with the d-band upon adsorption to a transition metal surface (with two different Fermi levels). If the Fermi level is high (E_{F1}) then the anti-bonding states are filled and adsorption is week, whereas if it is lower (E_{F2}) the anti-bonding orbitals are no longer filled resulting in strong adsorption.[44] For transition metal nanoparticles the low number of atoms and narrow d-band causes them to be highly susceptible to electronic modification.[46] In this section a range of methods used to modify the electronic structure will be discussed and some of the resulting effects on catalysis will be demonstrated.

One of the first observations of the effects of the size of metal particles on the electronic properties was the colour change of finely divided Au particles, noted by Faraday.[62] He observed that the colour change, from ruby to green, was due to the variation in size. It has since been found that for very small Au clusters, consisting of a few hundred to tens of atoms, there is also a transition from metallic to non-metallic properties.[63] A break-down in the band structure occurs, with discrete energy levels observed at the band edge as the clusters become more molecule-like. Due to its status as a noble metal, Au is not widely used as a catalyst but recently it has been found that in the form of small nanoparticles (<5 nm), where these modified electronic properties are observed in it can be highly active and selective for a range of reactions.[64]

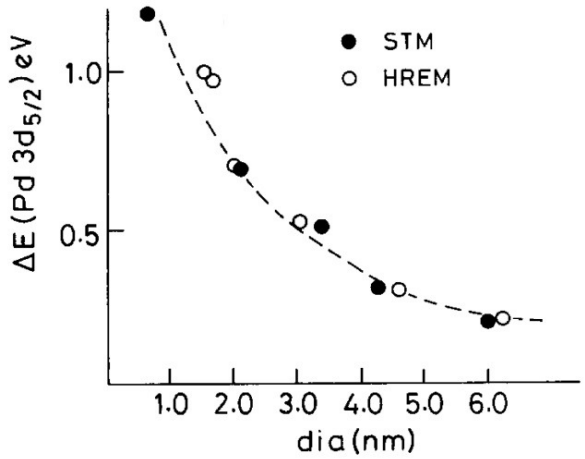


Figure 1.5– Variation of Pd $3d_{5/2}$ binding energy on changing particle size, with respect to bulk Pd. Reproduced from reference[65]

This modification of electronic properties with change in nanoparticle size has also been observed for a wide range of other metal nanoparticles.[63] Rao and co-workers deposited a range of different size Pd clusters (1-6 nm) on carbon supports, and using XPS observed a significant increase in the $Pd_{5/2}$ binding energy with decreasing particle size, shown in figure 1.5.[65] A change in conductance of these particles was also observed, again highlighting the

metal to non-metal transition at small sizes. Again the geometric and electronic properties are closely linked; the changes in electronic structure with particle size are reportedly due to an increase in low coordinate sites on the particle surface. These sites are electron deficient, as they are decoupled from the bulk atoms and have different d-hybridization.[66] Zhou *et al.* also reported an increase in $Pd_{5/2}$ binding energy of 0.2 eV from 40 nm to 9 nm particles, which correlated with an increased activity for formic acid electro-oxidation.[67] As these particles are relatively large, there is no significant change in the ratio of surface sites and as activity is normalised by surface area, it suggests the activity change is due to the electronic modification rather than geometric effects.

Whilst changing the size of nanoparticles has been shown to cause alterations to the electronic structure, limited particle stability under many reaction conditions and a constant desire for particles with a high metal surface area, make this an uncommon method to tune a metals electronic properties. A more common method of modifying the electronic structure of nanoparticle catalysts is the introduction of a second metal, to form bimetallic particles.[52] Geometric effects often have a significant impact on the catalytic activity of these particles, particularly in alloyed structures, but through the use of novel nanoparticle structures and computational methods the electronic and geometric effects can largely be separated. In alloyed bimetallic particles (figure 1.6c) the electronic modification caused by the addition of a second metal has clearly been observed by a number of analysis methods.[68] In alloy particles the breaking up of surface ensembles can also have a large effect on activity and selectivity; this will be discussed in section 1.4.2.

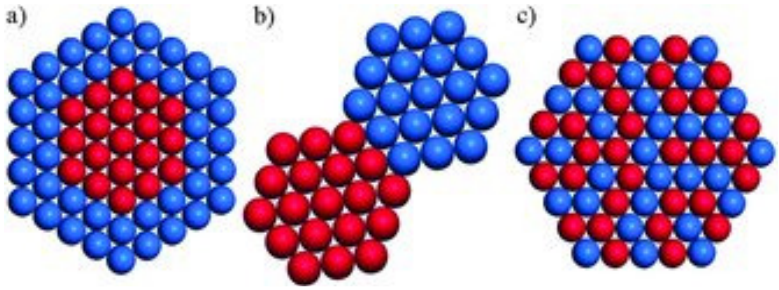


Figure 1.6– Illustration of some common bimetallic structures; (a) core-shell, (b) heterojunction, (c) alloy. Reproduced from reference[69]

Bimetallic particles with a core-shell composition (figure 1.6a) have been used to modify the electronic properties of metal surfaces, with minimal geometric modification to the surface. Tsang and co-workers reported a range of PVP stabilised nanoparticles consisting of a Pd shell with different transition metal cores (M@Pd), using ^{13}C NMR to monitor the electronic effects exhibited on a formic acid probe molecule by the surface a strong correlation between the work function of the core and the NMR shift was observed.[61] The difference in work function between the core and shell is shown to determine electron donation to or withdrawal from the surface, with associated modification of formic acid adsorption. This highlights the potential for the electronic properties of a surface to be tailored by a second metal.

This core-shell approach has also been used by Eichhorn *et al.* to produce a highly active catalyst for the selective oxidation of CO in hydrogen.[41] A 4.1 nm Ru core Pt shell particle (Ru@Pt) was found to have much higher activity, with CO oxidation completed below 20ºC, than either a RuPt alloy or physical mixture of monometallic particles, with complete oxidation occurring at 85ºC and 93ºC respectively. The selectivity of Ru@Pt particles for CO oxidation rather than H_2 is also higher than for either of the other catalysts. XPS analysis found the binding energies of the Pt $4f_{7/2}$ and Ru $3d_{5/2}$ were shifted to higher and lower energies, respectively, for the Ru@Pt particles compared to the monometallic particles. The presence of Ru causing a downshift in the Pt d-band and the effects on both Pt and Ru binding

energies, agrees with the reported NMR results of Tsang *et al*.[61] Effectively the metal with a higher work function becomes more electron rich and the other electron poor. DFT calculations performed using a Ru slab with a monolayer of Pt on the surface, coupled with a range of analysis techniques led them to propose that the Ru also modifies the Pt through lattice compression causing a downshift in the d-band centre. By downshifting the d-band centre of Pt, CO does not adsorb as strongly, resulting in available sites on the catalyst surface that can activate the other reactants giving a more active catalyst. Another advantage of core-shell particles is that the surface consists of only the active metal, so the high surface area of the small particles is all active for the reaction. Eichhorn *et al.* found that even though the Pt $4f_{7/2}$ was shifted to a higher binding energy in the RuPt alloy than with the Ru@Pt particles, the core-shell still had a much higher activity indicating the requirement of an uninterrupted Pt surface. This was highlighted by annealing the Ru@Pt catalyst at 500ºC, where the core-shell structure is lost becoming alloyed and the activity drops to that of synthesised alloy particles. This lack of stability is a significant problem with core-shell particles.

An alternate approach to electronic modification of bimetallic catalysts is to attach two different metal nanoparticles together (figure 1.6b), known as a heterojunction structure. In practice this can be difficult to control and the deposition or growth a second metal over part of the active surface of a particle, is often preferred. Using this method Yang *et al.* demonstrated Au nanorods partially encased in Ag gave a dramatic increase in activity for the reduction of *p*-nitrophenol by sodium borohydride.[70] A Au rod with ends encapsulated in Ag had a TOF over five times that of both a Au rod and a Au rod fully encapsulated in Ag. They propose that Au is the active surface and the presence of Ag increases electron density on Au increasing its activity.

As it was shown for Ru@Pt, DFT modelling is a very effective method to elucidate changes in a transition metals electronic structure. A huge advantage of computation methods is they allow a great deal of control over the structure of the bimetallic species being investigated, for example in the case of Ru@Pt the effect of the compression of the Pt lattice and the presence of the Ru underlayer can be examined separately which is very difficult if not impossible experimentally.[41] Nørskov and co-workers have produced a systematic study on the effect of mixing two transition metals on the position of the d-band centres for a range of catalytically important metals.[49] They considered both the addition of the second metal as an impurity (i.e. alloyed into the surface) or as an over-layer on the host metal (a core-shell structure), and calculated the d-band centre of the system. Whilst they do not suggest these structures are possible, they are presented to give ideas for modifying the electronic properties of a surface.

In a similar vain to the formation of a heterojunction between two metals, nanoparticles on a support have an interface between the metal and the support that can modify the electronic properties of nanoparticles, the interaction can be altered through changing the support material.[71] The influence of the support on metal nanoparticles is known as the "Metal-Support Interaction". The support can have a significant effect on both electronic and geometric properties of supported nanoparticles so will be discussed separately in section 1.4.3.

1.4.2 Geometric effects

Broadly, geometric effects are classed as any effect that doesn't directly affect the electronic structure of the nanoparticle.[44] As we have already noted, catalysts consisting of small particles are financially desirable due to a large surface to volume ratio and the reduction in

size can modify the electronic properties discussed in section 1.4.1. But changing the size also dramatically alters the ratio of corner, edge, and terrace sites on the metal surface, which were predicted by Taylor to have different activities.[37,60] The ratio of these sites is also highly dependent on the nanoparticle shape and to a more specific degree to the crystal planes present on the surface of the particle.[38] Thus, production of highly size/shape controlled particles is expected to allow their activity and selectivity to be tailored for desired reactions.[43] Some recent studies on the activity and selectivity changes of catalytic reactions as a result of modified geometric properties will be discussed in this section, including the influence of a secondary metal.

As it is relatively easy to control and measure the size of metal nanoparticles, the effect of particle size on catalysis has been widely studied and many reactions are found to be highly dependent on particle size.[43,59] Van Hardeveld and Hartog modelled different shape particles consisting of layered spheres with different crystal structures and different sizes, from this they produced mathematic models for the number of atoms with a given coordination number.[60] Figure 1.7a shows a typical cubo-octahedral particle with the different atom coordination numbers marked. It can clearly be seen that the different coordination numbers correlate with different sites on the catalyst surface, i.e. corner, edge, terrace. From the models, the ratio of atoms in each site can be calculated for a given metal at a specified size and from this figure 1.7b, displays the change in corner, edge, terrace, and total surface atoms as a percentage of total atoms of cubo-octahedral Pd particles of increasing size.

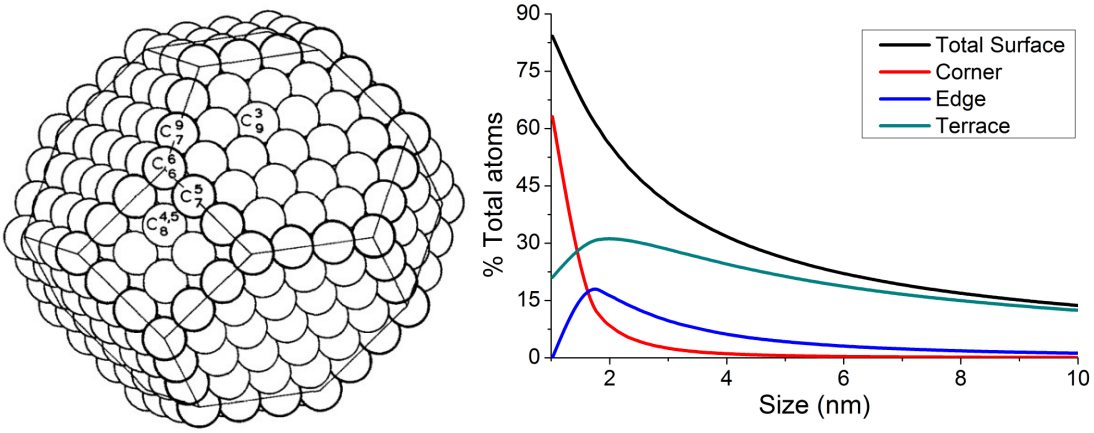


Figure 1.7– (a) Model cubo-octahedron reproduced from reference[60]; (b) calculated % of sites (corner, edge, terrace, and total surface sites) with respect to the total number of atoms for different size Pd cubo-octahedron

In agreement with Taylors' predictions, experimental results and DFT calculations have shown that sites with different coordination numbers have different properties (such as electron density and distance from its nearest neighbours), resulting in different activities for some reactions.[38,66] Boudart classified reactions in to two classes, structure sensitive or insensitive depending on how their activity increases with increasing metal surface area (decreasing particle size).[4] For structure insensitive reactions the activity increases linearly with increasing surface area; structure sensitive reactions do not have a linear relationship between activity and particle size. The difference in activities of specific surface sites is often the cause of a reaction being structure sensitive. On the other hand, structure insensitive reactions often occur through weakly bound species or, at high pressures, through the rapid formation of strongly bound species that block or mask any structure preference.

The effect of particle size on the hydrogenation of allyl alcohol (CH_2=$CHCH_2OH$) to propanol has been studied by Crooks and co-workers, over a range of dendrimer stabilised Pd particles with highly controlled sizes.[59] From figure 1.7b the most dramatic change in site ratio is found in the 1-3 nm range and as such this is the region investigated, with five samples

ranging from 1.3-1.9 nm. Interestingly, using a constant number of moles of Pd they find no change in activity - measured by hydrogen uptake per hour - for increasing particle size from 1.3-1.5 nm, but an increase in activity for 1.5-1.9 nm. This is unexpected, because with a constant number of moles of Pd the increasing particle size results in a decrease of total metal surface area. Using model cuboctahedral particles matching the size of their particles, with 55 to 250 atoms, they calculate the number of surface, defect, and face atoms for each size. The turnover frequency (moles H_2 uptake/moles active sites per hour) was calculated using each the number of surface, defect, face sites, and the total numbers of nanoparticles as the active site in turn (figure 1.8).

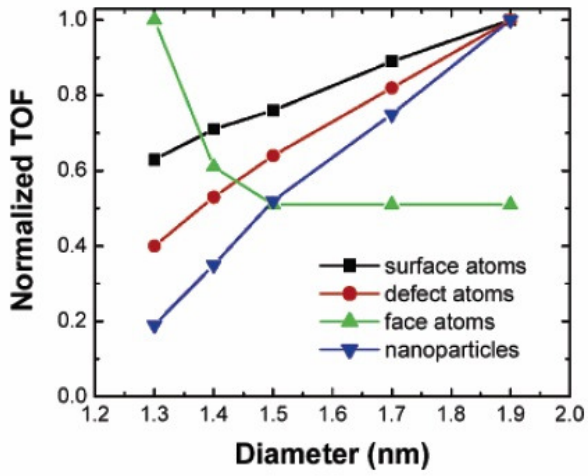


Figure 1.8– TOF of different size Pd particles for the activity of allyl alcohol hydrogenation, normalised by the fraction of different surface sites. Reproduced from reference[59]

The linear relationship between TOF (from surface, defect, and number of nanoparticles) and increasing size indicates that these sites are not the determining factor in the catalysts activity.[59] The fact there is no change in TOF (from face atoms), between 1.5-1.9 nm shows the TOF is dependent on the amount of face sites present in the catalyst. This implies that face sites are the preferred site for allyl alcohol hydrogenation, making the reaction structure sensitive. For the small particles (<1.5 nm), the rapid increase in TOF with decreasing size is

attributed to electronic effects being dominant rather than relative number of catalytic sites, which has been reported with particles of similar sizes and is observed by XPS (figure 1.5).

Thus far, we have mainly been concerned with the overall activity of a catalyst, but changes in selectivity are also of great importance to reduce waste and produce greener catalytic processes. For the hydrogenation of allyl alcohol, terrace sites were active whilst the other sites were not but for reactions with multiple products it is often found that the different sites on the metal surface (terrace/edge/corner) preferentially produce different products.[38,59] Thus, tailoring the sites on catalyst surfaces has been found to change the selectivity of a number of reactions. The synthesis of toluene from n-heptane is a clear example of this, it requires step sites to promote C-H cleavage and terrace sites to allow formation of the cyclic intermediate but kink or adatom sites promote unfavourable hydrogenolysis via C-C cleavage.[72,73] Through tailoring of the surface, optimum activity is achieved on single-crystals with five atom wide terraces separated by steps. For larger terraces the rate is found to slow as steps are too far away so C-H cleavage is limiting but on smaller terraces the cyclic intermediate cannot fit.

Further to the activities of different surface sites, studies of single-crystals terminated by different crystal planes have displayed that they can possess remarkably different activities for a number of reactions.[38] The synthesis of ammonia (figure 1.1) over iron is one of the most structure sensitive reactions and the activity is highly dependent on the packing of the surface.[73] The less tightly packed the Fe is on the surface the higher the activity, (111)>(100)>(110), with the (111) reported to be 400 times more active than (110). This is found to correlate with the ability of the surfaces to dissociatively chemisorb N_2, suggesting this is the rate determining step. From the studies of single crystals it is clear that not only are

the types of surface sites (corner, edge, terrace) in the catalyst important, but also the crystal planes present may have a significant effect on catalytic performance.

Whilst single-crystals have mainly been used for developing the understanding of reaction mechanisms or to model features of nanoparticle catalysts, the different activities of specific crystal planes clearly makes control of the surfaces in a catalyst desirable. Recent advances in the synthesis of nanoparticles with highly controlled shapes has allowed the production of particles totally encapsulated by particular crystal planes, mimicking single crystals.[74,75] As crystal planes have different surface energies, metal nanoparticles traditionally grow into a cuboctahedral shape, enclosed by (111) and (100) faces as this gives the lowest surface energy.[35] To promote the growth of different shape nanoparticles an additive is generally added to passivate a selected surface and promote growth on another surface, until the particle is encased with only the passivated surface.[76]

Somorjai has extensively studied the effects of different shaped nanoparticles on catalytic reactions and correlated them with single-crystal experiments, and has found strong agreement between systems terminated with the same faces.[73] He recently reported the hydrogenolysis of methylcyclopentane (MCP) over different shape Pt particles, with significant changes in selectivity.[43] The reactions of MCP are displayed in figure 1.9.

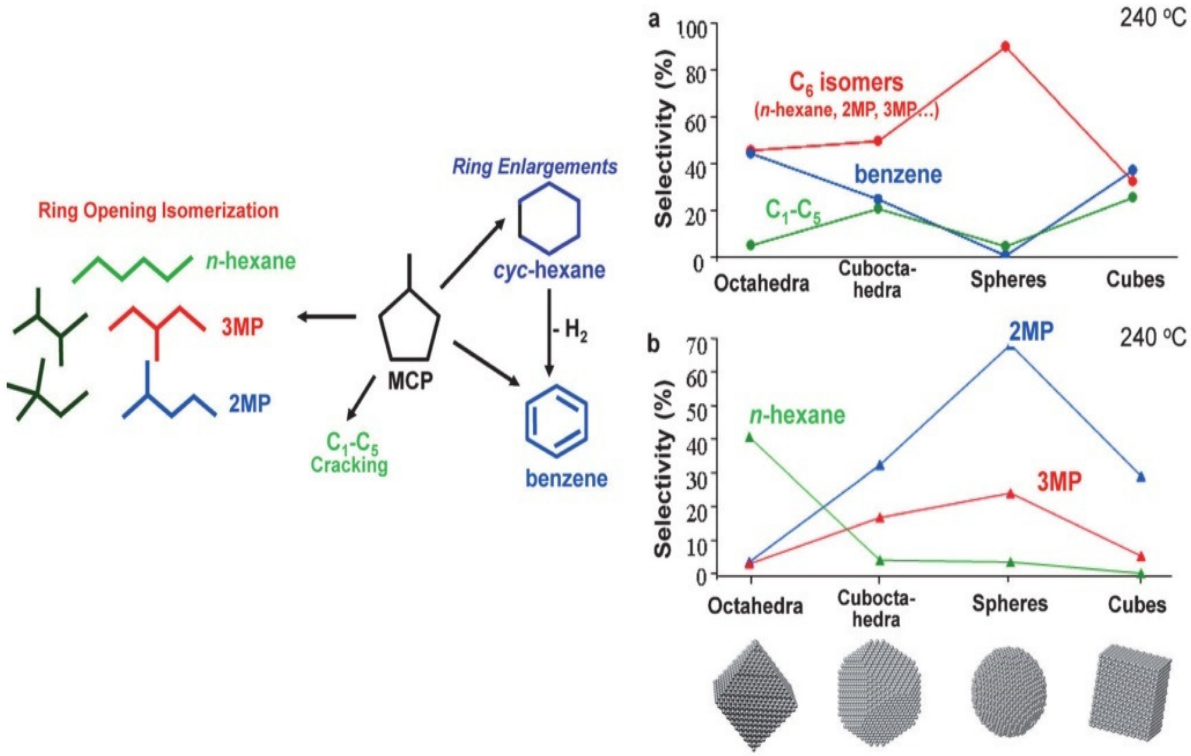


Figure 1.9– (Left) MCP reactions. (Right) dependence of the MCP reaction products on Pt particle shape. Modified from reference[74]

Somorjai *et al.* synthesised Pt octahedra with (110) surfaces, cuboctahedra with (111) and (100) surfaces, spheres with high index surfaces and cubes with (100) surfaces, all of ~6 nm.[43] Interestingly, they used a structure insensitive reaction (ethylene hydrogenation) to calculate the metal surface area because the activity should be independent of size and morphology. This allowed them to account for lost Pt surface area due to surface bound species remaining from the synthesis. For reactions with MCP the TOF varied greatly over the four catalysts; cuboctahedra and spheres had similar activities, with a TOF approximately three times that of octahedra and ten times that of cubes. The activation energies for the formation of the different products also varied greatly with particle shape, resulting in the distinct change in selectivity displayed in figure 1.9.

A detailed justification for the different reactivities and selectivities of the different shapes is not given, but some similarities can be drawn with the synthesis of toluene from n-heptane mentioned earlier. Firstly, the high index spheres result in a high proportion of ring opening products agreeing with the n-heptane reaction where kinks promoted C-C cleavage. The very low proportion of benzene produced by spheres also indicates the lack of sufficiently large terrace sites to produce the cyclic intermediate. The presence of the (100) surface also appears to be responsible for multiple C-C bond cleavage producing cracking products, as high levels are observed whenever it is present. Overall, this study highlights the dramatic influence the crystallographic plane, as well as the amount of edge/corner/terrace sites, can have on the selectivity of a reaction and why tailoring the surface features is such a key step in development of greener catalysts.

Although tailoring the sites on the catalyst surface, through changing size and/or shape has shown the significant influence the different sites and crystal planes can have on both activity and selectivity, these methods do have some serious limitations. Nanoparticles with controlled shape are often found to be unstable, requiring the use of low reaction temperatures.[77] Very small particles can also be unstable undergoing sintering or growth under reaction conditions, reducing the lifetime of the catalyst.[35]

An alternate method for modifying the geometric properties of nanoparticles is the introduction of a second metal. From a geometric point of view the role of a second metal in a bimetallic system can either be inert, simply blocking sites of the original metal, or be active, supplying another site on the surface with different properties.[78,79] Both of these roles of the second metal can be achieved through formation of an alloy or depositing the second metal on

the surface of the first.[40,78] Alloying is often the preferred method of geometric modification because it does not result in coverage of the, often very expensive, active material.[78]

For synthesis of alloyed systems, the two metals must have a similar surface energy otherwise one metal may segregate to or away from the catalyst surface. Nørskov and co-workers have used DFT to calculate the segregation energies for mixtures of transition metals, but the addition of adsorbates or different atmospheres can alter their preference to segregate to/from the surface.[47]

As we have previously seen for the synthesis of toluene from n-heptane, a specific arrangement of atoms is required for optimum activity.[72] The requirement for the correct arrangement of atoms required for a specific reaction is known as the ensemble effect, it is especially important in reactions with multiple paths.[3,4] Generally, a reaction will follow a path with the lowest energy for activation but if this route requires a large ensemble of active metal species, such as the cyclic intermediate in toluene formation, the favoured route of the reaction and therefore the selectivity can be changed by tuning ensemble size.[38]

Sachtler *et al.* investigated the effect of alloying Sn with Pt for the conversion of n-hexane in hydrogen; addition of Sn greatly reduced the formation of species that poisoned the catalyst.[79] Sn only altered the selectivity when present on the surface of the Pt catalyst, not when Pt was deposited onto pre-formed Sn particles indicating selectivity was modified by a geometric effect as any electronic effects would have remained in a core-shell structure. In PtSn alloys the different atoms where found to preferentially surround each other, creating isolated Pt atoms. The poisoning of the catalyst was due to formation of carbonaceous residues on the surface from extensively dehydrogenated species, which is reported to occur

on ensembles containing at least three Pt atoms. The reduction in poison formation and change in reaction selectivity, are thus explained by the reduction in the number of large Pt ensembles.

Whilst alloying is the major bimetallic method used for modifying nanoparticles, the blocking of specific sites and destruction of large ensembles can be achieved by the deposition of a second metal onto the surface of an existing nanoparticle.[40,73] After investigating the effect of Pt nanoparticle size on the selective reduction of cinnamaldehyde to cinnamyl alcohol, Tsang and co-workers found that large particles had higher selectivity due to the preferential adsorption of the carbonyl on flat surfaces.[28] Low coordination sites favoured interaction with the C=C π system resulting in unselective hydrogenation. The different properties of the catalyst surface sites was used to selectively poison the low coordinate sites by depositing cobalt on them, which resulted in the selectivity to cinnamyl alcohol increasing from 48% to 99% for 4.8 nm particles. This technique has also been widely used in electrochemistry, where deposition of the second metal onto the surface of a single-crystal or nanoparticle can be controlled.[80,81] Feliu and co-workers demonstrated this by depositing post transition metals onto the step sites of Pt single-crystal electrodes, which greatly reduced poisoning, indicating that it was the step site that produced the poison species.[82]

In the previous examples of bimetallic particles the second metal has been inactive for the reaction occurring, simply present to break-up ensembles of the active metal or to block sites that promote undesired reaction pathways.[79] For alloys containing an active second metal a "bi-functional" catalyst is formed, one metal performs one reaction and the other metal a different reaction.[3] A widely studied example of this is the addition of Ru to Pt for use as a direct methanol fuel cell catalysts.[40,78] In these catalysts, Pt is active for the cleavage of C-H

bonds but is readily poisoned by the resulting CO; Ru activates water much more easily than Pt forming an activated oxygen containing species in close proximity to Pt, which facilitates the oxidation of CO to CO_2. Ru has an electronic effect on Pt, as we saw from the Ru@Pt core-shell configuration in section 1.4.1, reducing the strength of CO binding however this is not the major cause of the reduced poisoning.[41] The optimal activity is not achieved with the maximum electronic effect, but found to occur with a ratio that results in an ensemble of three Pt atoms and one Ru atom on the surface, allowing stepwise dehydrogenation followed by oxidation of CO.[78]

1.4.3 Metal support interaction

All metal nanoparticles discussed so far are naturally unstable due to the high surface energy caused by the high surface area to volume ratio and on their own will agglomerate to form larger more stable particles.[4] This is often prevented by attaching ligands to the surface of the particles that keep them separated through steric or electrostatic repulsion.[61] The stability of these particles is limited especially at high temperatures, where the ligands decompose or come off and the activity of ligand stabilised particles is often greatly reduced because the ligands block surface sites.[83] Another method to keep the metal particles apart is to attach them to a support, which is the most common approach with numerous studies on a wide range of metals and support materials.[71] Metal nanoparticles can be added to the metal support by addition of pre-formed particles stabilised by ligands followed by removal of the ligands or more commonly, by addition of a metal precursor to the support followed by reduction to form metal particles.[71,83] The interaction between the particle and support reduces particle mobility, preventing agglomeration.

A wide range of materials are used as catalyst supports depending on the properties required of the catalyst and the conditions that it will operate under. Typically supports have high surface areas, 300-1000 m^2/gram, so the active metal species is highly dispersed.[4] However, for catalysts operating under very harsh conditions more stable, lower surface area supports are used (i.e. α-alumina). For industrial applications other factors are also important for the catalyst support (mechanical strength, etc.) to ensure a long lifetime with limited loss of the catalyst during use.[4]

The strength of the interaction between metal and support has a large effect on the size and stability of metal particles on its surface and is often a limiting factor in the size of catalyst used. For example, Zhao observed the agglomeration of Ag particles on a carbon film, over a year at 30°C and found a change from ~10 nm to above 100 nm, indicating the interaction between the particles and the support is not sufficient to overcome the high surface energy.[84] In stark contrast to Ag there are numerous reports of small Au clusters down to individual atoms on metal oxide surfaces, which are stable even at elevated temperatures.[56] The interaction between the support and metal nanoparticles can lead to significant effects on the particle structure, including changing the shape and distorting the metal lattice, both of which can greatly modify the catalytic properties.[45,85]

The interaction between the metal nanoparticles and the support can also modify the electronic properties through charge transfer, which has been important in explaining activity differences when changing supports.[71] A particularly dramatic electronic modification is seen with reducible metal oxides, such as TiO_2 and CeO_2, referred to as the Strong Metal-Support Interaction (SMSI).[32] It occurs after reduction at high temperatures, the metal ion of the support can be partially reduced (i.e. M^{4+} to M^{3+}) producing an electron rich metal oxide,

which results in an increased electron donation to the metal particles.[32] The SMSI effect may also result in geometric alterations to the metal surface, as the high temperature reduction has been reported to cause a thin coverage of the metal particle by the partially reduced support.[32] Interestingly, the SMSI is a reversible process, if the catalyst is oxidised (M^{3+} to M^{4+}) and re-reduced at a low temperature the electronic effect is not observed.

Novel methods have been developed to separate the electronic effects from any other, such as size, shape, surface blocking etc. One of these has been the synthesis of metal-metal oxide heterojunction structures similar to that depicted in figure 1.6b, but with one particle being a metal oxide. This has recently been reported by Sun and co-workers who synthesised a Pt particle with a single epitaxially linked Fe_3O_4 particle.[86] This technique allows them to tailor the size of both the Pt and Fe_3O_4 giving controlled coverage of the Pt surface and reducing effects of size and/or shape change upon attaching them. Comparing 5 nm Pt particles with and without Fe_3O_4, a 0.4 eV decrease in Pt 4f binding energy is observed, attributed to electron donation from Fe_3O_4 to Pt due to the higher work function of Pt. The corresponding electronic modification of Fe_3O_4 was also observed by a shift of the Fe(II)/Fe(III) redox potential, Fe_3O_4 in Pt-Fe_3O_4 is more easily reduced and difficult to oxidise. The electronic modification results in a significant improvement in activity for the oxygen reduction reaction, and the activity increases with Fe_3O_4 size, reaching a 20 fold increase in activity per gram of Pt for Pt(5 nm)-Fe_3O_4(17 nm). They have also produced an Au-Fe_3O_4 analogue, which through selective etching of either metal or metal-oxide, to reduce structural changes, is shown to be significantly more active than the sum of its parts.[87]

1.5 Formic acid

Formic acid has long been used as a probe for catalyst surfaces, as we saw in figure 1.2 it was one of the first adsorbates used to demonstrate Sabatiers' principle.[32] The simplicity of formic acid means that it is still used today as a model system for adsorption studies.[88] Another area of interest in formic acid has been as a hydrogen storage material.[89]

Due to the increasing world population and rapid development of many nations, the worldwide demand for energy has never been higher and is increasing.[17] The vast majority of energy is currently produced from fossil fuels, readily available supplies of which are limited and the waste products from their burning are linked with dramatic environmental damage.[30] Advancements in alternate sources of energy, such as wind and solar, indicate these may have an important role as replacements for fossil fuels, a problem with many of these current alternate fuels is storage of the often intermittent energy supplied and their applicability to transport or mobile devices.[90] Hydrogen is widely believed to play an important role in the future energy landscape, with the hydrogen economy proposed as a carbon independent system using hydrogen as the major carrier in the energy cycle.[17] The ability to store energy as hydrogen and release this energy through the use of hydrogen proton exchange membrane (PEM) fuel cells, displayed in figure 1.10, has driven interest in this area.[17]

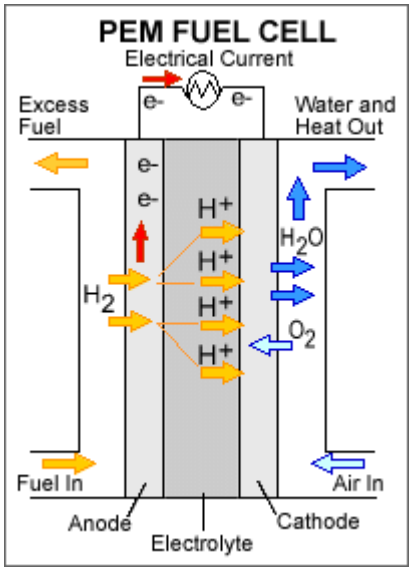


Figure 1.10– Schematic diagram of a hydrogen PEM fuel cell. Reproduced from reference[91]

Hydrogen PEM fuel cells consist of an anode and a cathode separated by a proton exchange membrane.[17,91] At the anode a catalyst splits molecular hydrogen into two protons, which pass through the membrane; and two electrons, which must travel around an external circuit to the cathode creating current. At the cathode the protons, electrons and molecular oxygen, from air, combine to form water. Currently the most active anode catalysts use platinum based nanoparticles, this means that the hydrogen supply should not contain CO or other species that bind strongly to Pt, otherwise the catalyst will be poisoned.[92,93] The most active anode catalysts can withstand up to 10 ppm CO with negligible side effects.[94] More complex catalysts can withstand higher CO concentrations (up to 500 ppm) without deactivation and filters can also be used to remove poisoning species but these methods result in more complex or less active fuel cells.[92,95]

Perhaps the most serious issue that is currently restricting the applicability of hydrogen as a fuel, particularly for mobile devices, is its transportation, storage and delivery.[90] A number of techniques are being used for hydrogen storage including high-pressure gas cylinders,

liquefied hydrogen, and a range of chemical methods such as alkali metal hydrides.[96,97] Recently, there has been increased interest in storing hydrogen as small molecules, which can be decomposed in situ to give hydrogen, such as hydrazine, borohydrides and formic acid.[90,97]

Formic acid has a hydrogen content of 4.4% weight, which is lower than the target set by the US Department of Energy (DoE) to be used in transportation fuels. The targets set by the DoE are by 2017 a 5.5% weight system –including tanks, pipes, cells, etc.– increasing to an ultimate goal of 7.5%. Thus, the current interest in the hydrogen storage properties of formic acid is due to its high hydrogen density, 53 g(H_2) L^{-1}, which is equivalent to hydrogen at 800 bar.[97] The relatively safe nature of formic acid compared to other liquid fuels, identified it as a particularly suitable hydrogen storage material suitable for small portable devices, such as mp3 players and laptop computers, with relatively low power requirements.[83] In these cases a high hydrogen percent weight is not a priority, and the high gravimetric hydrogen density of formic acid will allow the devices to maintain their small size.

1.5.1 Formic acid cycle

Another important feature which has driven interest in formic acid as a hydrogen storage material is the ease with which hydrogen can be stored and released.[90] The cycle displayed in figure 1.11 demonstrates the carbon neutral nature of the formic acid cycle (the net carbon output of the cycle is zero), as equal amounts of carbon dioxide will be released in situ during dehydrogenation as is captured in formic acid synthesis. The ability to release the bi-product of H_2 evolution (CO_2) to the atmosphere maintains the fuel at a constant 4.4% weight H_2, a significant advantage over some other small molecule hydrogen storage systems, such as

borohydride systems where the dehydrogenated products must be kept for subsequent re-hydrogenation.

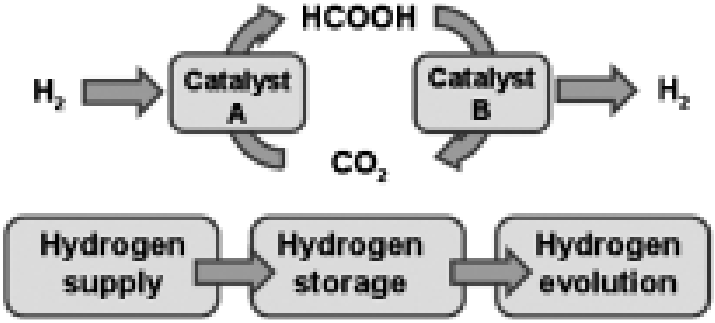


Figure 1.11– Hydrogen storage cycle based on formic acid/carbon dioxide[90]

An alternative system, in which formic acid is directly used as the fuel for a fuel cell has also been demonstrated.[61] The Direct Formic Acid Fuel Cell (DFAFC) has a number of problems, many of which are also associated with other non-hydrogen PEM fuel cell systems, including catalyst poisoning and membrane degradation. Some of these issues are also faced with the dehydrogenation of formic acid, such as poisoning, but by using a hydrogen PEM fuel cell many of the problems are avoided.

1.5.2 Formic acid synthesis

In figure 1.11, "catalyst A" hydrogenates CO_2 to formic acid, which is a reaction a vast number of catalysts have been shown to perform under a range of conditions.[30,90] Here a few will be summarised, along with some other methods of producing formic acid from CO_2 derived materials. Some of the first catalysts for hydrogenation of CO_2 were reported in 1976 by Inoue *et al.* using ruthenium complexes, but the activity was quite low.[98]

Since Inoue's reports the reaction has been shown to occur over a number of different transition metal catalysts in aqueous conditions, with the addition of amines.[90,99] It is found that very high activities can be achieved, for complex systems under optimal conditions; a

TOF of 95000 h^{-1} is observed for a $RuCl(OAc)(PMe_3)_4$ at 50°C under a high pressure of a CO_2/H_2 mixture.[30] Generally the activity is lower than this, most complexes reported have a TOF between 100-5000 h^{-1}.[30,90,99] Many of these complexes can also decompose formic acid back to hydrogen and CO_2, thus controlling the reaction conditions is a highly important factor in the production of formic acid. This feature has been used by Hull *et al.* who produced a system that will act as both "catalyst A" and "catalyst B" in figure 1.11.[100] Using an Ir complex with a ligand containing hydroxyl groups, they could change the favoured reaction of the catalyst depending on protonation of the hydroxyl groups. At low pH the protonated catalyst will decompose formic acid to CO_2 and H_2, whereas at higher pH the deprotonated catalyst performs the reverse reaction.

Whilst there has been much research on the hydrogenation of CO_2 using homogeneous catalysts there are fewer reports with heterogeneous catalysts. Feng *et al.* demonstrated that iron nanoparticles under mild hydrothermal conditions produced formic acid and acetic acid, with the ratio dependent on temperature and pressure.[101] Highly dispersed Au nanoparticles have also been found to hydrogenate CO_2 to formic acid.[102] At 180 bar and 40°C, Fachinetti *et al.* found that Au nanoparticles continuously produced formic acid from CO_2 and H_2 for 37 days.[102] It has also been reported that this Au based catalyst can produce formic acid from syngas, in a two-step process with CO_2 hydrogenation occurring after a water-gas-shift reaction to produce a 1:1 CO_2/H_2 mixture.[103]

Methods for the synthesis of formic acid without the need to directly hydrogenate CO_2 have been reported.[104] Generally, these methods involve the production of formic acid from biomass, in which case nature has converted CO_2 to sugars via photosynthesis. Enomoto *et al.* reported that under mild hydrothermal conditions biomass can be converted to formic acid,

they used glucose as a model carbohydrate and hydrogen peroxide as an oxygen source.[104] A high yield of high purity formic acid is produced, with the authors proposing it is feasible on an industrial scale.

1.5.3 Formic acid decomposition

In contrast to the widely studied hydrogenation of CO_2, the decomposition of formic acid was not studied substantially until recent times, but it was noted (as above) many of the homogeneous catalysts that hydrogenate CO_2 can also perform the reverse reaction under different reaction conditions.[100] When dehydrogenation is the desired process, it is found that a similarly wide range of transition metal complexes are highly active and selective. As the low hydrogen percent weight in formic acid has limited its potential hydrogen storage applications to small portable devices, a system based on a heterogeneous catalyst is highly desirable.[83] The advantages of using a heterogeneous catalyst are mainly due to the increased simplicity and stability of the reactor system, which are ideal due to the small size and portable nature of the intended devices.

This preference for a formic acid decomposition system based on a heterogeneous catalyst is highlighted by attempts to heterogenise a range of active homogeneous catalysts.[24,27] Laurenczy *et al.* have attempted to immobilise homogeneous catalysts using a number of methods: adsorption on zeolites, co-ordinating the catalyst with a functionalised polymer and ion exchange with a resin.[27] They found that immobilisation often resulted in a decreased activity of the catalyst, where the initial activity was maintained the catalyst was not as stable as the homogeneous species and significant deactivation occurred. This idea has been continued by Guo and co-workers, who recently coordinated complexes of Ru and Pd to the surface of silica through functionalised silanes, but their activity was much lower than many

reported homogeneous catalysts.[24] Their method of immobilising the metal complexes on the support involved refluxing in ethanol, which has been widely used to reduce metal particles, and limited reported characterisation means it is possible that this is in fact a heterogeneous catalyst.[105]

In the 1970's heterogeneous Pd catalysts were studied by Ruthven and Upadhye for the dehydrogenation of formic acid with a focus on the mechanism and the differences between the reaction in the aqueous and gas phase.[106] At that time the interest in hydrogen storage materials was limited and the development of heterogeneous catalysts for formic acid dehydrogenation was not widespread. Recently, interest in hydrogen storage materials has increased and as such interest in heterogeneous formic acid dehydrogenation catalysts has also rapidly increased.[52,53,90,99]

The dehydrogenation of gaseous formic acid either at temperatures above 100ºC or in the vapour phase, using an inert carrier, have been demonstrated using both metal oxides and metal nanoparticles supported on metal oxides, as catalysts.[107–109] Both of these methods greatly complicate the use of formic acid in portable devices as high control of gas flow, reaction heating and a supply of carrier gas would be required. For this reason most current research is concentrated on the solution phase decomposition, with the majority in aqueous conditions.[58,64]

In the solution phase a number of metal catalysts have been tested, both as colloidal and supported nanoparticles; Pd is generally reported to be the most active single metal under ambient conditions.[61] The development of heterogeneous catalysts through modification of

the electronic and geometric properties of the metal particles has been a recent area of high interest and the results will be discussed in detail in section 1.5.5.

Recently the concept of a formic acid based power generation system has been demonstrated.[99,110] Laurenczy's and co-workers developed a large scale system using a homogeneous catalyst with an output of 1 kW of electricity that has been used constantly for a year.[99] Even though significant engineering developments are still required to miniaturise and optimise this system it is an important proof of concept. Whilst continued research on increasing catalyst performance is required, the development of these systems highlights the potential of formic acid as a feasible hydrogen storage material.

1.5.4 Decomposition mechanism

Determining the mechanism of formic acid dehydrogenation is an important step in the development of nanoparticle catalysts tailored for high activity and selectivity. Formic acid can decompose by two mechanisms; it can be dehydrogenated producing H_2 and CO_2 (Eq. 1.3), which is clearly the desired reaction for supplying H_2 to a fuel cell, or it can be dehydrated producing H_2O and CO (Eq. 1.4).[83] The dehydration of formic acid is a highly undesirable reaction, not only does it waste fuel, but more significantly the CO produced is highly poisoning to both the fuel cell catalyst and the Pd-based catalysts generally used for formic acid decomposition.

$$HCOOH \longrightarrow H_2 + CO_2 \qquad \Delta G = -48.4 \text{ KJ mol}^{-1} \qquad \text{Equation (1.3)}$$

$$HCOOH \longrightarrow H_2O + CO \qquad \Delta G = -28.5 \text{ KJ mol}^{-1} \qquad \text{Equation (1.4)}$$

Using deuterated formic acid species, the rate determining step (RDS) has been identified as the cleavage of the C-H bond.[83,108] Exchange of the C-H proton for a deuterium atom forming DCOOH, results in a 1.5 times decrease in the reaction rate, a typical kinetic isotope effect. Exchange of the acidic proton to deuterium does not result in the iconic deactivation indicating that it is not involved in the RDS. Therefore, neither O-H cleavage nor the recombination of hydrogen adsorbed on the meal surface is rate limiting, identifying the C-H cleavage as the RDS. The transition state has also been probed using FTIR of formic acid adsorbed on metal surfaces, by in situ analysis of formic acid electro-oxidation catalysts and computationally, it is found that formic acid binds dissociatively to form a bound formate species and a hydrogen atom on the surface, the major binding modes of formic acid that have been widely identified are displayed in figure 1.12.[51,111,112]

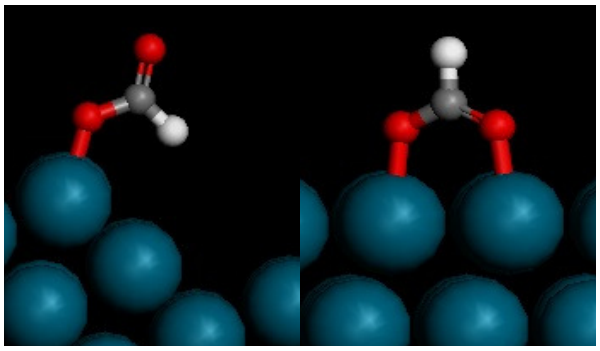


Figure 1.12– Bridging and monodentate binding modes of formate from dissociative adsorption of formic acid on a transition metal surface

The bridging formate mode has been identified as the intermediate of dehydrogenation, whereas formic acid binding through a single oxygen, to form monodentate formate, decomposes to CO and hydrogen.[83] In the case of electro-oxidation on Pt electrodes, these intermediates have been identified in situ along with generated CO poisoning species.[112,113] For electro-oxidation of formic acid two paths are widely reported: in the direct pathway formic acid is directly converted to CO_2 and $2H^+$; whereas for the indirect pathway formic acid is dehydrated to CO, followed by its oxidation.[112] The indirect pathway requires a

higher potential to oxidise CO, so comparing the activity of Pd single crystals with different numbers of low coordinate sites at a high and low voltage allowed the site of each path to be identified.[114] At lower potentials the flat surfaces gave the highest activity, with activity decreasing dramatically with the introduction of step sites; but at higher potentials stepped surfaces were found to have much higher activity.[114] Even though Hoshi *et al.* could not observe the bound species by IR it is apparent from the different activities of Pd crystals with different densities of steps, that the different reaction pathways are occurring on different sites. The indirect reaction, forming CO, is occurring on step sites resulting in the low activity of stepped surfaces at low potential, but at high potential with both pathways possible they are highly active. The site specific deposition of metals onto step sties of electrodes also shows a reduction in CO formation, again indicating the indirect pathway occurs on those sites.[82]

Following on from these electrochemical studies Tsang and co-workers proposed that at low coverages (expected in solution) the two binding modes are preferred on different sites, resulting in different pathways for formic acid decomposition.[61,83] As we saw in section 1.4.2, this site preference should make formic acid dehydrogenation a structure sensitive reaction with the activity not correlating with decrease in particle size. This was confirmed as an increase in activity was observed with increasing particle size, from 2.3 nm to 3.2 nm, even overcoming the associated loss in surface area.[83] From the higher activity of larger particles coupled with the changes in binding mode observed with increasing particle size and the results of electrochemical formic acid decomposition, it was determined that the bridging formate occurred on terrace sites and results in the dehydrogenation reaction (similar to the direct pathway in electro-oxidation).[111] Whereas the monodentate formate forms preferentially on low coordinate sites (corners or edges) and results in the dehydration

reaction, producing poisoning CO. Thus tailoring the geometric properties of the surface is highly important to achieve hydrogen production and prevent the formation of poisoning CO.

DFT calculations on the stability of adsorbed formic acid and its derivatives in various geometries have been performed on a range of metal surfaces, along with the prediction of reaction mechanisms resulting from lowest energy paths.[115] Many of these studies have been performed without the presence of water, simplifying the calculations, but it has been demonstrated by Akiya and Savage that addition of one or two molecules of water can significantly alter the structures of formic acid and as such the energies of its reactions.[50,115] Wang *et al.* also studied the influence of water on the adsorption and reaction mechanism of formic acid decomposition over Pd, and found that the presence of water can alter the rate determining step and even the total mechanism of decomposition.[51] This indicates the differences between experimental and calculated reaction mechanisms may be significant and could explain conflicting reported mechanisms. Huang and co-workers modelled the reaction pathway on a range of metals in the gas phase and in solution, they found an order of activities (Pd>Rh≈Pt>Au) similar to that observed experimentally.[33] But in the solution phase they propose a lowest energy reaction path through a solution phase formate ion, which conflicts with the experimental reports of Ruthven and Upadhye.[106] As we saw in section 1.2, the strength of adsorption is a key factor in determining the reactivity of a metal. Using DFT calculations GuiChang *et al.* studied the adsorption of formate on metal surfaces and found a linear correlation with d-band centre, which agrees with the linear relationship Tsang *et al.* found between the metal core work function and the activity of M@Pd core-shell particles, where M is a range of transition metals.[83,116] Even though the conditions used to model formic acid decomposition may vary, resulting in discrepancies between reports, it

appears comparison of calculated adsorption strength performed under the same conditions (water or not, etc.) results in trends with good correlation to experimental findings.[33,116]

As the rate determining step has been experimentally identified, any increase in rate is attributed to acceleration of this step. Tsang and co-workers found that as they increased electron density on the Pd surface, by changing the metal of the core, the rate of dehydrogenation increased, which was ascribed to higher electron donation into the C-H anti-bonding orbital weakening the C-H bond, promoting its cleavage.[83]

Many catalysts used for aqueous formic acid decomposition are found to suffer significant deactivation, which has been reported to be caused by adsorption of H_2 on active sites.[106] Zhou *et al.* did not find this to be the case and suggest that CO, produced from the dehydration of formic acid, is responsible for poisoning the catalyst.[52] They found that through alloying Pd with Au, the strength of CO adsorption could be weakened which results in reduced poisoning during formic acid decomposition. In most cases, it is believed that CO poisoning due to the dehydration reaction is the major factor in deactivating the catalysts.[52]

1.5.5 Developments in heterogeneous decomposition

A selection of reported formic acid decomposition catalysts will be discussed in this section, concentrating on the different methods that have been used to modify the catalytic activity rather than overall activity, due to differing reaction conditions throughout the literature. The modification of formic acid decomposition catalysts has two major objectives: firstly to increase the activity of the dehydrogenation reaction, and secondly prevent the formation of CO, which can poison both the gas stream and the decomposition catalyst.[52] A common

modification of the formic acid decomposition system is the addition of sodium formate, which can have a dramatic increase in the activity of catalysts for formic acid dehydrogenation.[52,117] The reason for this promotion is not clear, a number of reasons have been proposed but none are conclusive.[52] Further to this, it has been shown that sodium formate can be dehydrogenated over Pd based catalysts, producing H_2 and sodium bicarbonate, which in the presence of formic acid will react to produce CO_2 and sodium formate.[118,119] This presents an alternate reaction pathway when both formic acid and sodium formate are used, invalidating the direct comparison of the activity and selectivity of catalysts without the use of sodium formate.

One of the most widely used techniques is the formation of bimetallic nanoparticles, in section 1.4.1 and 1.4.2 it was demonstrated bimetallic catalysts can greatly modify both the electronic and geometric properties of a nanoparticle, depending on the structure. Increasing the d-band centre has been found to increase activity, so bimetallic particles containing Pd and group 11 elements have widely been examined.[52,53,58,83,120] Zhou and co-workers tested carbon supported alloys of Pd with a 3:1 ratio of Pd to Cu, Ag, or Au for formic acid decomposition at 90°C with the addition of sodium formate.[52] They found monometallic Pd was only active for a short time, but on alloying both Au and Ag greatly promoted the activity and stability of the catalysts, whereas Cu had minimal effect. This was attributed to Ag and Au preventing the stable binding of CO on the catalysts, thus preventing poisoning. On further investigation of the Pd-Ag/C alloy catalyst, after the first 10 minutes, they found constant gas generation for 240 hours with a CO concentration of approximately 100 ppm. The Pd-Au/C catalyst had the highest activity which is in contrast to the proposal of Tsang *et al.* that the activity is dependent on electron donation to Pd, but this could be due to the Pd-Au

particles being significantly smaller than the Pd-Ag catalyst (8 nm vs. 4 nm) or the dramatically different testing conditions between the two studies.[52,83]

On the other hand, Sun and co-workers have very recently (2013) reported highly active Pd-Ag and Pd-Au catalysts; with the Pd-Ag catalyst being more active than the Pd-Au as expected from electronic effects.[53,58] By reducing the size with respect to previous studies and optimising the Pd:Ag and Pd:Au ratios, similar activities to those reported by Zhou *et al.* have been achieved operating at a lower temperature (50°C) and without the addition of sodium formate.[52] The benefit of the alloyed surface has been examined using DFT calculations to model the electro-oxidation of formic acid over Au-Pd, the degree of alloying modifies the structure of the adsorbed formate and these ensemble effects strongly influence reaction selectivity.[121] Yuan and Liu proposed that without the presence of threefold Pd sites the energy barrier of CO formation is increased, which along with a lower CO binding strength, may be a contributing factor in the reduced poisoning and increased purity of the evolved gas.

Nanoparticles with more complex structures, such as a core-shell structure, have also been studied; the Tsang group found particles consisting of an Ag core with a Pd shell resulted in maximum activity, but only if the shell was sufficiently thin.[61,83] Using FTIR of adsorbed CO the electronic effects of the core could be monitored, with significant red-shift observed for a 1:1 ratio of Ag:Pd but no red-shift observed for the 1:3 sample. Atom probe tomography demonstrated the 1:1 sample contained 1-2 atomic layers of Pd on the Ag core whereas the 1:3 sample had 5-10 layers of Pd, indicating the range of electronic modification was limited.[83] Interestingly, they found that the increase in activity compared to monometallic Pd

was much more significant if the particles had a core-shell structure, than they had the more commonly used alloy structure.

Combining both the alloy and core-shell structure a PdAu@Au/C catalyst has been reported by Xing *et al.* with a Pd-Au alloy core with an Au shell, synthesised simply by co-reduction.[120] Interestingly this catalyst shows a high activity for a pure Au surface, in contrast with the vast majority of studies that have all been based on Pd or Pt as the active species. Additional studies have recently reported that small monometallic Au catalysts are active for formic acid decomposition.[64] As it was found with homogeneous catalysts, those that can hydrogenate CO_2 to formic acid will often decompose formic acid under different conditions. By altering the conditions, this has been found to be the case for Au. At elevated temperatures, in the presence of an amine, it is possible for Au nanoparticles to decompose formic acid with remarkably high TOF's.[64,122] Reducing the nanoparticles to the sub-nanometre range and using a support that demonstrates a strong metal support interaction, both of which have been shown to dramatically alter the electronic properties of Au, the reaction could proceed at 25°C producing <5 ppm CO, making the gas produced suitable for direct use in a hydrogen PEM fuel cell.

Taking a different approach to the majority of studies based on bimetallic modification, Zhou *et al.* reported that co-depositing their Pd-Au alloy catalyst on carbon with CeO_2 increases the activity by almost a factor of ten.[52] They suggest that the presence of ceria either results in the formation of cationic Pd that readily oxidises CO, or it changes the pathway of formic acid decomposition. The development of a catalyst containing a metal oxide has also been reported by Chan and co-workers, who produced a ternary $PtRuBiO_x$ structure.[123] They attribute the

high activity observed to a synergistic effect of the three components promoting C-H cleavage, preventing CO formation/adsorption and facilitating the generation/removal of CO_2.

The recent advances of Au based catalysts and highly active alloys highlight the fact that although a large number of studies have been performed on formic acid decomposition catalysts, there is still a significant scope for development. Whilst many of the approaches reported in sections 1.4.1-1.4.3, have been utilised for increasing the activity and selectivity of formic acid decomposition, a range have not. Thus, tailoring the active site on the catalyst surface using electronic or geometric modifications still has significant potential to provide dramatic increases in catalyst performance.

1.6 Aims and objectives

In this thesis some novel and less commonly utilised methods of modifying both the electronic and geometric properties of Pd nanoparticles will be investigated, and their effects on the room temperature decomposition of formic acid will be examined. The modification methods to be investigated are: the addition of a range of functional groups to the surface of Pd through the use of polymers, functionalisation of the catalyst support with promoting functional groups, and the deposition of a second metal on to the surface of Pd particles.

Whilst hydrogen production from formic acid is currently an area of great interest, the knowledge gained from understanding the mechanism of these modification methods has wider reaching consequences. Due to the extensive experimental and computational studies of formic acid decomposition over Pd catalysts a detailed description of the reaction mechanism exists, with both the surface sites required and intermediate species identified, making it an

ideal probe reaction. Thus, formic acid decomposition can be used to gain detailed knowledge about the mechanism by which these modification methods are altering the surface of the catalyst. This knowledge will not only be useful for the production of more active and selective formic acid dehydrogenation catalysts, but can also be applied to other reactions where the optimal nature of the active site is known.

The objectives of this thesis will be two-fold: firstly, the methods of modifying the catalyst will be studied to develop an understanding of the electronic and geometric modifications occurring on the catalyst surface. Secondly, these methods will be used to improve the activity and selectivity of Pd nanoparticles for formic acid dehydrogenation, with the aim to produce a highly active room temperature formic acid decomposition catalyst, which produces CO-free hydrogen that could be used directly in a PEM fuel cell, and suffers from very little or no deactivation.

1.7 Thesis overview

This thesis consists of seven chapters. Chapters four to six inclusive, detail the research performed during my study for this DPhil. degree.

Chapter One - Introduces catalysis, the basic theory and details of some methods used to modify nanoparticle catalysts. Also the role of formic acid as a hydrogen storage material and recent advances in its heterogeneous decomposition, are discussed.

Chapter Two – The background and theory of the analytical techniques used to characterise heterogeneous catalysts throughout this thesis are given.

Chapter Three – Gives a detailed description of the experimental methods used for synthesising, characterising and testing the catalysts discussed in this thesis.

Chapter Four – The effects of different polymer pendent groups on the surface of palladium nanoparticles is examined, using a range of analysis techniques and DFT calculations.

Chapter Five - The influence of attaching functional groups to the surface of catalyst supports is investigated for effects on the ability of palladium particles to decompose formic acid.

Chapter Six – Decoration of preformed palladium nanoparticle surfaces, through the deposition of a second metal, is studied for effects on the activity and selectivity of formic acid dehydrogenation.

Chapter Seven – Conclusions and the future outlook of the work is presented.

1.8 References

[1] M. Berzelius, *Edinburgh New Philosophical Journal* **1836**, *21*, 223–228.

[2] Oxford Dictionaries, "Oxford Dictionaries Catalyst definition," **2013**.

[3] J. Hagen, *Industrial Catalysis: A Practical Approach*, Wiley-VCH, **2006**.

[4] J. M. Thomas, W. J. Thomas, *Principles and Practice of Heterogeneous Catalysis*, Wiley-VCH, **1997**.

[5] V. Smil, *Nature* **1999**, *400*, 415–415.

[6] C. J. H. Jacobsen, *Chemical Communications* **2000**, 1057–1058.

[7] B. E. Smith, *Science (New York, N.Y.)* **2002**, *297*, 1654–1655.

[8] J. W. Erisman, M. A. Sutton, J. Galloway, Z. Klimont, W. Winiwarter, *Nature Geoscience* **2008**, *1*, 636–639.

[9] Forbes.com, "Global 2000 leading companies," can be found under http://www.forbes.com/global2000/, **2013**.

[10] A. Y. Khodakov, W. Chu, P. Fongarland, *Chemical Reviews* **2007**, *107*, 1692–1744.

[11] V. R. Calderone, N. R. Shiju, D. Curulla-Ferré, S. Chambrey, A. Khodakov, A. Rose, J. Thiessen, A. Jess, G. Rothenberg, *Angewandte Chemie International Edition* **2013**, *52*, 4397–4401.

[12] M. E. Dry, *Journal of Chemical Technology & Biotechnology* **2002**, *77*, 43–50.

[13] Research and Markets, "Global Catalysts Industry 2013-2018: Trend, Profit, and Forecast Analysis," can be found under http://www.researchandmarkets.com/research/nrcqzc/global_catalysts, **2013**.

[14] A. Schmid, J. S. Dordick, B. Hauer, A. Kiener, M. Wubbolts, B. Witholt, *Nature* **2001**, *409*, 258–268.

[15] R. A. Sheldon, I. W. C. E. Arends, U. Hanefeld, *Green Chemistry and Catalysis*, Wiley-VCH, **2007**.

[16] C. Song, *Catalysis Today* **2002**, *77*, 17–49.

[17] K. Bennaceur, B. Clark, F. M. Orr, T. S. Ramakrishnan, C. Roulet, E. Stout, *Oilfield Review* **2005**, 30–41.

[18] Hyundai Motor UK, "Hyundai ix35," can be found under http://www.hyundai.co.uk/about-us/environment/hydrogen-fuel-cell, **2013**.

[19] J. P. Rasor, E. Voss, *Applied Catalysis A: General* **2001**, *221*, 145–158.

[20] Z. Wei, F. Li, H. Xing, S. Deng, Q. Ren, *Korean Journal of Chemical Engineering* **2009**, *26*, 666–672.

[21] J. A. Osborn, F. H. Jardine, J. F. Young, G. Wilkinson, *Journal of the Chemical Society A: Inorganic, Physical, Theoretical* **1966**, *1*, 1711–1732.

[22] G. J. P. Britovsek, V. C. Gibson, D. F. Wass, *Angewandte Chemie International Edition* **1999**, *38*, 428–447.

[23] L. Resconi, L. Cavallo, A. Fait, F. Piemontesi, *Chemical Reviews* **2000**, *100*, 1253–1346.

[24] Y. Zhao, L. Deng, S. Tang, D.-M. Lai, B. Liao, Y. Fu, Q. Guo, *Energy & Fuels* **2011**, *25*, 3693–3697.

[25] J. A. Montoya, E. Romero-pascual, C. Gimon, P. Del Angel, A. Monzón, *Catalysis Today* **2000**, *63*, 71–85.

[26] J. A. Schwarz, C. Contescu, A. Contescu, *Chemical Reviews* **1995**, *95*, 477–510.

[27] W. Gan, P. J. Dyson, G. Laurenczy, *Reaction Kinetics and Catalysis Letters* **2009**, *98*, 205–213.

[28] S. C. Tsang, N. Cailuo, W. Oduro, A. T. S. Kong, L. Clifton, K. M. K. Yu, B. Thiebaut, J. Cookson, P. Bishop, *ACS Nano* **2008**, *2*, 2547–2553.

[29] B. Wu, H. Huang, J. Yang, N. Zheng, G. Fu, *Angewandte Chemie International Edition* **2012**, *51*, 3440–3443.

[30] S. Enthaler, *ChemSusChem* **2008**, *1*, 801–804.

[31] C. Fellay, N. Yan, P. J. Dyson, G. Laurenczy, *Chemistry - A European Journal* **2009**, *15*, 3752–3760.

[32] H. Knozinger, K. Kochloefl, *Heterogeneous Catalysis and Solid Catalysts*, Wiley-VCH, **2003**.

[33] C. Hu, S.-W. Ting, K.-Y. Chan, W. Huang, *International Journal of Hydrogen Energy* **2012**, *37*, 15956–15965.

[34] J. Richardson, *Principles of Catalyst Development*, Springer, **1989**.

[35] P. Stoltze, *Introduction to Heterogeneous Catalysis*, **1997**.

[36] I. Langmuir, *Transactions of the Faraday Society* **1922**, *17*, 607–620.

[37] H. S. Taylor, *Proceedings of the Royal Society A: Mathematical, Physical and Engineering Sciences* **1925**, *108*, 105–111.

[38] G. A. Somorjai, F. Zaera, *The Journal of Physical Chemistry* **1982**, *86*, 3070–3078.

[39] A. P. Umpierre, E. de Jesús, J. Dupont, *ChemCatChem* **2011**, *3*, 1413–1418.

[40] S. Jones, K. Tedsree, M. Sawangphruk, J. S. Foord, J. Fisher, D. Thompsett, S. C. E. Tsang, *ChemCatChem* **2010**, *2*, 1089–1095.

[41] S. Alayoglu, A. U. Nilekar, M. Mavrikakis, B. Eichhorn, *Nature Materials* **2008**, *7*, 333–338.

[42] M. A. Rigsby, W.-P. Zhou, A. Lewera, H. T. Duong, P. S. Bagus, W. Jaegermann, R. Hunger, A. Wieckowski, *The Journal of Physical Chemistry C* **2008**, *112*, 15595–15601.

[43] S. Alayoglu, C. Aliaga, C. Sprung, G. A. Somorjai, *Catalysis Letters* **2011**, *141*, 914–924.

[44] B. Hammer, J. Nørskov, *Advances in Catalysis* **2000**, *45*, 71–129.

[45] M. Mavrikakis, B. Hammer, J. Nørskov, *Physical Review Letters* **1998**, *81*, 2819–2822.

[46] J. Kitchin, J. Nørskov, M. Barteau, J. Chen, *Physical Review Letters* **2004**, *93*, 4–7.

[47] A. Ruban, H. Skriver, J. Nørskov, *Physical Review B* **1999**, *59*, 15990–16000.

[48] B. Hammer, J. K. Nørskov, *Nature* **1995**, *376*, 238–240.

[49] A. Ruban, B. Hammer, P. Stoltze, H. L. Skriver, J. K. Nørskov, *Journal of Molecular Catalysis A: Chemical* **1997**, *115*, 421–429.

[50] N. Akiya, P. E. Savage, *AIChE Journal* **1998**, *44*, 405–415.

[51] R. Zhang, H. Liu, B. Wang, L. Ling, *The Journal of Physical Chemistry C* **2012**, *116*, 22266–22280.

[52] X. Zhou, Y. Huang, W. Xing, C. Liu, J. Liao, T. Lu, *Chemical Communications* **2008**, 3540–3542.

[53] S. Zhang, Ö. Metin, D. Su, S. Sun, *Angewandte Chemie International Edition* **2013**, *52*, 3681–3684.

[54] Monex.com, "Palladium Price chart," can be found under http://www.monex.com/prods/palladium_chart.html, **2013**.

[55] R. Jin, *Nanotechnology Reviews* **2012**, *1*, 31–56.

[56] C.-T. Wu, K. M. K. Yu, F. Liao, N. Young, P. Nellist, A. Dent, A. Kroner, S. C. E. Tsang, *Nature Communications* **2012**, *3*, 1050–1058.

[57] H. Zhang, M. Jin, Y. Xia, *Chemical Society Reviews* **2012**, *41*, 8035–8049.

[58] Ö. Metin, X. Sun, S. Sun, *Nanoscale* **2013**, *5*, 910–912.

[59] O. M. Wilson, M. R. Knecht, J. C. Garcia-Martinez, R. M. Crooks, *Journal of the American Chemical Society* **2006**, *128*, 4510–4511.

[60] R. Van Hardeveld, F. Hartog, *Surface Science* **1969**, *15*, 189–230.

[61] K. Tedsree, C. W. A. Chan, S. Jones, Q. Cuan, W.-K. Li, X.-Q. Gong, S. C. E. Tsang, *Science (New York, N.Y.)* **2011**, *332*, 224–228.

[62] M. Faraday, *Philosophical Transactions of the Royal Society of London* **1857**, *147*, 145–181.

[63] C. N. R. Rao, G. U. Kulkarni, P. J. Thomas, P. P. Edwards, *Chemistry - A European Journal* **2002**, *8*, 28–35.

[64] Q.-Y. Bi, X.-L. Du, Y.-M. Liu, Y. Cao, H.-Y. He, K.-N. Fan, *Journal of the American Chemical Society* **2012**, *134*, 8926–8933.

[65] H. N. Aiyer, V. Vijayakrishnan, G. N. Subbanna, C. N. R. Rao, *Surface Science* **1994**, *313*, 392–398.

[66] K. W. Zilm, L. Bonneviot, G. L. Haller, O. H. Han, M. Kermarec, *The Journal of Physical Chemistry* **1990**, *94*, 8495–8498.

[67] W. P. Zhou, A. Lewera, R. Larsen, R. I. Masel, P. S. Bagus, A. Wieckowski, *The Journal of Physical Chemistry B* **2006**, *110*, 13393–13398.

[68] M. B. Boucher, B. Zugic, G. Cladaras, J. Kammert, M. D. Marcinkowski, T. J. Lawton, E. C. H. Sykes, M. Flytzani-Stephanopoulos, *Physical Chemistry Chemical Physics: PCCP* **2013**, *15*, 12187–12196.

[69] D. Wang, Y. Li, *Advanced Materials* **2011**, *23*, 1044–1060.

[70] X. Guo, Q. Zhang, Y. Sun, Q. Zhao, J. Yang, *ACS Nano* **2012**, *6*, 1165–1175.

[71] W.-J. Shen, M. Okumura, Y. Matsumura, M. Haruta, *Applied Catalysis A: General* **2001**, *213*, 225–232.

[72] W. Gillespie, R. Herz, E. Petersen, G. A. Somorjai, *Journal of Catalysis* **1981**, *70*, 147–159.

[73] G. A. Somorjai, J. Carrazza, *Industrial & Engineering Chemistry Fundermentals* **1986**, *25*, 63–69.

[74] K. An, G. A. Somorjai, *ChemCatChem* **2012**, *4*, 1512–1524.

[75] S. Cheong, J. D. Watt, R. D. Tilley, *Nanoscale* **2010**, *2*, 2045–2053.

[76] S. E. Habas, H. Lee, V. Radmilovic, G. A. Somorjai, P. Yang, *Nature Materials* **2007**, *6*, 692–697.

[77] M. Crespo-Quesada, J. M. Andanson, A. Yarulin, B. Lim, Y. Xia, L. Kiwi-Minsker, *Langmuir* **2011**, *27*, 7909–7916.

[78] Y. Liang, J. Li, Q. Xu, R. Hu, J. Lin, D. Liao, *Journal of Alloys and Compounds* **2008**, *465*, 296–304.

[79] F. Dautzenberg, J. Helle, P. Biloen, W. Sachtler, *Journal of Catalysis* **1980**, *63*, 119–128.

[80] J. L. Haan, K. M. Stafford, R. I. Masel, *The Journal of Physical Chemistry C* **2010**, *114*, 11665–11672.

[81] J. Clavilier, J. Feliu, A. Aldaz, *Journal of Electroanalytical Chemistry and Interfacial Electrochemistry* **1988**, *243*, 419–433.

[82] M. Maciá, E. Herrero, J. Feliu, *Electrochimica Acta* **2002**, *47*, 3653–3661.

[83] K. Tedsree, T. Li, S. Jones, C. W. A. Chan, K. M. K. Yu, P. A. J. Bagot, E. A. Marquis, G. D. W. Smith, S. C. E. Tsang, *Nature Nanotechnology* **2011**, *6*, 302–307.

[84] J. Li, Y. Lin, B. Zhao, *Journal of Nanoparticle Research* **2002**, *4*, 345–349.

[85] C. Henry, *Surface Science Reports* **1998**, *31*, 231–325.

[86] C. Wang, H. Daimon, S. Sun, *Nano Letters* **2009**, *9*, 1493–1496.

[87] Y. Lee, M. A. Garcia, N. A. Frey Huls, S. Sun, *Angewandte Chemie International Edition* **2010**, *49*, 1271–1274.

[88] M. Bowker, P. Stone, R. Bennett, N. Perkins, *Surface Science* **2002**, *511*, 435–448.

[89] A. Boddien, H. Junge, *Nature Nanotechnology* **2011**, *6*, 265–266.

[90] S. Enthaler, J. von Langermann, T. Schmidt, *Energy & Environmental Science* **2010**, *3*, 1207–1217.

[91] U.S. Department of Energy, "Types of Fuel Cell," can be found under http://www1.eere.energy.gov/hydrogenandfuelcells/fuelcells/fc_types.html#pem, **2011**.

[92] X. Cheng, Z. Shi, N. Glass, L. Zhang, J. Zhang, D. Song, Z.-S. Liu, H. Wang, J. Shen, *Journal of Power Sources* **2007**, *165*, 739–756.

[93] V. A. Sethuraman, J. W. Weidner, *Electrochimica Acta* **2010**, *55*, 5683–5694.

[94] T. E. Springer, T. Rockward, T. A. Zawodzinski, S. Gottesfeld, *Journal of The Electrochemical Society* **2001**, *148*, A11–A23.

[95] T. Yamanaka, T. Takeguchi, G. Wang, E. N. Muhamad, W. Ueda, *Journal of Power Sources* **2010**, *195*, 6398–6404.

[96] B. Sakintuna, F. Lamaridarkrim, M. Hirscher, *International Journal of Hydrogen Energy* **2007**, *32*, 1121–1140.

[97] A. Züttel, *Materials Today* **2003**, *6*, 24–33.

[98] Y. Inoue, H. Izumida, Y. Sasaki, H. Hashimoto, *Chemistry Letters* **1976**, *5*, 863–864.

[99] M. Grasemann, G. Laurenczy, *Energy & Environmental Science* **2012**, *5*, 8171–8181.

[100] J. F. Hull, Y. Himeda, W.-H. Wang, B. Hashiguchi, R. Periana, D. J. Szalda, J. T. Muckerman, E. Fujita, *Nature Chemistry* **2012**, *4*, 383–388.

[101] C. He, G. Tian, Z. Liu, S. Feng, *Organic Letters* **2010**, *12*, 649–651.

[102] D. Preti, C. Resta, S. Squarcialupi, G. Fachinetti, *Angewandte Chemie International Edition* **2011**, *50*, 12551–12554.

[103] D. Preti, S. Squarcialupi, G. Fachinetti, *ChemCatChem* **2012**, *4*, 469–471.

[104] F. Jin, J. Yun, G. Li, A. Kishita, K. Tohji, H. Enomoto, *AIP Conference Proceedings* **2008**, *987*, 139–142.

[105] Y. Zhang, J. Yu, H. Niu, H. Liu, *Journal of Colloid and Interface Science* **2007**, *313*, 503–510.

[106] D. Ruthven, R. Upadhye, *Journal of Catalysis* **1971**, *21*, 39–47.

[107] S. A. Halawy, S. S. Al-shihry, M. A. Mohamed, **1997**, *48*, 247–251.

[108] M. Ojeda, E. Iglesia, *Angewandte Chemie International Edition* **2009**, *48*, 4800–4803.

[109] D. A. Bulushev, L. Jia, S. Beloshapkin, J. R. H. Ross, *Chemical Communications* **2012**, *48*, 4184–4186.

[110] A. Majewski, D. J. Morris, K. Kendall, M. Wills, *ChemSusChem* **2010**, *3*, 431–434.

[111] K. Tedsree, A. T. S. Kong, S. C. Tsang, *Angewandte Chemie International Edition* **2009**, *48*, 1443–1446.

[112] G. Samjeské, A. Miki, S. Ye, M. Osawa, *The Journal of Physical Chemistry B* **2006**, *110*, 16559–16566.

[113] A. Miki, S. Ye, M. Osawa, *Chemical Communications* **2002**, 1500–1501.

[114] N. Hoshi, M. Nakamura, K. Kida, *Electrochemistry Communications* **2007**, *9*, 279–282.

[115] D. J. Morris, G. J. Clarkson, M. Wills, *Organometallics* **2009**, *28*, 4133–4140.

[116] H. Ma, G. Wang, Y. Morikawa, J. Nakamura, *Science in China Series B: Chemistry* **2009**, *52*, 1427–1433.

[117] X. Gu, Z.-H. Lu, H.-L. Jiang, T. Akita, Q. Xu, *Journal of the American Chemical Society* **2011**, *133*, 11822–11825.

[118] H. Wiener, Y. Sasson, J. Blum, *Journal of Molecular Catalysis* **1986**, *35*, 277–284.

[119] B. Zaidman, H. Wiener, Y. Sasson, *International Journal of Hydrogen Energy* **1986**, *11*, 341–347.

[120] Y. Huang, X. Zhou, M. Yin, C. Liu, W. Xing, *Chemistry of Materials* **2010**, *22*, 5122–5128.

[121] D. W. Yuan, Z. R. Liu, *Journal of Power Sources* **2013**, *224*, 241–249.

[122] M. Yadav, T. Akita, N. Tsumori, Q. Xu, *Journal of Materials Chemistry* **2012**, *22*, 12582–12586.

[123] S.-W. Ting, S. Cheng, K.-Y. Tsang, N. van der Laak, K.-Y. Chan, *Chemical Communications* **2009**, 7333–7335.

Chapter 2

Analytical Techniques

Chapter 2 Analytical Techniques 63

2.1 Introduction 64

2.2 X-ray powder diffraction 65

2.3 X-ray photoelectron spectroscopy 68

2.4 Thermogravimetric analysis 70

2.5 Transmission electron microscopy 71

2.6 Energy-dispersive x-ray spectroscopy 73

2.7 Pulse chemisorption 74

2.8 Fourier transform infrared spectroscopy 76

2.9 References 79

2.1 Introduction

Information on the nature of a catalysts surface can provide important insights into the mechanism of a catalytic reaction, leading to extensive understanding of specific catalysts for specific reactions.[1,2] As such, characterisation of catalysts has become a key part in their development cycle and the knowledge gained about the effects of altering their properties has greatly advanced the ability to intelligently design catalytic materials.[3] In chapter one, the different activities of different metal surface sites, such as corners, edges and terraces, in some reactions were demonstrated. Additionally, changing the electronic properties of metal nanoparticles resulted in significant changes in catalytic reactivity. Thus to understand the catalytic activity and selectivity of a material, it is vital to have information on its electronic and geometric properties. Furthermore, the influence of modification methods (alloying, core-shell, support effects, etc.) used to tailor nanoparticle catalysts must be understood, so that their effects on catalytic performance can be predicted and the most suitable techniques for modifying catalysts can be intelligently identified for a given situation.[4–6]

A vast number of analytical techniques have been developed that probe different aspects of the bulk and/or surface properties of catalyst materials.[7–9] However, the aspects probed by a single analysis technique are sometimes limited and a range of complimentary methods are commonly required for understanding a catalyst's properties, especially how they are altered under different conditions. In this chapter details of the analysis techniques used throughout the course of this thesis are presented, with examples of the information provided by these techniques and their theoretical principles.

2.2 X-ray powder diffraction

X-ray diffraction (XRD) is one of the most widely used techniques to characterise nanoparticle catalysts.[10] It provides information on the composition, crystal structure, and size of crystallite materials, which form the basis of many heterogeneous catalysts.[1] XRD relies on the scattering of incident x-rays by the structure of an ordered material and as the wavelength (λ) of the x-rays is similar to the atomic spacing in crystalline materials, a high degree of scattering is observed.

Typically, x-rays are generated by electronic bombardment of a Cu anode resulting in the production of high energy x-rays. These x-rays are monochromated before interaction with the sample and the resulting scattered x-rays are detected over a wide range of angles by altering the relative positions of the x-ray source, sample and detector. The scattering of x-rays occurs predominantly from the electrons of an ordered material, and results in constructive and destructive interference of the x-rays producing a diffraction pattern. Through modelling the crystal as a series of parallel crystal planes (figure 2.1), the angles at which constructive interference will be observed is predicted by Bragg's law (equation 2.1).

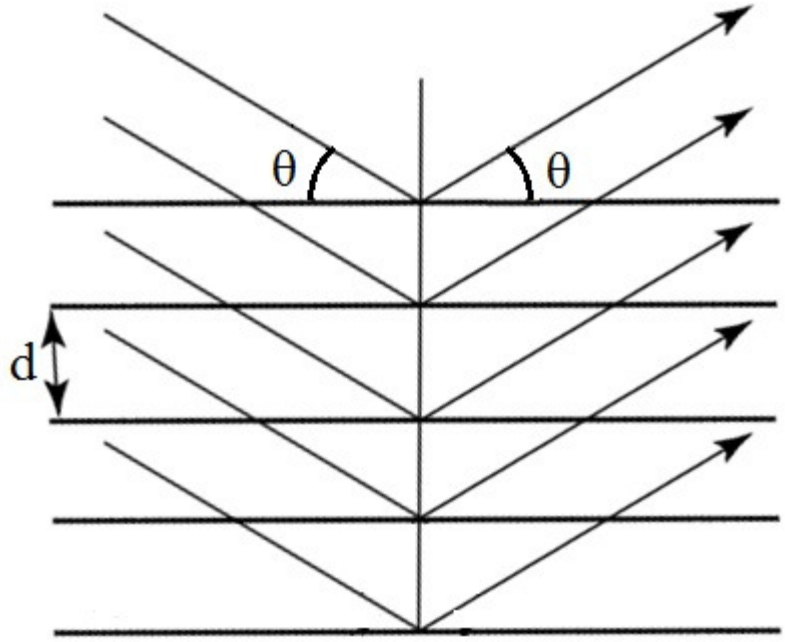


Figure 2.1– Schematic diagram of constructive interference from a crystalline structure. Modified from reference[10]

$$n\lambda = 2\mathrm{d}\sin\theta \qquad \text{Equation 2.1}$$

Where λ is the wavelength of the x-rays, d is the spacing between scattering layers, θ is the angle of incident x-rays to the crystal planes and n is an integer value depending on the layer of scattering. Thus, a change in the lattice parameter of the crystalline material alters the spacing between the diffracting layers of the sample, which shifts the angles at which constructive interference is observed. The d spacing can be related to the lattice parameter for a cubic crystal structure by equation 2.2, which when combined with Braggs law results in equation 2.3.

$$d^2 = \frac{a}{h^2 + k^2 + l^2} \qquad \text{Equation 2.2}$$

$$\left(\frac{\lambda}{2a}\right)^2 = \frac{\sin^2\theta}{h^2 + k^2 + l^2}$$ Equation 2.3

Where *h*, *k*, *l* are the miller indices of the Bragg plane and *a* is the lattice parameter. The change in lattice parameter can be used to describe the degree of alloying in bimetallic systems, which has led to an empirical relationship called Vegards law that relates the amount of metal doped into another metal to the shift in lattice parameter (equation 2.4). From the lattice parameter of the individual metals and assuming the doping of one metal into the other, a linear relationship is obtained.

$$a_{1,2} = xa_1 + (1 - x)a_2$$ Equation 2.4

Where $a_{1/2}$ is the lattice parameter of metal one or two, $a_{1,2}$ is the lattice parameter of the alloy of the two metals and x is the fraction of metal one alloyed into metal two. Whilst XRD gives important information on the composition and structure of materials, it is also possible to derive the average size of the nanoparticles of the catalyst. From the limited long range order of the crystal planes in nanometre size particles, broadening of the diffraction peaks is observed. Using the Scherrer equation (equation 2.5), this broadening of the diffraction peaks can be related to the average size of the crystalline regions in the sample.

$$L = \frac{K\lambda}{\beta \cos\theta}$$ Equation 2.5

Where L is the average crystallite size, K is the shape factor, β is the peak broadening at full-width half maximum and θ is the angle of x-rays to the crystal planes. Thus, from XRD a vast amount of information about the structure and composition of metal nanoparticle catalysts can be gained. The information on structure, such as alloy formation and particle size, can provide information on the electronic and geometric properties of the catalyst.

2.3 X-ray photoelectron spectroscopy

X-ray photoelectron spectroscopy (XPS) is another x-ray based analysis technique, which is widely used in the analysis of both surface composition and oxidation state of catalysts, with a high sensitivity.[7] A monochromatic beam of soft x-rays of a known energy, typically Al K_α with an energy of 1486 eV, is used to irradiate a sample under ultra-high vacuum conditions. These x-rays induce photoelectron emission from the core-levels of an atom, by a process illustrated in figure 2.2.

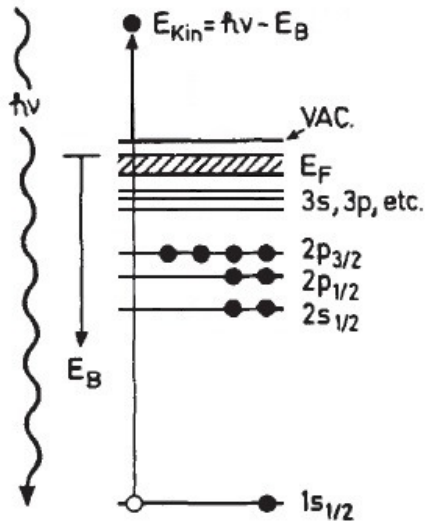


Figure 2.2– Schematic diagram of the photoelectric emission of a core 1s electron. Reproduced from reference[7]

As the energy of the incoming photons is fixed (hν), the kinetic energy of the emitted electrons varies depending on the energy required to remove the electron from the sample. The observed kinetic energies of the emitted electrons can be converted to the binding energy of the electrons (equation 2.6), which correspond to specific orbitals of a particular element.

$$E_B = h\nu - E_K \qquad \text{Equation 2.6}$$

Where E_B is the binding energy of the electron in the solid, E_K is the kinetic energy of the emitted photoelectrons and $h\nu$ is the energy of the incoming photon. The binding energy of a specific orbital of an element is characteristic of that element and can be used to identify the substituent elements in a catalyst. Additionally, variations in these characteristic binding energies can be used to identify the oxidation state or any modification of the electronic structure of an element caused by chemical environment that is termed chemical shift. Typically an increase in binding energy represents a higher oxidation state, with a decreased binding energy signifying a negative oxidation state.[9]

Further to the information on the electronic properties and identification of elements in a sample, the quantitative composition of a material can also be determined. If instrumental factors are constant, the relative areas of the peaks in XPS spectra depend on the number of electrons emitted by each element. The number of electrons emitted by each element depends on its photoelectron cross-section, the inelastic mean free path of the emitted electrons in the material and the concentration of that element in the material. Relative sensitivity factors can be used to relate the peak areas to the relative concentration of elements in the sample, using equation 2.6. The relative sensitivity factors account for the elements photoelectron cross-section, electron mean free path and common instrument factors.[8] The relative sensitivity

factors have been calculated and tabulated for a wide range of elements for given incident x-ray energies.

$$C_x = \frac{\left(\frac{I_x}{S_x}\right)}{\sum_i \frac{I_i}{S_i}} \quad \text{Equation 2.7}$$

Where C_x is the concentration of element x, I_x is the area of the peak from element x, S_x is the sensitivity factor of element x, I_i is the area of the peak from element i and S_i is the sensitivity factor of element i. XPS is commonly referred to as a surface sensitive technique, due to the sampling depth being limited to 3-10 nm, depending on the composition of the material and the mean free path of electrons in the material.[9] However, the small size of most nanoparticle catalysts means that this sampling depth results in analysis of the whole particle rather than just the surface, thus XPS analysis of nanoparticles generally gives information on the overall composition.

2.4 Thermogravimetric analysis

Thermogravimetric analysis (TGA) monitors the weight of the sample as a function of temperature. During a programmed heating or cooling process, under a controlled atmosphere, the change of sample weight is recorded. The weight change is typically reported as percentage weight loss/gain and rate of weight change, which can be used to identify weight change from the oxidation, reduction or any decomposition of the sample depending on the atmosphere under which the analysis is performed. A schematic representation of the TGA Q50 used throughout this thesis is displayed in figure 2.3.

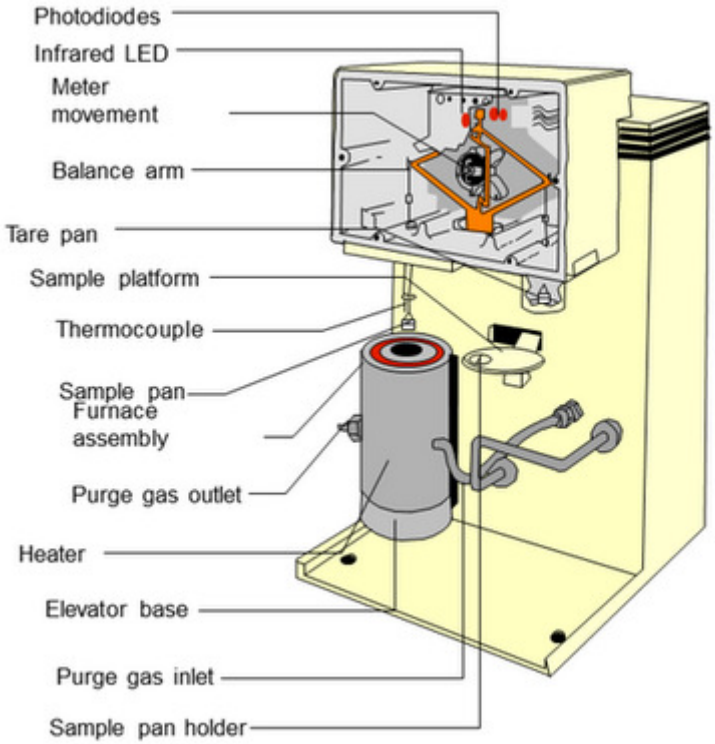


Figure 2.3– Schematic of TGA Q50[11]

A TGA consists of a highly accurate balance, a well-controlled furnace with a thermocouple in close proximity to the sample and a purge gas setup to control the atmosphere over the sample. The balance uses photodiode detectors to determine the offset between the sample pan and an empty pan contained in the balance housing (tare pan), which provides a high degree of accuracy in measuring mass changes.

2.5 Transmission electron microscopy

Transmission electron microscopy (TEM) uses a beam of high energy electrons to produce high resolution images through a sample; as the wavelength of electrons is much smaller than that of visible light they allow a much higher resolution than for optical microscopy with modern instruments providing atomic resolution. TEM is a valuable technique for examining

nanoparticle catalysts as it is one of the most direct methods for imaging the catalyst, resulting in information on the size, shape and dispersion of nanoparticles in a catalyst.[7,9,12] Additionally, high resolution TEM can give composition and structural information from observation of the lattice parameter and atomic arrangement of the nanoparticles. Electrons are generated from a filament and accelerated to high energy (typically 100-200 kV) to produce electrons with a de Broglie wavelength (0.025 Å at 200 kV) much smaller than typical interatomic spacing's.[8] Using a series of electromagnetic lenses and apertures these electrons are focused to a small coherent beam, which is shone through the sample before a number of further electromagnetic lenses re-focus the image onto a phosphor coated screen. Then, in modern systems, a CCD camera is used to capture the final image directly into a digital format.

Bright-field TEM utilises the electrons than are transmitted through the sample or slightly scattered, which are then refocused using the lenses after the sample, however a number of electrons are scattered (elastically or inelastically) to a larger degree and reduce the brightness of the image. Therefore thin samples must be used in TEM, to limit scattering allowing sufficient electrons to penetrate through the sample to give a clear image. The higher the energy of the electron beam the thicker the sample that can be examined, but the thickness is generally limited to ~200 μm. Scattering of electrons by the sample depends on the atomic number of the atom, heavy atoms with large nuclei scatter electrons more than lighter atoms which, in bright-field TEM, provides a degree of elemental identification from the intensity of the electron beam and is referred to as Z-contrast. A number of other TEM methods exist that utilise combinations of electrons that have undergone different degrees of scattering, which can provide different information from the specimen.

2.6 Energy-dispersive x-ray spectroscopy

Energy-dispersive x-ray spectroscopy (EDX) is commonly used in conjunction with electron microscopy and provides elemental analysis with a high degree of spatial resolution.[8] This technique is widely used in analysis of catalysts because it not only provides information on the elemental composition of the catalyst, but also an understanding of how the elements are distributed throughout the catalyst.

When a sample is exposed to the incident high-energy electron beam used in TEM it can result in ionisation of the atoms through the loss of a core electron. An outer electron can then move down to fill the lower energy hole. The energy lost by the electron from moving to a lower orbital, results in a release of energy in the form of x-rays. The energy of these emitted x-rays depends on the relative energies of the orbitals and is characteristic of an element. Alternatively the high-energy electron beam can transfer energy to the atom without ionising it, this energy is also emitted as x-rays of various energies depending on the amount of energy transferred from the electron beam. The direction of these two types of emitted x-rays is different, with the first being emitted isotropically and the second being emitted predominately in a forward direction. Thus by placing the EDX detector on the same side of the sample as the incident electron beam, the characteristic x-rays can be preferentially detected. The emitted x-rays are detected by photoelectric absorption, commonly in a Si single crystal, that allows the number of x-rays of a specific energy to be counted. Therefore from the amount of x-rays detected at each characteristic energy, the ratio of each element present in the sample can be determined and by combining this with the high degree of spatial resolution provided by TEM a detailed compositional map of the sample can be formed.

2.7 Pulse chemisorption

Pulse chemisorption can be used to measure the surface area of different parts of the catalyst system. Depending on the adsorbant gas used, it can identify the active surface area (i.e. metal surface area) or total surface area of the catalyst. This technique provides a powerful method for the quick determination of the catalytically active surface area, which is a crucial factor for calculating turnover frequencies and understanding the absolute activity the sites on a catalyst surface.[13] Using a gas that adsorbs to a specific surface in the catalyst system, a loop of known volume, a thermal conductivity detector, and an inert carrier gas, the amount of gas that adsorbs to a known mass of sample can be accurately measured. Multiple pulses of an adsorbate gas are flowed over the sample, using an inert carrier gas, and the peak area of each pulse is monitored. In figure 2.4 a representative pulse chemisorption profile is displayed, the low area of the initial peaks is due to adsorption of the pulse gas on the surface of the sample. Once the surface is saturated, the peak area becomes constant representing the signal from the total volume of the loop. Comparing the difference in the area of the initial peaks with that of the full loop, the total volume of gas adsorbed by the sample can be calculated.

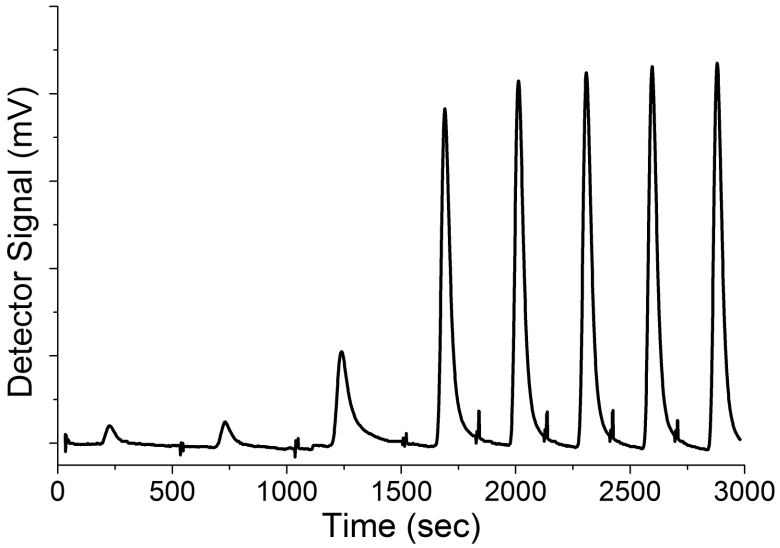


Figure 2.4– Typical pulse chemisorption profile

For metal catalysts, CO and H_2 are commonly used to selectively bind to the metal surface whilst not binding to the catalyst supports allowing metal surface area to be calculated.[14] Whereas, an adsorbate gas such as nitrogen can bind to both metal and support surface, giving total surface area. The number of moles of adsorbate gas per pulse can be calculated from the pulse volume and the ambient temperature, which allows the moles of gas adsorbed to be calculated. Thus, the metal surface area can be calculated using equation 2.8.

$$A_m = \frac{n_{ads} N_A S}{C_m m_m} \qquad \text{Equation 2.8}$$

Where A_m is surface area per gram of metal, n_{ads} is the moles of gas adsorbed, N_A is Avogadro's number, S is the stoichiometry of the adsorbate binding on the metal surface, C_m is the surface packing density of the metal and m_m is the mass of metal in the sample. This surface area can be used to give a measure of the dispersion of the catalyst using equation 2.9, which is a ratio of the moles of metal on the catalyst surface to the total moles of metal in the sample. The surface area can also be used to calculate an average size of metal nanoparticles, equation 2.10.

$$D = \frac{N_S}{N_T} \qquad \text{Equation 2.9}$$

$$d = \frac{S_f \times 10^3}{A_m \rho_m} \qquad \text{Equation 2.10}$$

Where D is the dispersion of the metal, N_S is the moles of surface metal, N_T is the total moles of metal, d is the average diameter of metal nanoparticles and S_f is the shape factor, which depends on the shape of the metal nanoparticles and the amount of metal surface in contact with the support.

2.8 Fourier transform infrared spectroscopy

Fourier transform infrared spectroscopy (FTIR) is a technique that can be used to analyse IR active species on the surface of catalysts, often this involves determination of reaction intermediates or organic functional groups on the catalyst surface through detection of the characteristic stretching and bending frequencies of specific functional groups.[9] Additionally, changes in these characteristic adsorption bands for chemical probe molecules (such as CO) indicate electronic and geometric interactions between the molecule and the catalyst surface. This is a widely used technique to investigate both the electronic and geometric properties of nanoparticle surfaces.[15]

The stretching frequency of a bond can be approximated using Hooke's law, by modelling the bond as a simple harmonic oscillator with two masses connected by a spring. The energy required to stretch or compress the bond is thus related to the masses on the ends and the strength of the bond/spring, this results in characteristic stretching frequencies for different molecules with shifts in these frequencies dependent on electronic modification of the bonds. For the case of a diatomic molecule, equation 2.11 relates the energy of the vibration to the atoms of the molecule and the bond strength.

$$\tilde{\nu} = \frac{1}{2\pi c}\sqrt{\frac{f(m_1 + m_2)}{m_1 m_2}}$$ Equation 2.11

Where $\tilde{\nu}$ is the vibrational frequency (cm^{-1}), $m_{1/2}$ is the mass of atoms 1 or 2 (g), c is the speed of light (cm s^{-1}) and f is the force constant of the bond (g s^{-2}). CO is a common probe molecule for metal nanoparticles, through changes in the strength of the C=O bond information on both the electronic and geometric properties of the metal surface can be identified.[12] Metal surfaces typically donate electrons into the π* antibonding orbital of CO, which alters the stretching frequency of the bond observed by IR. The degree of back donation depends on the binding geometry of CO, which is commonly a bi-dentate bridging or a mono-dentate linear configuration with CO bound to two or one metal atoms respectively, and on the electron density and work function of the metal surface. Thus through examining changes in the position and ratio of peaks in the IR spectra of CO adsorbed on catalyst surfaces extensive information on the nature of the surface can be gained.[16]

In this thesis an attenuated total reflection FTIR (ATR-FTIR) spectrometer is used to perform IR analysis. In FTIR spectroscopy a broad frequency beam of IR radiation, generally ranging from 600 to 4000 cm^{-1}, is shone onto the sample. A detector monitors the intensity of the different frequencies and by altering the relative intensities of the different frequencies in the incident radiation, the amount of each frequency absorbed by the sample can be determined. This data then undergoes a Fourier transform to give the relative absorption of each frequency, generating the final FTIR spectrum. ATR-FTIR spectroscopy combines FTIR spectroscopy with a system to improve the ability of IR to be performed on materials that

strongly absorb IR and/or present other issues that hinder the use of traditional transmission techniques. Figure 2.5 depicts a multiple internal reflection ATR setup, in the technique infrared radiation is passed through a material with a high optical density (such as a ZnSe crystal) at an angle such that total internal reflection occurs. When total internal reflection occurs an evanescent field is formed that extends beyond the crystal surface.

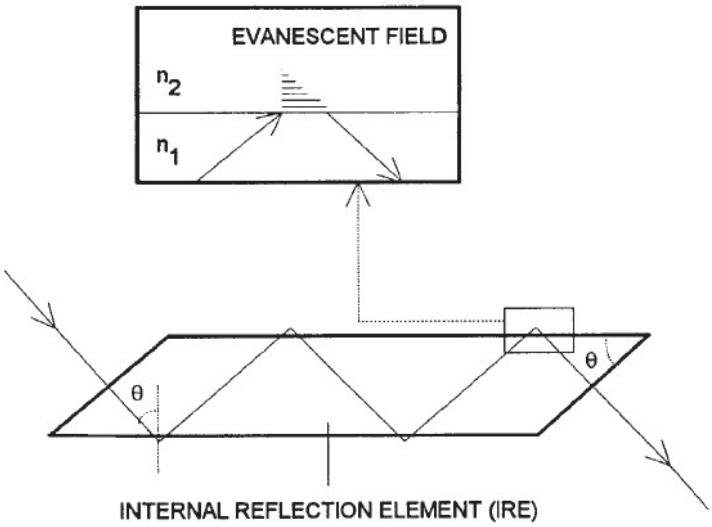


Figure 2.5– Schematic of an ATR crystal with multiple internal reflections.
Reproduced from reference[7]

A thin-film of the sample to be examined by ATR-FTIR is placed onto the crystal and, if a powder, pressed down to provide a tight contact between the crystal and sample. The evanescent wave of the IR radiation then extends from the surface and can interact with the sample. Specific frequencies of the IR evanescent field are absorbed and monitored by the FTIR detector, resulting in a typical IR spectrum. By increasing the number of reflections in the crystal the amount of interaction with the sample is increased, which can result in a highly sensitive technique to monitor catalyst surfaces.

2.9 References

[1] H. Knozinger, K. Kochloefl, *Heterogeneous Catalysis and Solid Catalysts*, Wiley-VCH, **2003**.

[2] J. M. Thomas, W. J. Thomas, *Principles and Practice of Heterogeneous Catalysis*, Wiley-VCH, **1997**.

[3] G. A. Somorjai, J. Carrazza, *Industrial & Engineering Chemistry Fundermentals* **1986**, *25*, 63–69.

[4] A. Ruban, B. Hammer, P. Stoltze, H. L. Skriver, J. K. Nørskov, *Journal of Molecular Catalysis A: Chemical* **1997**, *115*, 421–429.

[5] S. Alayoglu, A. U. Nilekar, M. Mavrikakis, B. Eichhorn, *Nature Materials* **2008**, *7*, 333–338.

[6] K. Tedsree, C. W. A. Chan, S. Jones, Q. Cuan, W.-K. Li, X.-Q. Gong, S. C. E. Tsang, *Science (New York, N.Y.)* **2011**, *332*, 224–228.

[7] D. Brune, R. Hellborg, H. J. Whitlow, O. Hunderi, *Surface Characterization A User's Sourcebook*, Wiley-VCH, **1999**.

[8] J. Rivière, S. Myhra, *Handbook of Surface and Interface Analysis: Methods for Problem-solving*, CRC Press, **2010**.

[9] C. R. Brundle, C. A. Evans, S. Wilson, *Encyclopedia of Materials Characterization*, Elsevier, **1992**.

[10] W. Clegg, A. Blake, J. Cole, *Crystal Structure Analysis: Principles and Practice*, Oxford University Press, **2001**.

[11] "How the TGA works," can be found under https://sites.google.com/site/isumate453lab10group8/how-the-tga-works, **2011**.

[12] N. Toshima, T. Yonezawa, *New Journal of Chemistry* **1998**, 1179–1201.

[13] P. Stoltze, *Introduction to Heterogeneous Catalysis*, **1997**.

[14] F. Menegazzo, M. Signoretto, T. Fantinel, F. Pinna, P. Canton, N. Pernicone, *Sciences at Ca' Foscari* **2012**, *3*, 87–94.

[15] G. C. Cabilla, L. Bonivardi, M. A. Baltan, *Science* **1998**, *55*, 147–156.

[16] C. Henry, *Surface Science Reports* **1998**, *31*, 231–325.

Chapter 3

Experimental and Characterisation Methods

Chapter 3 Experimental and Characterisation Methods 80
3.1 Synthesis of colloidal nanoparticles 81
3.1.1 PVP stabilised nanoparticles 81
3.1.2 Non-PVP stabilised nanoparticles 82
3.1.3 Decoration of colloidal nanoparticles 84
3.2 Synthesis of functionalised supports 84
3.3 Synthesis of supported palladium catalysts 85
3.3.1 Polymer modification of Pd/C 85
3.3.2 Synthesis of supported palladium 85
3.3.3 Decoration of supported palladium 86
3.4 Characterisation 86
3.4.1 XRD 86
3.4.2 XPS 87
3.4.3 TGA 88
3.4.4 TEM/EDX 88
3.4.5 FTIR 88
3.4.6 CO chemisorption 89
3.5 Catalyst testing 89
3.6 Computational details 90
3.6.1 DFT calculations 90
3.6.2 XRD simulation 91
3.7 References 92

3.1 Synthesis of colloidal nanoparticles

3.1.1 PVP stabilised nanoparticles

Glycol reduction

Polyvinylpyrrolidone (PVP) stabilised palladium nanoparticles (Pd-PVP) were synthesised using a modified polyol method used by Bonet *et al.*, with ethylene glycol or diethylene glycol as the solvent and reducing agent.[1] Pd-PVP particles were synthesised with a molar ratio of 1:10 of Pd to PVP monomer units; 0.166 g (1.5 mmol) of PVP was dissolved in 30 mL of glycol before 0.040 g (0.15 mmol) of $Pd(NO_3)_2$ was also dissolved by stirring under N_2. The light brown solution was then heated to 120°C at 5°C/min under a nitrogen atmosphere and held at this temperature for 100 minutes, turning dark brown as colloidal nanoparticles are formed. Once cooled to room temperature, the particles were mixed with acetone and precipitated by centrifugation. The sample was washed three times with acetone and dried at room temperature in air for 12 hours.

Ethanol reduction

Pd-PVP particles reduced by ethanol reduction were synthesised by a similar method to Liu *et al.*[2] A molar ratio of 1:10 of Pd to PVP monomer units was again used. The reaction mixture was prepared as above except but 30 mL of ethanol was used instead of a glycol. This solution was then heated at 5°C/min to reflux for 3 hours, before allowing the sample to cool to room temperature. The nanoparticles were precipitated using acetone and hexane, washed three times with acetone and dried at room temperature in air for 12 hours.

Sodium borohydride reduction

Pd-PVP particles reduced by $NaBH_4$ were synthesised by a similar method to Du *et al*. for synthesis of size-controlled Pd particles.[3] Again the reaction mixture was prepared as with the glycol reduced sample except water was used as the solvent. A five times molar excess of sodium borohydride in 5 mL of water was then added drop-wise to the reaction mixture, before stirring for one hour to ensure complete reduction. The colloidal suspension was precipitated using acetone and hexane, washed three times with acetone and dried at room temperature in air for 12 hours.

3.1.2 Non-PVP stabilised nanoparticles

Colloidal nanoparticles stabilised by a range of polymers (details in table 1 and figure 3.1) were synthesised using an ethylene glycol reduction following the method detailed in 3.1.1, but with some modifications. The molar ratio of metal to monomer units was 1:15, to ensure the size of the palladium particles was between 1-10 nm for all polymers used. During the reaction particles stabilised by some of the polymers would form a dark black/brown precipitate, which was re-dispersed by sonication after cooling and prior to precipitation. The colloidal suspension was precipitated using acetone and hexane, washed three times with acetone and dried at room temperature in air for 12 hours.

Table 1– Properties of polymers used to stabilise colloidal Pd nanoparticles and to modify type 87L

Polymer	Abbreviation	Molecular weight	% wt. solution[a]
Poly(4-styrenesulfonic acid)	PSSA	75,000	18
Poly(acrylic acid)	PAAcid	35,000	35
Polyacrylamide	PAAmide	10,000	50
Polyethyleneimine, Highly branched	PEI	35,000	≥ 99
Poly(allylamine)	PAAmine	17,000	20

[a]All solutions are in water

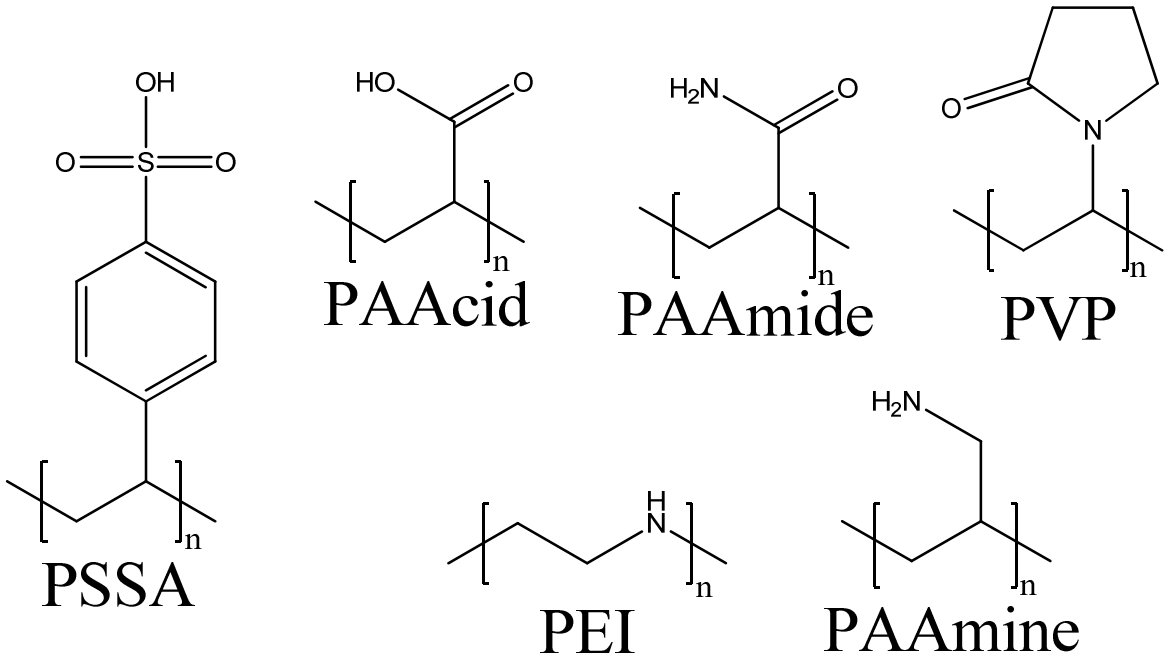


Figure 3.1– Structures of polymer monomers used to stabilise colloidal Pd nanoparticles and to modify type 87L

3.1.3 Decoration of colloidal nanoparticles

Decoration of Pd-PVP particles was performed by a redox method, similar to that used by Gauthard *et al.* with an additional reduction step.[4] Pd-PVP particles were synthesised using the ethylene glycol reduction method described in section 3.1.1, but stopped before the precipitation step. Once the reaction was cooled to room temperature the nitrogen was stopped and hydrogen was then allowed to flow through the solution at room temperature for 30 minutes, producing a Pd-H surface species. After hydrogen treatment the gas supply was switched to nitrogen and the required amount of decorating metal, dissolved in 5 mL of ethylene glycol, was added to the Pd-PVP colloidal suspension and stirred for 15 minutes. At this point a redox reaction occurred between the Pd-H and metal salt in solution, attaching the salt to the metal surface. An additional reduction step was then performed, ensuring total reduction of the decorating metal. The additional reduction methods used were re-heating the reaction in ethylene glycol, the addition of sodium borohydride and the addition of hydrazine. Ethylene glycol reduction was performed in the same way as production of Pd-PVP. For sodium borohydride and hydrazine reduction a four times excess of reducing agent was dispersed in 5 mL of ethylene glycol before being added drop-wise to the reaction mixture. After the reduction step the particles were precipitated using acetone and hexane, washed three times with acetone before being dried in air for 12 hours.

3.2 Synthesis of functionalised supports

Functionalised metal oxides were synthesised by a similar method to Harlick and Sayari.[5] Prior to functionalisation the metal oxide was pre-treated as required, typically dried under vacuum at 150°C. The prepared metal oxide was placed in a three-neck round bottom flask under a nitrogen atmosphere, before 50 mL of dry toluene was added and the metal oxide was

dispersed by stirring. The suspension was then heated to 85°C, if water is required, 0.3 mL of water was added the mixture stirred for 30 min, and then 1.27 moles of silane added. After stirring under nitrogen for 16 hours at 85°C, the reaction was filtered using a sintered glass funnel with maximum pore size of 1.6 μm. The powder was re-dispersed in hot toluene and filtered 10 times to remove excess silane, before drying at 100°C in air.

3.3 Synthesis of supported palladium catalysts

3.3.1 Polymer modification of Pd/C

For polymer modification of a commercial supported Pd/C catalyst, type 87L from Johnson Matthey was used. The amount of polymer to give the desired Pd to monomer mole ratio was dissolved in water and type 87L was then added and thoroughly dispersed by sonication. The reaction mixture was then stirred in a sealed flask for 48 hours, before the solvent was either evaporated or removed by filtration, with a 0.2 μm membrane filter. The filtered samples were additionally washed extensively with water. The polymer modified catalysts were then dried at 85°C for 12 hours.

3.3.2 Synthesis of supported palladium

Carbon supported palladium nanoparticles were synthesised using a deposition-precipitation method combined with an in situ hydrogen reduction, adapted from Park *et al.*[6] Briefly, 300 mg of Norit GSX carbon or metal oxide support was dispersed in 200 mL of water by extensive sonication and stirring, before the required amount of $Pd(NO_3)_2$ solution (to produce a sample with the desired percent weight Pd) was added. After stirring for 30 minutes, the

reaction mixture was adjusted to the required pH (8 or 11) by drop-wise addition of NaOH solution. Nitrogen was bubbled through the reaction mixture with vigorous stirring for 30 minutes. The gas was then exchanged to hydrogen, if required the reaction mixture was heated to the desired temperature, and stirring under hydrogen was continued at the desired temperature for 1 hour. The sample was then filtered using a 0.2 μm membrane filter and washed extensively with water until neutral. Then the sample was dried for 12 hours at 85°C.

3.3.3 Decoration of supported palladium

The palladium on Norit GSX carbon (Pd/C) synthesised by the method in section 3.3.2, was decorated using a similar method to the decoration of colloidal Pd-PVP and of Gauthard *et al.*[4] Typically, 200 mg of dried Pd/C with 10% weight palladium was dispersed in 120 mL of water and bubbled with hydrogen for 30 minutes. The required molar ratio of the decorating metal was dissolved in 5 mL of water and added to the hydrogen treated Pd/C dispersion. After stirring rapidly for 15 minutes, a four times excess of hydrazine in 5 mL of water was added drop-wise and stirring was continued for 1 hour. The sample was filtered using a 0.2 μm membrane filter, washed extensively with water and dried for 12 hours at 85°C.

3.4 Characterisation

3.4.1 XRD

To achieve the optimum results from XRD analysis colloidal and supported catalysts were prepared by different methods. For colloidal samples, the sample was dispersed in a minimum amount of water by sonication, before being drop cast on to a glass slide. This was then dried

under air, resulting in a thin film over the slide with even coverage. For supported samples the powder was placed in a fixed depth well on a glass slide and the surface was pressed level. Patterns were collected using a Philips PANalytical X'Pert Pro PW 1710 diffractometer operating in Bragg-Brentano focusing geometry with a generator at 40 kV and 40 mA producing $Cu_{K\alpha}$ radiation with a wavelength of 1.5406 Å. The patterns were collected between 20° and 90°.

3.4.2 XPS

Prior to XPS analysis catalysts were reduced under hydrogen for one hour. The recently reduced powders were attached to the sample stub by a sticky double sided carbon tab. Samples were analysed using a VG – Escalab X-Ray Photoelectron Spectrometer VGX900 using aluminium K_α radiation with an energy of 1486 eV, operating at $< 1 \times 10^{-8}$ mbar. A wide scan was performed to identify all elements present in the sample, an average of 5 scans between 0 and 1200 eV with a 1 eV step size, 0.1 second dwell time, and 50 eV pass energy. More intense, higher resolution spectra were collected for regions of interest as an average of 20 scans each using a step size of 0.1 eV and a 0.2 second dwell time, with a pass energy to of 20 eV. The resulting spectra were then analysed using CasaXPS peak fitting software with the C 1s peak set to 284.50 eV to calibrate the spectra, as used by Jansen and van Bekkum for studies of Norit carbon.[7]

3.4.3 TGA

Thermal gravimetric analysis was performed on a TA instruments Q50. Powdered samples were placed in a sample pan and loaded into the furnace of the TGA. Samples were heated at 10°C/min from room temperature to 950°C with a gas flow of 15 mL/min. over the sample and 30 mL/min. over the balance. The gases used were air or nitrogen. A 50 μL platinum pan and a 150 μL alumina pan were used depending on the sample to be analysed.

3.4.4 TEM/EDX

TEM was performed on a JOEL 2010 operating at 200 kV. EDX was performed using an Oxford Instruments LZ5 windowless energy dispersive X-ray spectrometer. Samples for TEM were prepared by dispersing the dry catalyst in ethanol using sonication before a drop was placed on a holey-carbon coated copper grid. The grid was then dried under vacuum for at least 1 hour.

3.4.5 FTIR

Infrared data was collected using a Nicolet 6700 ATR-IR spectrometer with a liquid-nitrogen-cooled MCT detector. The ATR attachment was smart golden gate-with ZeSe/diamond crystal surface. Spectra were obtained by averaging 128 scans from 650 to 4000 cm^{-1}. For the polymer stabilised colloidal samples, they were initially dissolved in approximately 2 mL of water and a drop of this solution was placed onto the crystal surface, after drying under air the spectra were collected. For analysis of catalyst supports a finely ground sample was placed directly onto the crystal surface and spectra collected. For analysis of CO adsorbed onto colloidal particles a spectrum of un-CO treated colloidal particles was first collected, as

before, and the solution of the sample was then treated with CO for 30 minutes before a spectrum of this was collected. If the spectra of the colloidal particles pre-CO treatment contain any peaks that interfere with the CO region, the pre- and post-CO treatment spectra were subtracted, removing the interfering peaks.

3.4.6 CO chemisorption

Prior to CO chemisorption measurements the sample was pre-treated *in situ* under helium for 15 minutes, reduced by 5% hydrogen in argon at 40°C for 1 hour, and finally flushed with helium for 1 hour. For type 87L Pd/C and polymer modified catalysts based on 87L, CO chemisorption measurements were performed on a CE instruments TPD/R/O 1100, with a pulse volume of 456 µL. For all other samples, the CO chemisorption measurements were performed using a Quantachrome Instruments ChemBET Pulsar TPR/TPD equipped with a loop with 75 µL pulse volume. In both cases an accurately weighed amount of sample, approximately 50 mg, was loaded into quartz tubes and contained with quartz wool. 99% CO was used as the pulse gas and helium was used as the flow gas, at least five pulses were performed after complete CO adsorption had occurred.

3.5 Catalyst testing

The activities of colloidal and supported catalysts were measured by gas evolution, using water displacement. For supported catalysts, an amount of catalyst containing approximately 4.25 mg of Pd was placed in a reaction vessel under a nitrogen atmosphere and 10.575 mL of 1.4M formic acid was added. For colloidal catalysts, samples containing 0.15×10^{-3} moles of Pd were dispersed in 5 mL of water and left for 12 hours. The colloidal suspension was then

added to a reaction vessel under nitrogen and formic acid solution was added, resulting in 15.860 mL of 1.4M formic acid solution. Reaction vessels were then stirred at 1000 rpm and the volume of gas produced was measured by water displacement in an upturned burette. The temperature was maintained at 22-25°C, unless stated otherwise. For analysis of the gas, a reactor was prepared as above and the gas produced was collected directly in a syringe before being injected into a GC with both a thermal conductivity (TCD) and flame ionization detector (FID) or into a GC-methanator FID. This allowed accurate detection of H_2, CO_2, CO and other gases, with a detection limit below 10 ppm for CO.

3.6 Computational details

3.6.1 DFT calculations

All DFT calculations were performed by Jin Qu, a fellow student in the Tsang group, in the framework of DFT using the Vienna ab initio simulation package (VASP).[8–11] The projector-augmented wave (PAW) potentials were used for the core electron interaction.[12,13] The Perdew–Burke–Ernzerhof (PBE) functional based on the generalised gradient approximation (GGA) was employed to evaluate the non-local exchange-correlation energy.[14,15] A plane wave basis set with a cut-off energy of 350 eV and a 2×2×1 k-point grid determined by the Monkhorst-Pack method were used. For structure optimization, the ionic positions were allowed to relax until the forces were less than that of 0.05 eV/Å.

The Pd(111) surface was modelled by a periodic slab model with four layers of metals. A 4×4 surface unit cell (11.171×11.171 $Å^2$) was utilised in this study and the bottom layer was fixed during all geometry optimizations. A vacuum layer of 15 Å along the z direction

perpendicular to the surface (the x and y directions being parallel to the surface) was employed to prevent spurious interactions between the repeated slabs.

Vibrational frequencies of CO stretching were calculated by applying the finite-difference method to create the Hessian matrix, which was diagonalised to obtain the characteristic frequencies of the system. An atomic displacement of 0.05 Å was used in the three directions of space. During the frequency calculation, as the coupling between molecular vibrations and surface phonons of adsorbate is negligible, all the atoms except CO, were not allowed to move.[16] The CO molecule was put in the bridge site on the surface to compare with the corresponding experimental FTIR peak and kept as far as possible from the co-adsorbed organics in the periodic model to minimise interactions.

3.6.2 XRD simulation

XRD simulations were performed by Dr Simon Fairclough in the Tsang group. The position of PdBi alloy peaks were calculated using Vegards Law, particles were modelled with the synthesised stoichiometric ratios of Pd and Bi assuming an FCC structure and using the bond lengths of bulk Pd and Bi.[17] A Pd@Ag core-shell particle was simulated by constructing a strained core-shell nanoparticle using a modified method of Fairclough *et al.* with various ratios of Ag over a 3.2 nm palladium core, the parameters used to construct the core-shell simulation are detailed in table 2.[17] The XRD pattern of the resulting particles were simulated using the 'DISCUS' program with a Cu k alpha source.[17,18]

Table 2– Crystal structure and physical properties of metals used for core-shell simulation

	Pd	Ag
Crystal structure	FCC	FCC
Lattice constant (Å)	3.8907	4.090
Bulk modulus (GPa)	180	100
Young's modulus	121	83
Poisson ratio	0.39	0.37

3.7 References

[1] F. Bonet, V. Delmas, S. Grugeon, R. Herrera Urbina, P.-Y. Silvert, K. Tekaia-Elhsissen, *Nanostructured Materials* **1999**, *11*, 1277–1284.

[2] Y. Zhang, J. Yu, H. Niu, H. Liu, *Journal of Colloid and Interface Science* **2007**, *313*, 503–510.

[3] Y. Wang, M. Du, J. Xu, P. Yang, Y. Du, *Journal of Dispersion Science and Technology* **2008**, *29*, 891–894.

[4] F. Gauthard, F. Epron, J. Barbier, *Journal of Catalysis* **2003**, *220*, 182–191.

[5] P. J. E. Harlick, A. Sayari, *Industrial & Engineering Chemistry Research* **2007**, *46*, 446–458.

[6] H. Cho, J. Park, B. Hong, Y. Park, *Bulletin of the Korean Chemical Society* **2008**, *29*, 328–334.

[7] R. Jansen, H. Van Bekkum, *Carbon* **1995**, *33*, 1021–1027.

[8] G. Kresse, J. Hafner, *Physical Review B* **1993**, *47*, 558–561.

[9] G. Kresse, J. Hafner, *Physical Review B* **1994**, *49*, 14251–14269.

[10] G. Kresse, J. Furthmiiller, *Computational Materials Science* **1996**, *6*, 15–50.

[11] G. Kresse, J. Furthmüller, *Physical Review B* **1996**, *54*, 11169–11186.

[12] P. Blöchl, *Physical Review B* **1994**, *50*, 17953–17979.

[13] G. Kresse, D. Joubert, *Physical Review B* **1999**, *59*, 1758–1775.

[14] J. Perdew, K. Burke, M. Ernzerhof, *Physical Review Letters* **1996**, *77*, 3865–3868.

[15] J. Perdew, K. Burke, M. Ernzerhof, *Physical Review Letters* **1996**, *77*, 3865–3868.

[16] A. Valca, J. M. Ricart, F. Illas, A. Clotet, *The Journal of Physical Chemistry B* **2004**, *108*, 18297–18305.

[17] S. M. Fairclough, E. J. Tyrrell, D. M. Graham, P. J. B. Lunt, S. J. O. Hardman, A. Pietzsch, F. Hennies, J. Moghal, W. R. Flavell, A. A. R. Watt, et al., *The Journal of Physical Chemistry C* **2012**, *116*, 26898–26907.

[18] T. Proffen, R. B. Neder, *Journal of Applied Crystallography* **1997**, *30*, 171–175.

Chapter 4

Polymer Modification

Chapter 4 Polymer Modification 94

4.1 Background 95

4.2 Objectives 97

4.3 Experimental details 98

4.4 Results and discussion 99

4.4.1 Colloidal synthesis method 99

4.4.2 Polymer stabilised palladium colloids 108

4.4.3 Polymer modified supported palladium 116

4.5 Conclusion 130

4.6 References 131

4.1 Background

The ability of molecular species to modify the properties of metal nanoparticles has been widely observed.[1–3] The term "unconventional promoter" has been coined to refer to the use of a molecular species in modifying either the electronic or geometric properties of a nanoparticle to promote its catalytic properties, rather than the traditional approach of using different metals or supports.[4] The unconventional promoter acts either through an electronic modification of the surface, with charge transfer occurring to or from the metal surface in a similar way to the electronic effects in transition metal complexes, or through a geometric effect with the molecules selectively binding to specific sites. The ability of molecules to adsorb on specific sites or crystal planes is highlighted by the use of molecular additives to produce shaped nanoparticles. Somorjai *et al.* found addition of NO_2 during the growth of Pd particles stabilised the (111) facets, through an interaction similar to its observed poisoning effects on Pd.[5] Controlling the concentration of NO_2 allowed the shape of resulting nanoparticles to be controlled from cubic to octahedral, due to the variation in relative stability of the facets.

Recently the addition of many small organic molecules (some of which are commonly considered to be poisons) to electro-catalysts has demonstrated the electronic and geometric influence they have on the surface, altering the catalytic properties. Adsorption of CO on a gold electrode was found to promote the electro-oxidation of methanol in an alkaline medium; CO_{ads} promoted OH adsorption, with charge transfer observed from CO to OH.[6] This activated OH species only occurs in close proximity to CO_{ads} and facilitates oxidation of methanol at much lower potentials.

The ability of molecular species to block surface sites is also highlighted by the common practice of removing the stabiliser after particle synthesis.[7,8] Stabilisers are adsorbed on the surface of individual particles providing steric repulsion from other particles and preventing aggregation; two classes of molecule are generally used, (i) small organic ligands consisting of an alkyl/allyl chain attached to a functional group, which adsorbs to the metal surface and (ii) large polymers whose pendent groups adsorb on the surface. Ligands are able to pack tightly together on the particle surface (figure 4.1a) and as such often result in very low activity catalysts. Polymers, on the other hand, are limited in the degree of surface blocking that can occur due to the ridged nature of the polymer (figure 4.1b); for this reason it is often found that polymer stabilised particles are used directly as catalysts without requiring the removal of the polymer.

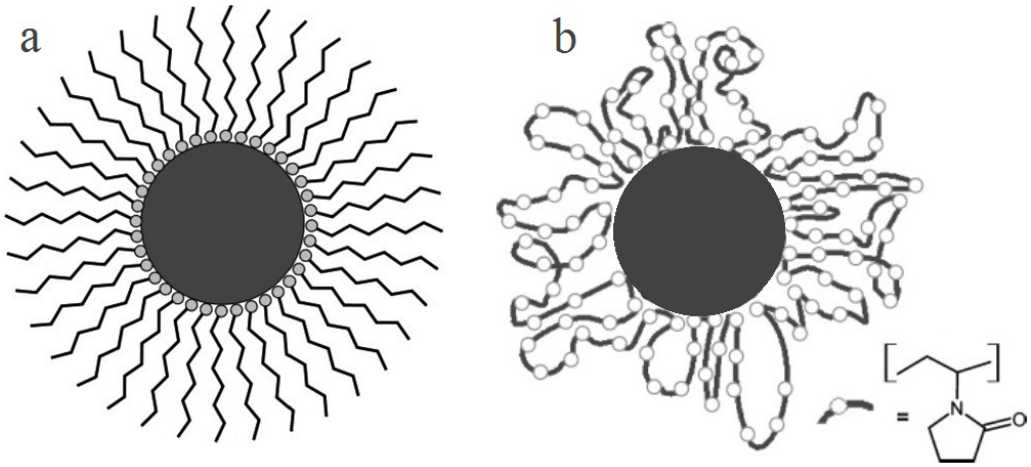


Figure 4.1– Schematic diagram of colloidal nanoparticles stabilised with (a) ligands and (b) polymer. Modified from references [9] and [1] respectively

Whilst there has been much interest into the effects of different polymers on the properties of stabilised metal nanoparticles, the interest has mainly revolved around the size, shape, solubility and stability of the particles rather than their catalytic activity.[10,11] Only recently has the electronic modification of surfaces by stabilising polymers been studied and the charge transfer been examined.[1,12] A wide range of polymers have been used to produce

metal nanoparticles but often the electronic and/or geometric alterations due to the polymer have been overlooked.[13]

The abilities of small molecules to modify catalytic activity has been more widely studied, which only serves to highlight the effects polymer pendent groups may have on catalyst performance. For example, the addition of alkyl thiols to pre-formed Pd particles is found to drastically increase the selectivity of epoxybutene hydrogenation to epoxybutane.[14] This is attributed to the thiols creating a self-assembled monolayer on the Pd surface. These organised layers have both an electronic and geometric influence on the surface, simultaneously blocking access of the larger epoxide ring while electron withdrawing effects destabilise adsorbed species, disfavouring bond breaking reactions. Thus, selectivity of the double bond hydrogenation increases from 11% to 94%. A similar approach has been used to increase selectivity in the conversion of cinnamaldehyde to cinnamyl alcohol; using a long chain alkyl amine, cinnamaldehyde can be prevented from binding to the surface in a flat configuration so hydrogenation of the double bond is prevented.[15]

4.2 Objectives

From the examples discussed in section 4.1, it is clear that the addition of certain molecular species to the surface of metal nanoparticles can have a large impact on their catalytic properties. While the electron-transfer from polymer to metal has been examined in some cases, the influence of polymer stabilisers, and molecular species added during nanoparticle synthesis, are often overlooked with regards to modification of catalytic properties. In this chapter we have two aims: primarily, to understand the effects that different polymers have on the surface properties of metal nanoparticles and secondly, to use the knowledge gained about

polymer interactions to modify the electronic and/or geometric properties of Pd nanoparticles to produce a highly active catalyst for the dehydrogenation of formic acid. This work will serve to highlight the potential of polymers to be utilised as a catalyst modification technique.

4.3 Experimental details

Extensive experimental details of the synthesis procedures, characterisation methods and catalysis testing are given in chapter three, a brief summary of catalyst synthesis is given here. Polyvinylpyrrolidone (PVP) stabilised palladium particles were synthesised with a 1:10 ratio of Pd to PVP monomer units. A range of reduction methods were used, namely, two polyol reductions (ethylene and diethylene glycol), ethanol reduction and a sodium borohydride reduction in water. PVP was dissolved in the required solvent prior to dissolving $Pd(NO_3)_2$. $Pd(NO_3)_2$ was then reduced to Pd^0 at the appropriate temperatures detailed in table 1. Once the reaction mixture had returned to room temperature, acetone was added and the nanoparticles were precipitated by centrifugation, washed three times with acetone, and dried in air.

Pd particles stabilised with a range of polymers were also synthesised using ethylene glycol as a solvent and reducing agent with a 1:15 molar ratio of Pd to monomer unit, similar to that used by Bonet *et al*.[16] To precipitate these particles a mixture of acetone and hexane was used due to the differing solubility of the different polymers in pure acetone. As above, samples were washed and dried in air at room temperature. For polymer modification of type 87L Pd/C, the catalyst and the required amount of polymer (for the desired Pd to monomer unit molar ratio) were dispersed in water and stirred for 48 hours before the solvent was removed by evaporation or filtering. The modified type 87L was then dried in air at 85°C.

4.4 Results and discussion

4.4.1 Colloidal synthesis method

Understanding the influence of polymer pendent groups on the surface of a catalyst is one of the key objectives of this chapter, but it is also noted that the preparation method is often instrumental in determining the activity of nanoparticle catalysts; as such, the synthesis method should be maintained for catalysts synthesised with all the different polymers.[17,18] Therefore a range of PVP stabilised palladium nanoparticles (Pd-PVP), with a 1:10 molar ratio of Pd to PVP monomer unit, were synthesised by varying the reduction method; the reduction methods selected are commonly used for the synthesis of colloidal metal nanoparticles, detailed in table 1.[16,19,20] In all cases, after heating or addition of the reducing agent, the light brown solution of $Pd(NO_3)_2$ turned dark brown indicative of the reduction from Pd^{2+} to Pd^0 colloidal nanoparticles.

The synthesis of Pd particles was confirmed by XRD, figure 4.2 displays a typical diffraction pattern for Pd-PVP. The strong agreement between the observed peaks and those reported for Pd metal in the Inorganic Crystal Structure Database (REF 064920) and the lack of peaks due to $Pd(NO_3)_2$ (ICSD 080658) confirms reduction to Pd metal. The peaks are assigned, left to right, to the (111), (200), (220), (311) and (222) reflections of face-centred cubic Pd, and the lattice parameter corresponding with reported values for Pd nanoparticles.[2,21] The successful formation of small nanoparticles is also evident from the broadness of the peaks, agreeing with the widely reported data for Pd nanoparticles.[22,23] All reduction methods produced similar diffraction patterns but with a variation in the peak broadening indicating different particle sizes; thus particle size was calculated from the (220) peak using the Scherrer equation and are displayed in table 1.

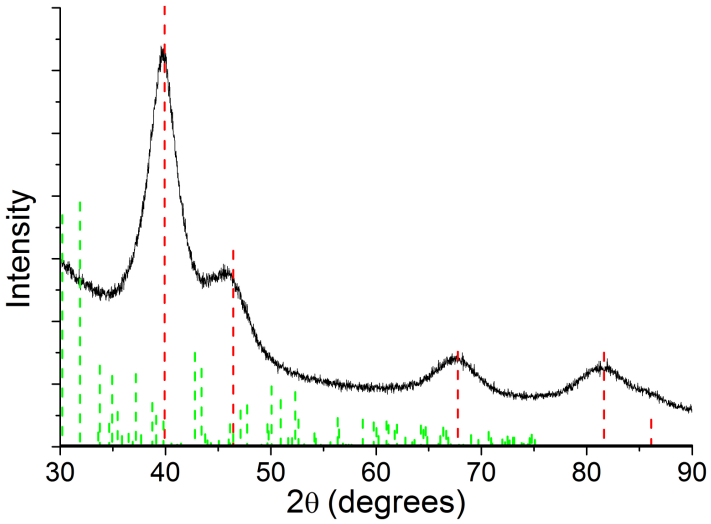


Figure 4.2– XRD pattern of Pd-PVP 1:10, reduced by ethylene glycol and ICDS peaks of Pd^0 and $Pd(NO_3)_2$, red and green lines respectively

The different synthesis methods resulted in particles with a narrow size range (2.4-3.9 nm); as the concentration of $Pd(NO_3)_2$ and PVP is the same in all cases, the differences in the rate of reduction and solvent viscosity are expected to account for the size changes.[24] The rate of reduction is determined by the strength of the reducing agent, or temperature of reduction, and the solvent viscosity determines the diffusion and growth processes. The low viscosity of ethanol and a slow reduction accounts for this method resulting in the largest particles, but slow reduction with high viscosity glycol solvents results in smaller particles. The higher rate of reduction of the glycols results in smaller particles than reduction with ethanol. The higher viscosity of diethylene glycol than ethylene glycol produces slightly smaller particles, under these conditions. In the case of $NaBH_4$, the very rapid reduction of Pd overcomes the low viscosity of water producing the smallest particles.

Traditionally the effects of catalysts with different particle sizes are accounted for by normalising the activity by the quantity of active sites on the metal surface, allowing the relative activity of sites to be determined; when the amount of active sites is unknown, the

activity is normalised by the total metal surface area.[25] In this case, and with many polymer stabilised colloidal nanoparticles, accurate determination of the surface area is not possible due to the presence of the polymer stabiliser. The methods traditionally used to determine the surface area of supported catalysts involve measuring the quantity of an adsorbed species, such as hydrogen/carbon monoxide chemisorption or electrochemical CO stripping, which are all inhibited by the polymer layer.[23,26] Determination of the surface area of these colloidal particles has been achieved by depositing them on a support and removing the polymer stabiliser to produce a typical supported catalyst, for which the surface area can be measured in the traditional way.[27] This approach has a number of draw backs; the removal of the polymer often requires the use of high temperatures, which can result in size changes, and contact with the support will block some metal surface area.

Table 1– Reaction conditions and details of resulting Pd-PVP nanoparticles

Reduction method	Reduction Temperature (°C)	Particle size (nm)[a]	Theoretical surface area (m^2 $g(Pd)^{-1}$)[b]
Ethylene Glycol	120	3.2	156
Diethylene Glycol	120	2.9	172
Ethanol	70	3.9	128
$NaBH_4$	0	2.4	208

[a]Particle size calculated by XRD from the Pd (220) peak; [b]Theoretical surface area calculated from size assuming a spherical particle.

An alternate approach, and the one that has been used here, is to calculate the theoretical surface area from the size of the particles. The particles are assumed to be spherical, a close approximation to cubo-octahedral particles (the most thermodynamically stable shape for fcc crystals) and in reasonable agreement with TEM results (displayed in chapter 6). [13,23,28,29] The surface area of a particle is calculated along with the number of particles in the sample,

resulting in the total surface area. In comparison, measurements by Tsang *et al.* of electrochemical CO stripping on 3.2 nm Pd-PVP particles - after deposition on carbon and thermal treatment to remove the PVP - found a surface area of 135 m^2 g^{-1}, which is in good agreement with our theoretical surface area of 156 m^2 g^{-1}.[23] Whilst calculating the surface area also has its drawbacks, such as no accounting for particle size distribution, its simplicity and reassurance that the particles have not altered during polymer removal make it ideal for this case.

A major limitation of both methods for determining the surface area of colloidal particles mentioned above, is that they do not account for the surface covered by the polymer, this means the actual active surface areas are likely to be much less than those measured or calculated.[25] Whilst these differences in surface area will result in subsequent errors in TOFs, by maintaining the ratio of metal to monomer units and the precipitation/washing procedure a similar degree of surface coverage by the polymer is expected, so comparison between these results will not be affected.

The Pd-PVP catalysts were tested for formic acid decomposition activity, figure 4.3 depicts the typical gas evolution from a Pd based catalyst over two hours at room temperature. The initial rate of gas production (evaluated for the first 10 min.) is much higher than the final rate (evaluated over the final 20 min.), this decrease is observed by the levelling off of the activity profile. This deactivation of Pd catalysts has been widely observed and though there has been some debate on its cause, it is currently regarded as the result of the dehydration reaction occurring on the catalyst surface.[30] The produced CO poisons the catalyst through its strong chemisorption to the surface and can migrate to sites active for formic acid dehydrogenation, preventing further decomposition.[31] Formic acid decomposition reactions are conducted

under a nitrogen atmosphere due to the ability of Pd to catalyse the reaction of hydrogen and oxygen to produce water; if the reaction is conducted under air a decreased initial activity is observed as the hydrogen produced is consumed by reacting with the oxygen present.

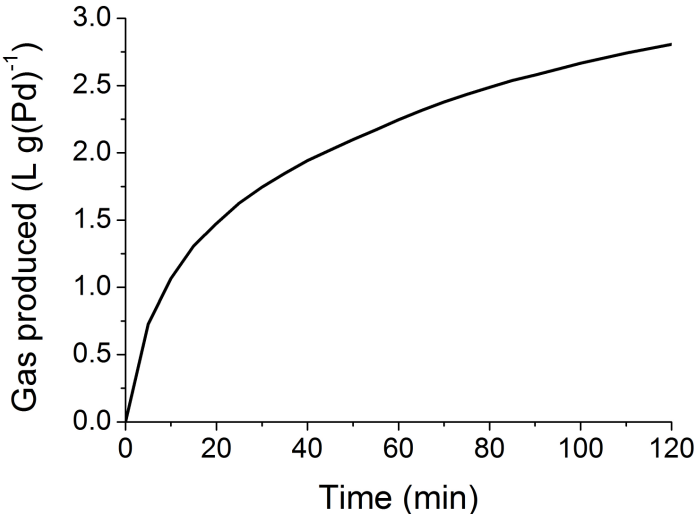


Figure 4.3– Activity plot of Pd-PVP 1:10 reduced by ethylene glycol at 120°C, $0.15x10^{-3}$ moles of Pd in 15.86 mL 1.4 M formic acid at 25°C

The gas produced by formic acid decomposition was analysed by gas chromatography (GC); it was possible to accurately detect H_2, CO_2 and CO along with most other common gaseous species. The only gaseous products observed were CO_2 and H_2, with approximately a 1:1 ratio, and the detection limit of CO was 5 ppm but in all cases no CO was observed; this is in agreement with the reports of Tsang *et al.* who found that CO was not detected in the product gas unless the sample was heated to 70°C.[23] This also supports the theory that the catalyst deactivation is caused by CO poisoning the catalyst, as any CO produced remains bound to the surface and is not released in the product gas under the testing conditions. Although the low level of CO (< 5 ppm) in the product gas makes it ideal for use in a hydrogen PEM fuel cell, the reduction in surface bound CO –due to formic acid dehydration– is desirable to increase catalyst lifetime and hydrogen production.

Table 2– Activity data of Pd-PVP 1:10 with different synthesis methods

Reduction method	Initial Rate[a] (L g(Pd)$^{-1}$ min^{-1})	Final Rate[b] (L g(Pd)$^{-1}$ min^{-1})	Deactivation[c]	Total Gas[d] (L g(Pd)$^{-1}$)	TOF[e] (h^{-1})
Ethylene Glycol	0.106	0.007	15.14	2.807	19.0
Diethylene Glycol	0.090	0.010	9.00	3.150	19.4
Ethanol	0.049	0.003	16.33	1.579	13.1
$NaBH_4$	0.141	0.011	12.82	4.098	20.9

[a]Rate of gas production in the first 10 min; [b]Rate of gas production in the final 20 min; [c]Deactiviation calculated from initial rate divided by final rate; [d]Total gas produced in 2 hours ($0.15x10^{-3}$ moles of Pd in 15.86 mL of 1.4M formic acid stirred at 25°C); [e] TOF (h^{-1}) calculated from the total moles of hydrogen produced divided by theoretical moles of Pd surface normalised for one hour.

Table 2 displays the activities of Pd-PVP reduced by different methods, and as expected the results are quite similar due to only small differences in the prepared catalysts. The only major exception is Pd-PVP reduced by ethanol, which show almost a 50% lower initial activity than the next worst catalyst and a much lower final activity. This significant difference from all other methods can be explained by ethanol, or its oxidation products such as acetaldehyde, binding strongly to the surface and blocking a large proportion of the active sites. Generally in the literature, alcohol reduction methods involve a high temperature pre-treatment step before catalytic testing to remove species blocking the surface.[7] Whilst this is possible for nanoparticles deposited on a support, it is not ideal for colloidal particles as it can result in damage to the polymer and significant changes in particle structure.

For the other reduction methods, the rate of gas production is initially quite variable (table 2), but the final rates vary substantially less, this is due to differing levels of CO production occurring on the catalyst surfaces. The amount of CO produced over the two hours can be inferred by dividing the initial rate by the final rate, giving a quantified level of activity loss.

Whilst the initial and final activities will be dependent on surface area, the deactivation should be independent of surface area and allow a measure of catalyst selectivity. Figure 4.4 displays the paths for formic acid dehydrogenation and dehydration and includes a schematic representation of the reported sites that these reactions occur on.

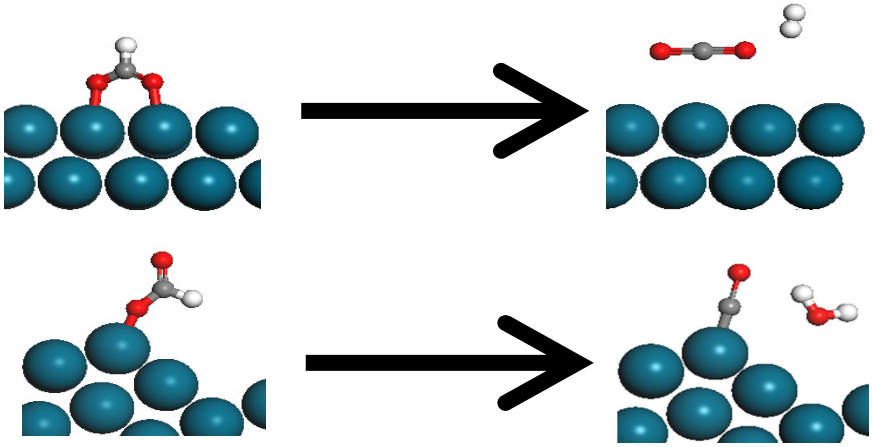


Figure 4.4– Illustration of the reaction mechanism of formic acid decomposition on different Pd surface sites. Reproduced from reference[23]

As the decomposition of formic acid has been reported to be structure sensitive on Pd surfaces, in agreement with the proposed mechanism of electrochemical decomposition on Pt and Pd, the structure of the surface was investigated using FTIR of adsorbed CO.[23,32] FTIR of adsorbed CO is a widely used technique for characterising catalyst surfaces where CO binds in a linear or bridging mode on Pd, with its preference dependent on surface coverage and the coordination number of the surface sites.[33] At low coverages, linear CO is observed between 2040-2070 cm^{-1} and is preferred on low coordinated sites (corners or edges) bound to the atop site of a single Pd atom; whereas bridging CO, observed between 1910-1960 cm^{-1}, is the preferred binding mode on flat surfaces (terraces).[23,33] Thus, the difference in the ratio of these peaks for the Pd-PVP particles synthesised by different methods will allow the surfaces to be characterised.

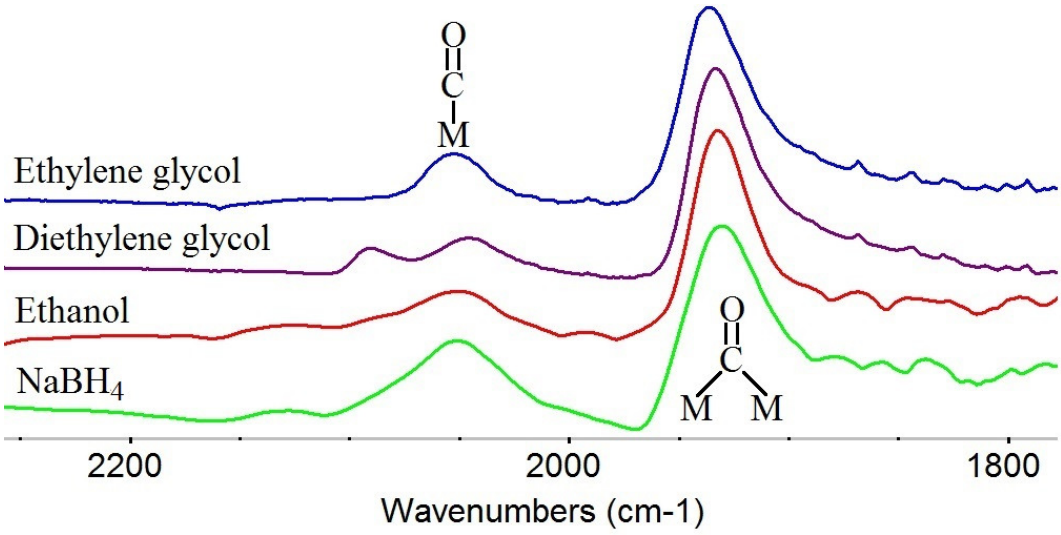


Figure 4.5– FTIR of CO adsorbed on Pd-PVP 1:10 reduced by different methods

In figure 4.5 it is apparent that the different reduction methods have resulted in particles with different proportions of low coordinate sites; this is expected as, demonstrated in chapter one with the calculations of van Hardeveld and Hartog, the change in size also results in a change in the ratio of terrace, edge, and corner sites. Another feature of the reduction method that can influence the proportion of low coordinate sites is the rate and temperature of reduction; slow reduction and/or high temperatures are expected to produce more thermodynamically stable surfaces, whereas low temperatures and/or rapid reduction result in less thermodynamically stable surfaces with more defect sites. As expected, the particles formed by $NaBH_4$ reduction are the smallest particles with the highest ratio of linear CO, as $NaBH_4$ is the strongest reducing agent and reduction is performed at the lowest temperature. Particles reduced by ethanol, a weak reducing agent, undergo slow reduction at a high temperature and result in a low ratio of linear CO, indicative of a low proportion of low coordinate sites.

For the glycol reductions both reduced at 120°C, the degree of linear CO is related to the rate of $Pd(NO_3)_2$ reduction; ethylene glycol, the stronger reducing agent, results in faster reduction, giving more defective surfaces with higher proportion of low coordinate sites than

for diethylene glycol. Both glycol reductions give levels of linear CO between that of the ethanol and $NaBH_4$ reduced samples.

The presence of additional species on the surfaces of both ethanol and $NaBH_4$ (figure 4.6) reduced Pd-PVP results in the expected relationship between the proportion of low coordinate sites and catalyst deactivation - high deactivation with a high proportion of low coordinates sites due to high CO formation - not being observed. In the case of the two glycol reduced samples, the expected relationship is observed with the ethylene glycol sample deactivating significantly more than the diethylene glycol sample over two hours.

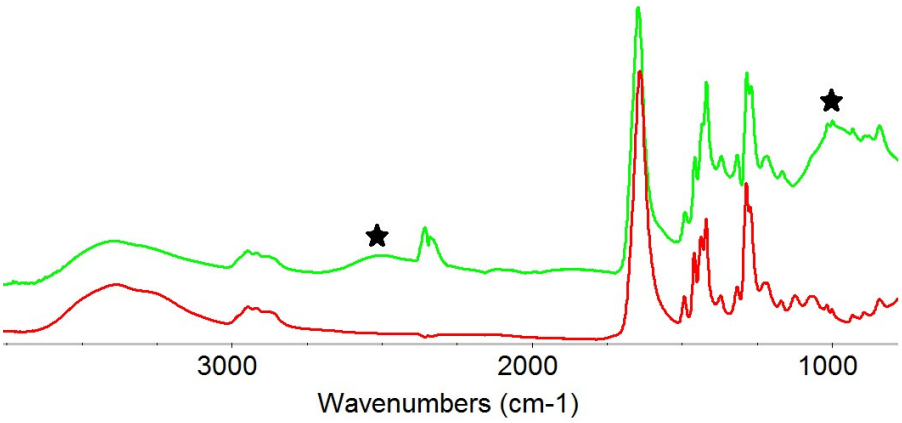


Figure 4.6– FTIR of Pd-PVP synthesised by ethylene glycol reduction (red) and NaBH4 reduction (green). Black stars indicate boron species

From the FTIR displayed in figure 4.6 additional peaks can clearly be seen in the spectra of the $NaBH_4$ reduced catalyst. The majority of peaks present in both samples are from PVP, but peaks marked with a star have been identified as the absorbance bands of boron oxide; the double peak at 2350 cm^{-1} is from atmospheric CO_2.[1,34] The presence of boron in Pd nanoparticle samples synthesised using $NaBH_4$ reduction has been noted by Cai *et al.*, who found 2.9% atomic percent boron in a Pd/C catalyst even after extensive washing.[35] The presence of boron oxide may play a role in limiting the deactivation of the Pd-PVP reduced by $NaBH_4$, similar to the effects attributed to a bismuth oxide species by Chan *et al.*[36] The

small particles display a high ratio of linearly bound CO indicative of a large number of low coordinate sites, which are expected to favour the dehydration pathway for the decomposition of formic acid that should result in rapid deactivation.[23] Although the Pd-PVP particles reduced by $NaBH_4$ show high activity and limited deactivation, the presence of boron on the surface would lead to complications in the study of polymer modification, and as such this method was not ideal for further study.

Accounting for the different particle sizes using the theoretical surface area gives very similar TOF's (19-21 h^{-1}) for all reduction methods except for ethanol, which is substantially lower for the reasons mentioned above. These TOF's are similar to those reported by Tsang *et al.*, who found a TOF of 25 h^{-1} for 3.2 nm Pd-PVP particles; the discrepancy is due to a difference in surface packing density used to calculate the moles of Pd on the surface of the particles ($1.0x10^{19}$ in their work vs. $1.27x10^{19}$ used for these results).[23] From the rate of reaction, deactivation, TOF and FTIR studies it is found that the most suitable reduction methods for producing a range of colloidal Pd nanoparticles stabilised with different polymers is by either of the glycol methods, as these resulted in particles with reasonable activity and surfaces free from any additional species.

4.4.2 Polymer stabilised palladium colloids

From the two glycol methods found to be most suitable for synthesis of Pd-PVP in section 4.4.1, ethylene glycol reduction at 120°C was selected for synthesis of Pd particles stabilised by a range of polymers with different pendent groups. Ethylene glycol reduction is a widely used method and should allow synthesis of nanoparticles stabilised by all of the desired polymers.[37] The moderate activity per gram and significant deactivation of the ethylene

glycol reduced particles also presented a wide range of potential promotion mechanisms. The polymers used to stabilise the Pd colloids are detailed in table 3 and illustrations of the monomer units are displayed in chapter 3; to ensure the synthesised Pd particles are all in the range of 1-10 nm (a common size range of metal nanoparticle catalysts) the ratio of Pd to polymer monomer units was increased to 1:15. This was kept constant for all polymers to ensure the same quantity of functional groups were present to modify the particle surface.

Table 3– Polymer properties and details of the resulting polymer stabilised Pd nanoparticles

Polymer	Molecular weight	Polymer length (monomer units)[a]	Particle Size (nm)[b]	Theoretical Surface area (m^2 g^{-1})[c]
Poly(4-styrenesulfonic acid), PSSA	75,000	410	9.5	52.5
Poly(acrylic acid), PAAcid	35,000	490	5.3	94.2
Polyacrylamide, PAAmide	10,000	140	4.0	124.8
Polyvinylpyrrolidone, PVP	40,000	360	3.1	161.0
Polyethyleneimine, branched, PEI	35,000	800	6.9	72.3
Poly(allylamine), PAAmine	17,000	300	2.5	199.7

[a]Polymer length calculated from molecular weight divided by monomer weight; [b]Particle size calculated by XRD from the Pd (220) peak; [c]Theoretical surface area calculated from size assuming a spherical particle.

It was not possible to purchase polymers with identical molecular weights, but a narrow range was selected. The influence of polymer molecular weight has previously been studied on nanoparticle synthesis and catalyst activity, and little variation in particle size (7.4-8.7 nm) is observed for changing PVP molecular weight from 10,000 to 360,000 with the dominant effect attributed to changing the number of chains present.[38] On the other hand, the effect of PVP molecular weight on the activity of Pd-PVP particles was found to be more significant;

the amount of PVP adsorbed on the particle surface was found to increase with molecular weight, reducing surface area available to perform the hydrogenation of 1,3-cyclooctadiene.[39] The change in average polymer length (number of monomers) is clearly highly influential on the number of functional groups able to bind to the surface and as such we compared this property. Due to varying monomer weights, length does not correlate with molecular weight (table 3) but the length of the polymers is quite similar. Thus, a similar number of functional groups are expected to be able to bind to the surface of the particles; the exceptions are PEI and PAAmide, which have approximately double and half the typical chain length, respectively, suggesting the number of groups bound to the surface may be quite different.

The ability of the polymers tested to stabilise Pd nanoparticles is clearly quite different, as the particle sizes vary widely (table 3). The different stabilisation of Pd^{2+} ions in solution prior to reduction, and the strength of interactions with the particle surface have been shown to be influential in determining the size of colloidal nanoparticles and is likely the case here.[40] The activity of these particles for formic acid decomposition, displayed in table 4, indicate that the increase in the ratio of monomer units significantly decreases the activity of the colloidal particles; the TOF of Pd-PVP decreases from 19 h^{-1} to 4.6 h^{-1} on increasing the Pd to PVP from 1:10 to 1:15, attributed to the 50% increase in polymer resulting in more pendent groups bound to, and blocking, the surface. The rate of deactivation is also significantly reduced from the 1:10 particles, which is also attributed to the increased quantity of polymer blocking low coordinate surface sites and, as has been reported by Choo *et al.*, increasing particle stability.[38]

Table 4– Activity of different polymer stabilised Pd particles for formic acid decomposition over 1.5 hours

Catalyst	Initial Rate[a] (mL g(Pd)$^{-1}$ min^{-1})	Final Rate[b] (mL g(Pd)$^{-1}$ min^{-1})	Deactivation[c]	Total Gas[d] (L g(Pd)$^{-1}$)	TOF[e] (h^{-1})
Pd-PSSA	6.89	2.10	3.28	0.307	4.1
Pd-PAAcid	21.30	3.29	6.47	0.626	4.7
Pd-PAAmide	25.69	3.76	6.83	0.633	3.6
Pd-PVP	36.34	6.11	5.95	1.059	4.6
Pd-PEI	29.45	26.94	1.09	2.256	22.0
Pd-PAAmine	126.57	64.85	1.95	8.195	29.0

[a]Rate of gas production in the first 10 min; [b]Rate of gas production in the final 20 min; [c]Deactivation calculated from initial rate divided by final rate; [d]Total gas produced in 1.5 hours (0.15×10^{-3} moles of Pd in 15.86 mL of 1.4 M formic acid stirred at 25°C); [e] TOF (h^{-1}) calculated from the total moles of hydrogen produced divided by theoretical moles of Pd surface normalised for one hour.

The total reaction time was reduced from 2 hours for the Pd-PVP 1:10 catalysts to 1.5 hours due to the high activity of Pd-PAAmine. Interestingly, it was found that the pendent group of the polymer could dramatically alter the activity of the Pd colloids and also the deactivation of the catalysts. Particles stabilised by either of the polymers containing amine functional groups resulted in higher TOF's than even the most active Pd-PVP 1:10 catalysts (table 2) and stabilisation by PAAmine results in almost double the volume of gas produced in only three quarters of the time. On the other hand, use of all other polymers resulted in similar TOF's, which were much reduced from the catalysts with lower polymer ratios. Although the TOF's of the amine catalysts were increased over the Pd-PVP 1:10 catalysts, the initial rates are lower than the $NaBH_4$ reduced catalyst (141 mL g(Pd)$^{-1}$) and Pd-PEI has a lower initial rate than all of the Pd-PVP 1:10 catalysts, even the sample reduced by ethanol. The very low

levels of deactivation of the amine stabilised catalysts (table 4), are clearly key to the high TOF's over 2 hours.

The interaction between the different polymers and the Pd surface was examined in two ways; first by FTIR of CO poisoned particles and secondly by computational modelling of the polymer functional groups on a Pd (111) surface. In FTIR of adsorbed CO the position of the peaks gives an insight into the electronic properties of the surface. Electron rich surfaces result in more electrons back-donated into the CO π* anti-bonding orbital, weakening the C=O bond and lowering its position in the infrared spectrum (cm^{-1}).[41] Thus, through monitoring the shift in position of bridging and linear CO the degree of electronic modification caused by the polymers could be probed, with substantial electronic modifications apparent. Figure 4.7 clearly shows that stabilising particles with PAAmine results in increased electron density on the Pd surface causing an increase in back-donation to the CO π* anti-bonding orbital and shifting the peaks to lower energy; whereas, PSSA and PAAmide result in less electron donation to Pd than PVP. This change in the electronic properties of the surface correlates with the initial rates of gas production, and agrees with the report by Tsang *et al.* stating that increased electron density on the surface accelerates the C-H bond cleavage in formic acid dehydrogenation.[23] Comparing the degree of electronic modification caused by stabilisation of Pd particles PAAmine with that reported by Tsang *et al.* for a Ag@Pd core-shell particle, we find that the polymer has almost double the effect with a shift of 19 cm^{-1} compared to only 11 cm^{-1} for Ag@Pd.

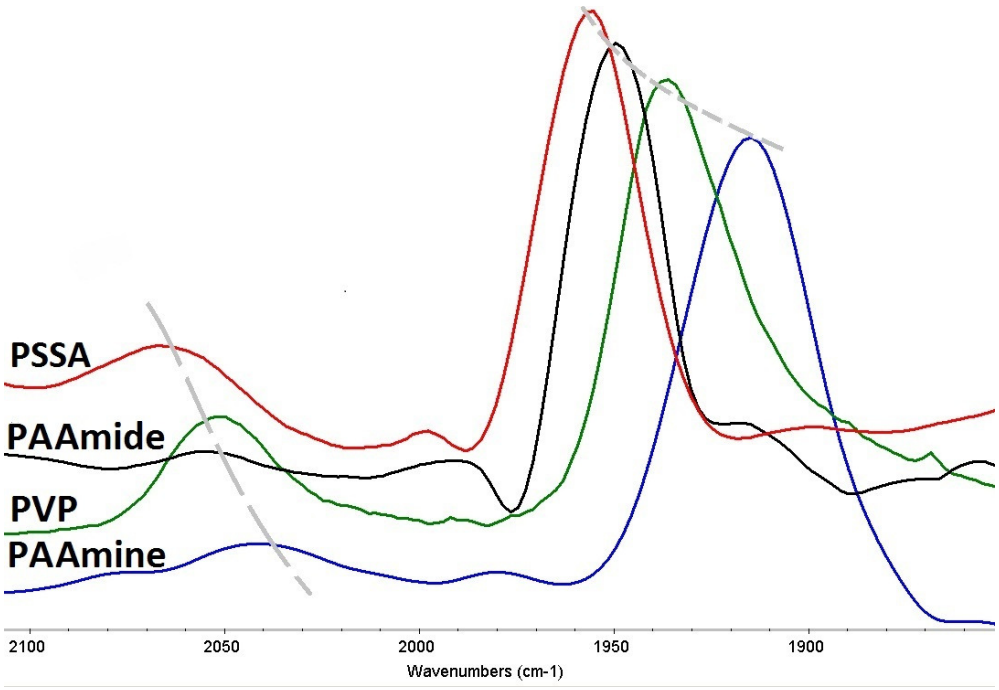


Figure 4.7– FTIR of CO adsorbed on polymer stabilised Pd nanoparticles, with a 1:15 ratio. Normalised by CO bridging peak

Whilst the degree of electronic modification explains the trend in the initial rate of gas production, it does not explain the changes in deactivation. Further examination of figure 4.7 demonstrates a significant difference in the intensity of the linear CO peak associated with low coordinate sites on the Pd surface.[31] Whilst it was not appropriate to quantify the changes in peak area due to the background not being well defined, it appears that PAAmine results in the lowest degree of linearly adsorbed CO, the opposite of what is expected given the small particle size. To understand these results we calculated the most stable binding modes of the functional groups on a Pd (111) surface, figure 4.8. PAAmine was modelled without the additional carbon in the pendent group to reduce processor time, but this is expected to have limited influence on binding geometry, and PSSA was not modelled due to the high computational demand posed by the large number of atoms in its pendent group.

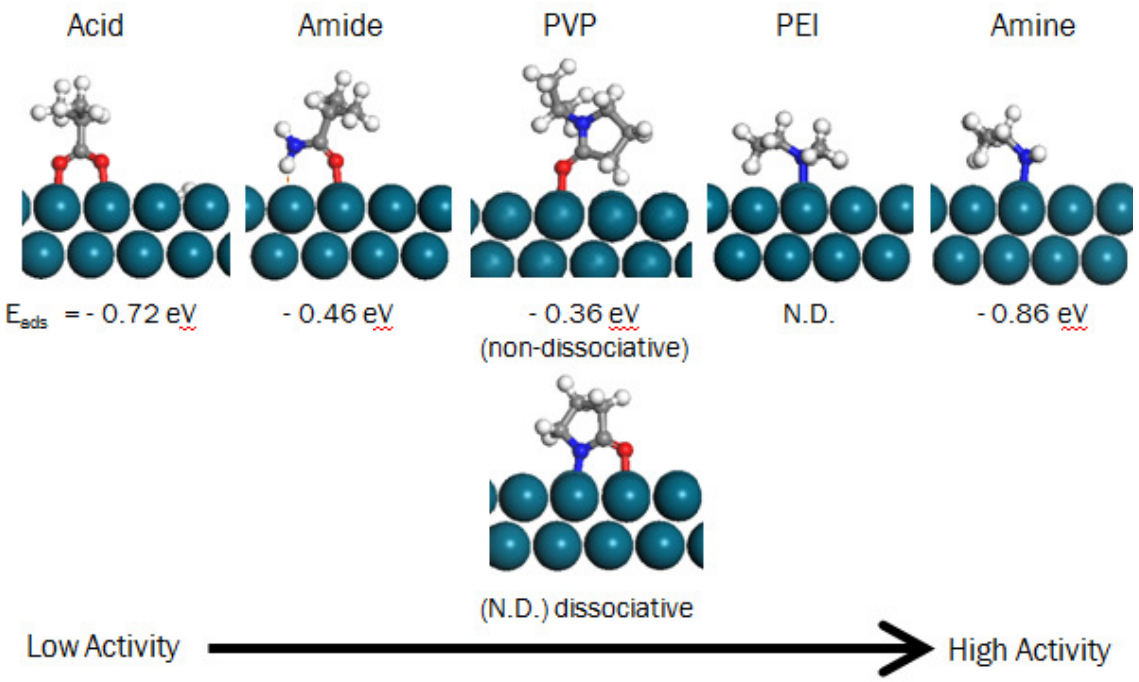


Figure 4.8– Calculated stable binding modes of polymer pendent groups and their energy of adsorption (E_{ads}). N.D=Not determined

The calculated binding modes show an interesting trend, all the groups with two hetero atoms prefer a bridging geometry on two Pd atoms, whereas the amine groups bind linearly to the atop site of a single Pd atom. PVP, which has been reported to be present in both the dissociated and non-dissociated forms on metal surfaces, is found in both bridging and linear modes.[1] PAAmide is found to form a bridging species, but unexpectedly the lone pair of nitrogen does not interact directly with the surface. Rather, a hydrogen atom is used as a bridge between surface and the nitrogen. This can be rationalised by the fact the lone-pair of nitrogen is resonant with the oxygen double bond and it appears loss of this ability to form a bond to the surface is unfavourable. From these different binding modes it is predicted that the different polymers will present a method for geometric modification of the catalyst surface. Amine-containing functional groups are expected to show a preference for low coordinate metal sites, as the single nitrogen only requires one atom to bind and low

coordinate sites generally bind adsorbates more strongly; whereas the other functional groups requiring two adjacent atoms will prefer to bind to terrace sites.[31]

The site preference of different adsorbates has also been examined by Ryu *et al.* who found that an atom with a single lone pair (nitrogen in methylamine) will show a strong preference for binding on corner sites, whereas an atom with two lone pairs (sulphur in methylthiol) will not show any site preference.[42] This strongly agrees with the low deactivation observed during formic acid decomposition for Pd particles stabilised by amine containing polymers, which indicates the amine pendent groups are blocking the low coordinate sites where the dehydration pathway would occur.

The difference between the degree of deactivation of Pd-PEI and Pd-PAAmine can be rationalised by the difference in size. Assuming cubo-octahedral particles and using the models of van Hardeveld and Hartog displayed in the introduction, the small Pd-PAAmine particles (2.5 nm) will have ~40% of atoms in corner or edge sites whereas the larger Pd-PEI particles (6.9 nm) will have less than 20%.[43] Thus, the low coordinate sites will be much more easily blocked in the case of Pd-PEI which accounts for the fact that there is almost no deactivation observed over 1.5 hours. The activity difference (TOF) can also be explained by comparison of the two polymers. Highly branched PEI contains a mixture of a mainly tertiary and secondary amines and although these would be expected to have increased electron donation (they are more basic) to the surface, they are sterically hindered preventing interaction, whereas PAAmine only consists of primary amines which can bind more freely to the surface.

The addition of sodium formate is widely reported to dramatically increase the rate of formic acid dehydrogenation over heterogeneous catalysts, but its role is debated. [30,44] It has been proposed that increasing the proportion of formate ions in solution either provides an alternate decomposition mechanism or that the formate ions remove poisoning species generated on the catalyst surface.[30,44] As such, the potential for our observed promotion to simply be due to an increase in formate ions in the solution must be considered.

Further comparison of the PEI and PAAmine stabilised catalysts strongly suggests that formate does not play a role in promoting the activity. As steric hindrance does not prevent the deprotonation of formic acid, and there is an equal number of pendent groups the more basic PEI (tertiary amines) will result in higher formate formation. But from table 4 we have seen Pd-PEI shows a much lower initial activity than Pd-PAAmine, even accounting for the lower surface area. Thus, the activity does not correlate with expected formate concentration, whereas the differences in activity can be rationalised from the steric hindrance in PEI, preventing nitrogen atoms interacting with the surface limiting the electronic effects. Additionally as will be demonstrated in section 4.4.3, reduced poisoning does not appear to be a result of formate because amine modified supported Pd catalysts still show significant levels of deactivation. The promotion in activity and selectivity is thus attributed to the modification of the electronic and geometric properties of the Pd nanoparticle surfaces by the polymer used to stabilise them.

4.4.3 Polymer modified supported palladium

The inability to accurately determine the surface area not covered by polymer and the potential for discrepancies in the polymer stabilised colloidal particles caused during

synthesis, such as size or different surface features, makes it preferential to modify preformed particles with polymers. There is also a preference for supported catalysts in order to provide the benefits of heterogeneous catalysts over homogeneous catalysts, such as the ability to use flow reactors. Thus, it was decided to modify a commercial 10% weight Pd on carbon, type 87L supplied by Johnson Matthey (JM), with the polymers tested previously. Type 87L was selected so a large quantity of identical catalyst would be available, ensuring any variation between samples was due to the polymer modification and not discrepancies in the initial catalyst. The ability of polymer modification to change the activity or selectivity of an existing catalyst would also demonstrate this technique as a potentially useful method for tuning the properties of a wide range of existing heterogeneous catalysts. Type 87L was extensively characterised before modification so any changes could be identified. In figure 4.9, it can clearly be seen that the as-received sample does not consist purely of Pd; although peaks corresponding to Pd metal (ICSD 064920) are observed, additional peaks are apparent which resemble PdO (ICSD 026598). A strong correlation can also be observed between the non-Pd peaks of the as received type 87L and the diffraction pattern of another commercial catalyst type 39 which is PdO supported on carbon, confirming the presence of PdO in the as-received catalyst.

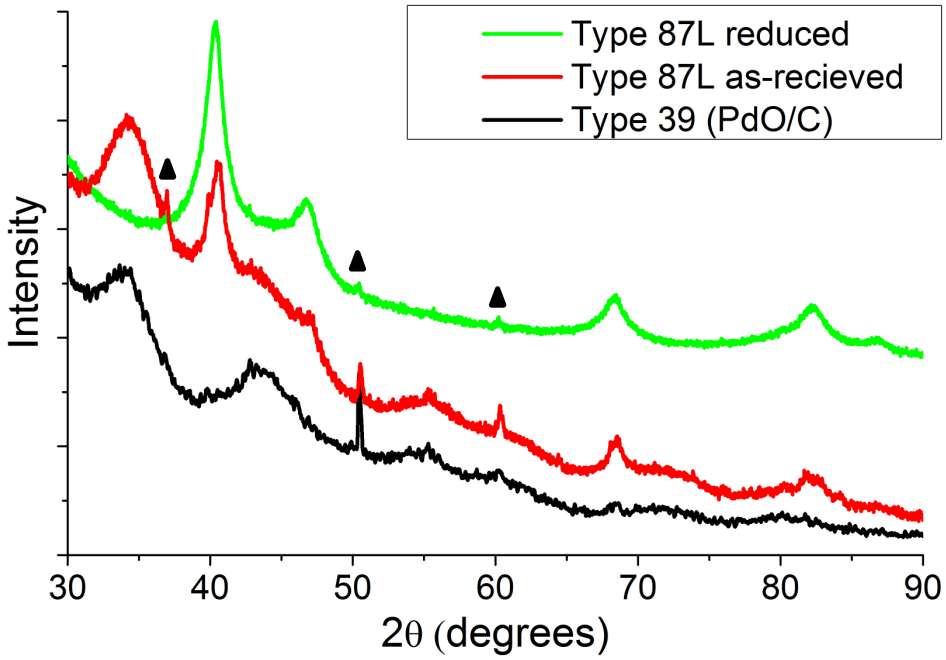


Figure 4.9– XRD of type 87L as received, type 87L reduced at room temperature and type 39 (PdO/C). Triangles mark peaks of a support impurity

The diffraction pattern of type 87L after reduction at room temperature under hydrogen for one hour clearly shows that the PdO is reduced and the intensity of the peaks corresponding to Pd metal increases. The reduced sample has been exposed to air before and during XRD analysis, indicating bulk oxidation does not readily occur at room temperature.

In all three XRD patterns a number of other small peaks are observed, marked with triangles, which are due to an impurity in the catalyst. Due to the commercial nature of the catalysts the identity of the carbon used as a support is not known, but these peaks are observed for both type 87L and type 39 supplied by JM; these peaks are also present for Norit GSX carbon from JM indicating they are from an impurity in the support. Treatment of Norit GSX carbon with base and washing extensively had no effect on the intensity of the impurity peaks, as such it was concluded the impurity was an integral part of the support rather than an impurity deposited on its surface. In the wide scan XPS of reduced type 87L (figure 4.10) the only

significant peaks observed are due to Pd, carbon and oxygen, indicating the impurity was at a very low level or not present on the surface of the carbon support.

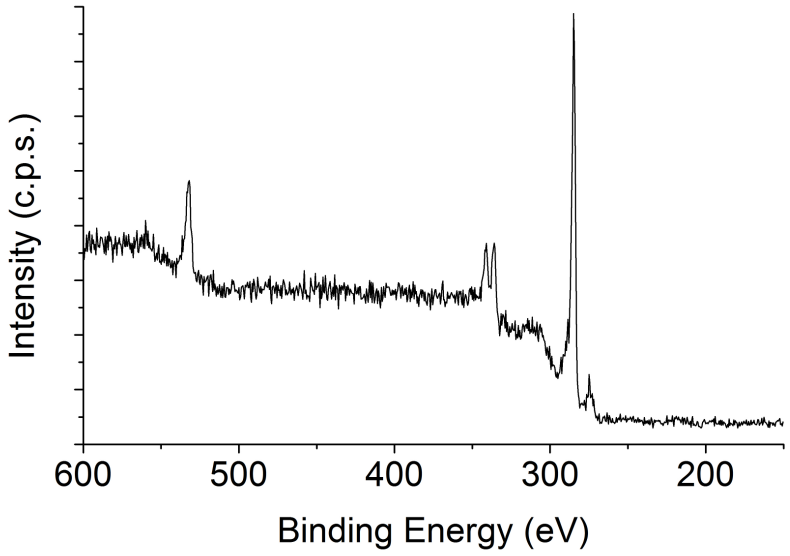


Figure 4.10– Widescan XPS spectra of reduced type 87L

A narrow scan of the Pd 3d region (figure 4.12) and deconvolution of the Pd $3d_{5/2}$ peak reveals two forms of Pd are present with binding energies of 334.9 eV and 336.2 eV; these correspond to Pd^0 and PdO, with ~35% in the oxide state.[45,46] Whilst it is clear from XRD that bulk oxidation of the Pd particles does not occur in air at room temperature, XPS indicates there is some surface oxidation; as the bulk oxide is reduced at room temperature, the surface oxide will also be reduced under a hydrogen atmosphere at room temperature and the formation of an oxide phase will only occur on exposure to atmospheric oxygen. Due to the production of hydrogen from formic acid decomposition, it is thus expected that the catalyst will be fully reduced during catalyst testing at room temperature.

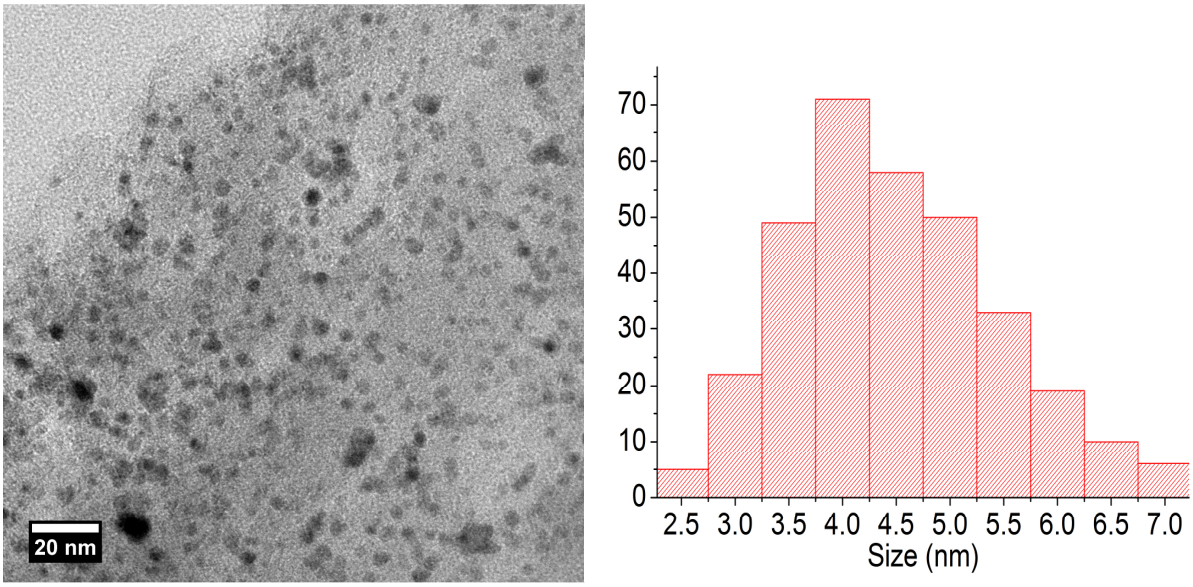


Figure 4.11– TEM micrograph and size distribution histogram of type 87L Pd/C

The size of the Pd particles in type 87L was determined by both XRD and TEM; from XRD the average size was calculated as 5.3 nm and from TEM the average size was 4.5 nm. The Pd surface area was also measured and found to be 85.1 m^2 $g(Pd)^{-1}$, this gave the size of the particles as 4.9 nm, assuming a shape factor of 5, in reasonable agreement with both TEM and XRD. TEM (figure 4.11) also shows the Pd particles to be quite well dispersed, with few regions of aggregated particles.

Once the commercial catalyst had been characterised, it was modified by the polymers tested in section 4.4.2. Polymer was added to type 87L, with a molar ratio of Pd to monomer unit of 1:5, by dispersing both polymer and catalyst in water and stirring for 48 hours before drying. The surface area of the polymer modified catalysts was measured using CO chemisorption and found to be 52.3, 60.6, 71.5, 60.8, 63.5 and 70.4 m^2 $g(Pd)^{-1}$ for the PSSA, PAAcid, PAAmide, PVP, PEI and PAAmine modified type 87L catalysts respectively, indicating the polymer had adsorbed on the metal surface. These catalysts were then tested for formic acid decomposition and compared to unmodified type 87L (table 5).

Table 5– Activity data of different polymer stabilised Pd particles for formic acid decomposition

Catalyst	Initial Rate[a] (L g(Pd)$^{-1}$ min^{-1})	Final Rate[b] (L g(Pd)$^{-1}$ min^{-1})	Deactivation[c]	Total Gas[d] (L g(Pd)$^{-1}$)	TOF[e] (h^{-1})
Type 87L	0.534	0.122	4.4	27.12	169
+PSSA	0.033	0.023	1.4	3.10	31
+PAAcid	0.079	0.023	3.4	4.44	39
+PAAmide	0.192	0.294	6.6	8.12	60
+PVP	0.235	0.030	7.7	9.51	83
+PEI	0.944	0.129	7.3	36.33	303
+PAAmine	1.665	0.351	4.7	81.97	616

[a]Rate of gas production in the first 10 min; [b]Rate of gas production in the final 20 min; [c]Deactivation calculated from initial rate divided by final rate; [d]Total gas produced in 2 hours (4.25 mg of Pd in 10.575 mL of 1.4 M formic acid stirred at 25^{o}C); [e] TOF (h^{-1}) calculated from the total moles of hydrogen produced divided by theoretical moles of Pd surface normalised for one hour.

Again the effects of the polymer are dramatic, with a polymer either greatly increasing or decreasing the activity of the unmodified catalyst depending on the pendent group. The general trend is found to be the same as with the colloidal particles, but comparison with the unmodified catalyst gives further insight into the polymer influence. An interesting difference between these results and those for the synthesised colloidal particles is the deactivation; the amine polymers no longer drastically reduce poisoning. The only polymers that result in a decrease in deactivation are PSSA and PAAcid, which are expected to bind preferentially on terrace sites, but as their activity is so low, the deactivation may be lower due to the vastly different turnover frequencies. The fact that deactivation is no longer reduced by the amine groups is likely due to rigidity of the polymer chains preventing them from selectively

blocking the low coordinate sites of the preformed nanoparticles; whereas for colloidal particles formed in the presence of the polymer, the pendent groups can attach selectively as the particles are formed. This idea is extended by Ryu *et al.* who found, computationally, that the presence of an amine group would induce the formation of corners at the site where it was bound.[42]

As we can now reference the effects of polymer modification to a bare Pd surface it is apparent that a number of polymers significantly reduce the catalysts activity, whereas previously it was only known they were less active than Pd colloids stabilised by PVP. Identification of the cause of this decreased activity is a key step in further understanding the role the polymer plays on the surface. FTIR analysis was not possible on the carbon supported materials, due to the high adsorption of carbon. Therefore, we computationally modelled CO and the polymer pendent groups co-adsorbed on a Pd (111) slab. The pendent groups and CO were adsorbed on the slab such that spatial interactions were limited, and from the strength of the corresponding C=O bond the IR stretch was calculated (table 6). An approximate 1.05 times variation between experimental (for colloidal Pd-Polymer 1:15 particles in section 4.4.2) and calculated data is observed, which is similar to that reported by Rösch *et al.* ascribed to the overestimation of interatomic distances in gradient-corrected DFT calculations.[47] Interestingly, it is clear that all polymers investigated result in a significant degree of electronic donation to the Pd surface, and all have a similar or greater influence than the introduction of an Ag core mentioned above.[23]

Table 6– Correlation of pendent group basicity with IR shift of CO (experimental and calculated)

Sample (monomer, pKa)	Bridging CO (cm^{-1})	
	Colloidal Pd-PolyX	Calculated
Pd	N/A	1847
+PSSA (-2.8)	1956	N/A
+PAAcid (4.4)	1948	1838
+PAAmide (5.5)	1949	1828
+PVP (6.8)	1936	1828
+PAAmine (9.7)	1915	1825

The pKa of the functional groups is also listed in table 6, a strong correlation is observed between it and the shift in wavenumbers of adsorbed CO. As discussed in section 4.4.2, the deprotonation of formic acid to formate as the key promotion mechanism has been ruled out and thus any shift in adsorbed CO must be primarily due to electronic modification of the surface.

XPS was performed on the polymer modified type 87L; figure 4.12 displays the Pd 3d region of PAAmine modified and unmodified type 87L where a clear shift to lower binding energy is observed after modification. Unfortunately the introduction of the polymers to type 87L made it insulating, resulting in charging effects that shift the binding energies to higher energies with prolonged exposure to x-rays. As a result of the charging effects, XPS could not be used quantitatively to compare the degree of electron donation from each polymer. However, the charging effects make the shift observed for PAAmine modified type 87L more significant as

the actual position of the Pd 3d peaks will be at an even lower binding energy, having been artificially shifted up by sample charging.

For amine modified type 87L the $3d_{5/2}$ peak again consists of two distinct Pd species, expected to be Pd^0 and a palladium oxide species. Both peaks are shifted from their positions in unmodified type 87L by approximately 0.7 eV, occurring at 334.2 eV and 335.5 eV, respectively, with ~25% of Pd in the sample oxidised. Following the reports of Tsang *et al.*, the more electron rich Pd explains the increased activity for formic acid decomposition. Identification of this charge transfer, similar to that observed in alloy or core-shell particles, indicates the polymer is electronically modifying the surface rather than having a spatial interaction with the adsorbed species.[37,48,49]

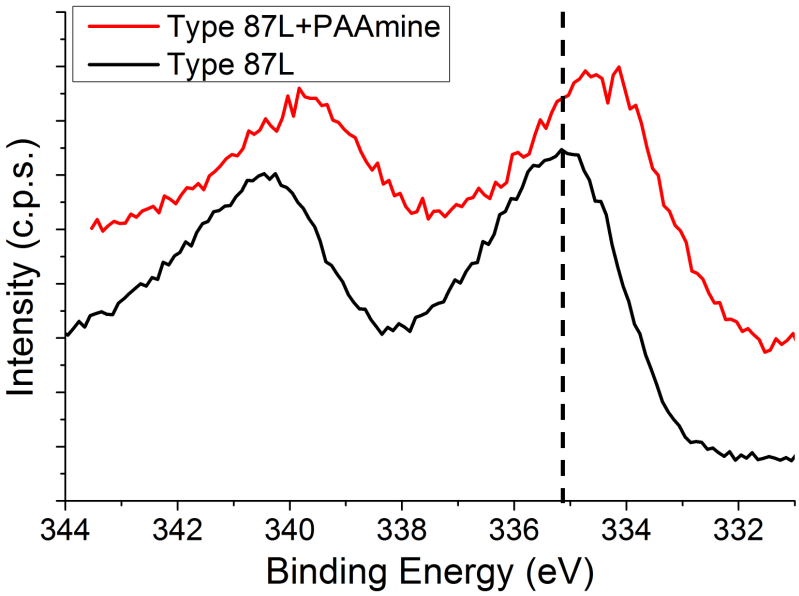


Figure 4.12– XPS spectra of type 87L and type 87L modified PAAmine, using a 1:5 ratio of Pd to PAAmine monomer unit

To further understand the modification of the particles electronic structure upon adsorption of the PAAmine pendent group, the density of states of the d-band (d-DOS) was modelled. Figure 4.13 displays the d-DOS for PAAmine modified and unmodified Pd(111) slabs; the x-

axis represents the energy of the states, with 0 eV being the position of the Fermi level, and the y-axis is the number of states at a particular energy. For the unmodified Pd(111) slab a large peak can be observed at -0.9 eV, whereas for the modified slab the largest peak is at -0.4 eV; thus there are more states at higher energies for the modified surface. The increasing density of states at higher energy, closer to the Fermi level, results in a raising of the d-band centre from -1.72 eV for Pd(111) to -1.56 eV for Pd(111)+PAAmine, relative to the Fermi level.

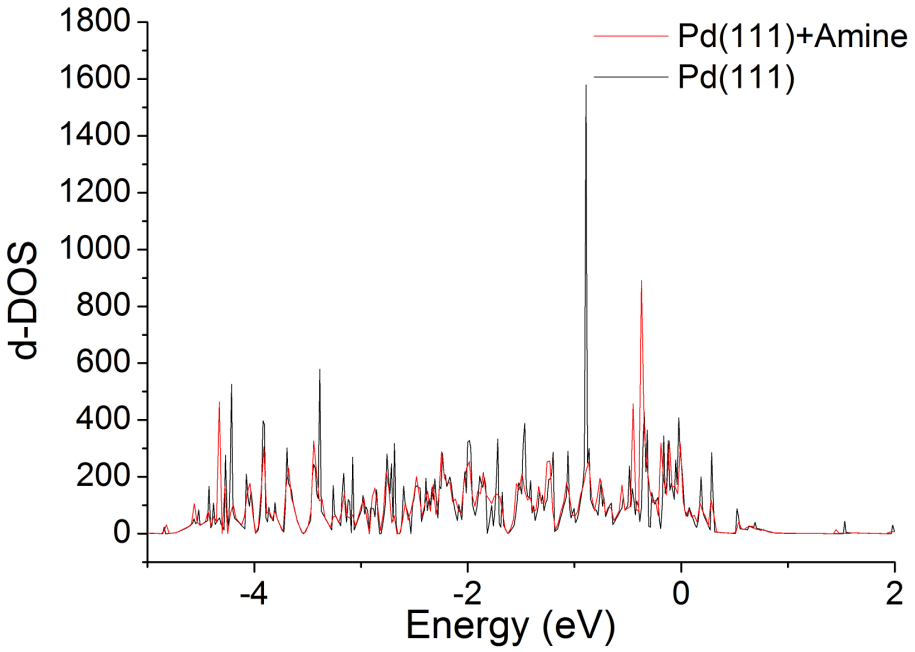


Figure 4.13– Calculated d-band density of states for Pd(111) and amine modified Pd(111)

Nørskov's d-band centre theory for the adsorption of simple molecules predicts that raising the band centre will result in a stronger surface-adsorbate bond; when the adsorbate binds the bonding (d-σ) and anti-bonding (d- σ)* states are formed, and a higher d-band centre results in less filling of the anti-bonding states giving stronger adsorption.[50] The stronger adsorption of small molecules to surfaces with higher d-band centres has been widely reported along with lower barriers to dissociation of adsorbates, which agrees with the increase in formic acid decomposition activity observed for reported catalysts containing electron rich Pd.[23,51,52]

Through the combination of experimental and computational results, particularly from the calculated IR stretching frequencies of CO, it is apparent that for all the polymers examined electronic donation occurs from the polymer to the Pd surface. Previous reports and theoretical models both predict this should increase formic acid decomposition activity, but a dramatic range of activities is observed in the modification of type 87L. By comparing the formic acid decomposition results for modified 87L with those of the colloidal particles and the calculated stable binding modes (figure 4.8) it is apparent that geometric effects must also play an important part in determining the activity of the modified catalysts. Whilst we have already noted that the amine containing functional groups do not show the same site selectivity for the supported catalysts likely due to polymer rigidity preventing site selective binding on the preformed particles, the general trend remains where species with bridging binding modes have low activities and those with linear modes have higher activities. This can be understood as the bridging bound polymers blocking the active sites for dehydrogenation of formic acid, so although they result in a more electron rich Pd surface the catalyst activity is decreased.

As the modification of type 87L with the amine polymers does not result in a decrease in deactivation and results in an increased initial activity even with the lower surface areas, the promotion effect appears to be dominated by electronic effects. As such, the effect of changing the polymer to Pd ratio is expected to have a significant influence on the activity. Figure 4.14 demonstrates the results of changing the molar ratio of Pd to monomer units of PAAmine and the effect of extensively washing the catalyst on the activity for formic acid decomposition.

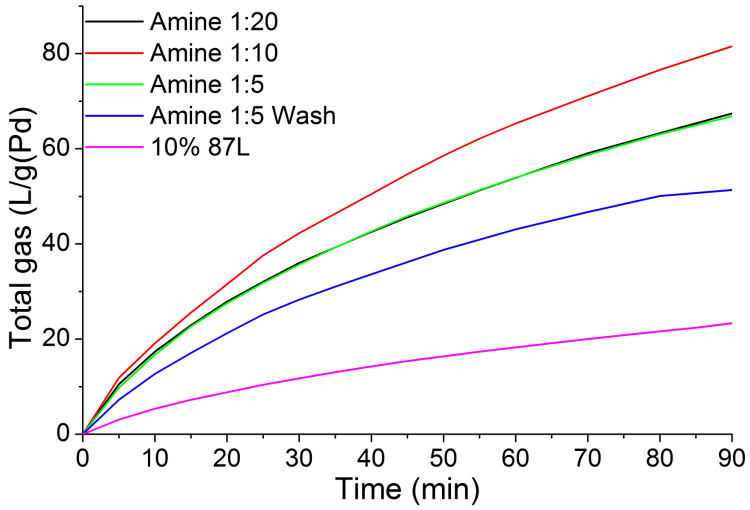


Figure 4.14– Activity plot of PAAmine modified type 87L. 4.25 mg of Pd stirred in 10.575 mL of 1.4 M formic acid at 25°C

Increasing the ratio of PAAmine to Pd results in a large decrease in effective surface area – measured as 70.5, 39.7 and 16.0 m^2 $g(Pd)^{-1}$ for 1:5, 1:10 and 1:20 ratios, respectively– demonstrating that more pendent groups are attaching to the surface. On testing these catalysts similar activity profiles are observed in all cases. If selective blocking of the low coordinate sites had occurred, a constant activity (straight line) would be expected due to reduced catalyst poisoning. As this is not the case and all catalysts display similar degrees of deactivation, the amount of electronic donation to the surface is clearly the dominant factor. In the case of the 87L + PAAmine 1:10, the electronic promotion clearly outweighs the loss in surface area resulting in the most active catalyst tested per gram Pd. At higher polymer content (1:20), the electronic promotion is not sufficient to overcome the loss in surface area and activity per gram drops. Comparing the initial TOF's of these catalysts (table 7), it is clear that the activity of the sites is dramatically increased with increasing polymer ratio, with the TOF approximately doubling as polymer ratio is doubled. This indicates that the more functional groups on the surface the more electronic promotion occurs, but when balanced with the losses in surface area it results in a typical volcano relationship.

So far all catalysts have been prepared by stirring in water followed by evaporation to ensure a specific ratio of metal to polymer; figure 4.14 displays the effect of extracting the catalyst from solution by filtration followed by extensive washing with water. A 23% loss in activity is observed upon washing with respect to the un-washed sample, but this washed catalyst still shows over double the activity of the unmodified catalysts. Although Hutchings *et al.* reported the complete removal of poly(vinyl alcohol) by washing, the persistence of a substantially increased activity after washing demonstrates that a significant amount of PAAmine is strongly bound to the surface and as such not removed.[8]

Table 7– Comparision of PAAmine modified type 87L with reported formic acid decomposition catalysts

Catalyst	Initial TOF (h^{-1})	Temperature (ºC)	State	Ref
Type 87L 10%	359	22	Heterogeneous	This work
87L + Amine 1:5 Water	1438	22	Heterogeneous	This work
87L + Amine 1:10 Water	2729	22	Heterogeneous	This work
87L + Amine 1:20 Water	6061	22	Heterogeneous	This work
Pd@Ag (1:1)	125*	20	Colloidal	[23]
Pd@Ag (1:1)	626*/500*	90/70	Colloidal	[23]
Pd@Ag(1:1)/C	192*	20	Heterogeneous	[23]
$Ag_{42}Pd_{58}/C$	382	50	Heterogeneous	[52]
$Au_{41}Pd_{59}/C$	210	50	Heterogeneous	[53]
$PdAg/C\text{-}CeO_2$	832/227	100/90	Heterogeneous	[30]
$(RuBr_3 \cdot xH_2O)/3PPh_3$	3630	40	Homogeneous	[54]
$[RuCl_2(PPh_3)_3]$	2688	40	Homogeneous	[55]
$[Ru(H_2O)_6](tos)_2$	460	120	Homogeneous	[56]

*TOF taken over 2 hours

The details of the methods used to calculate TOF's in table 7 vary widely –from the length of time to determine TOF to the use of total metal quantity rather than metal surface area– limiting the usefulness of their precise comparison. But table 7 clearly shows that the PAAmine modified type 87L catalysts are amongst the most active catalysts reported. Even

comparing initial TOF (table 7) with those over two hours (table 5), which include the effects of poisoning, displays the dramatic effects of PAAmine modification resulting in comparable results to alloy or core-shell catalysts operating at 50-90°C. The initial TOF's are also similar to those reported for some homogeneous catalysts, but these are maintainable for vastly extended periods of time with minimal deactivation.[54]

4.5 Conclusion

Through a combined approach of experimental and computational results we have demonstrated a substantial electronic donation from a range of polymer modifiers to Pd nanoparticles. From comparison with reports in the literature, the electronic donation from PAAmine to Pd appears to be almost twice that achieved through the use of an Ag@Pd core-shell structure. XPS also demonstrates the electronic effects for modification of an existing heterogeneous catalyst, although it is effected by sample charging, with a similar Pd shift observed as that of Pd in a Cu rich PdCu alloy.[48]

We have also demonstrated a significant geometric modification, with amine containing polymers showing selective blockage of low coordinate sites and polymers with two hetero-atoms blocking terrace sites. The blockage of low coordinate sites is observed more significantly for particles synthesised in the presence of polymer, as it is expected the semi-rigid polymers will have difficulty encapsulating the preformed supported particles. The effect of the site specific blocking is observed most clearly for Pd-PEI colloidal particles, which appear to have almost entirely supressed formic acid dehydration with over a 5 times reduction in deactivation compared to a typical Pd-PVP sample.

The combination of electronic and geometric factors in polymer modification highlights the importance of considering the influence of the polymer or any molecular additive(s) added during synthesis and also presents an alternate method for modifying heterogeneous catalysts. It shows that similar effects can be achieved through the addition of a polymer as are typically achieved by the production of bimetallic systems. This technique could be used to modify a wide range of existing metal catalysts currently operating in reactions at near ambient temperatures.

4.6 References

[1] Y. Borodko, S. M. Humphrey, T. D. Tilley, H. Frei, G. A. Somorjai, *The Journal of Physical Chemistry C* **2007**, *111*, 6288–6295.

[2] M. Ganesan, R. G. Freemantle, S. O. Obare, *Chemistry of Materials* **2007**, *19*, 3464–3471.

[3] C. Pan, K. Pelzer, K. Philippot, B. Chaudret, F. Dassenoy, P. Lecante, M. J. Casanove, *Journal of the American Chemical Society* **2001**, *123*, 7584–7593.

[4] Y. J. Tong, *Chemical Society Reviews* **2012**, *41*, 8195–8209.

[5] S. E. Habas, H. Lee, V. Radmilovic, G. A. Somorjai, P. Yang, *Nature Materials* **2007**, *6*, 692–697.

[6] P. Rodriguez, Y. Kwon, M. T. M. Koper, *Nature Chemistry* **2012**, *4*, 177–182.

[7] R. M. Rioux, H. Song, J. D. Hoefelmeyer, P. Yang, G. A. Somorjai, *The Journal of Physical Chemistry B* **2005**, *109*, 2192–2202.

[8] J. A. Lopez-Sanchez, N. Dimitratos, C. Hammond, G. L. Brett, L. Kesavan, S. White, P. Miedziak, R. Tiruvalam, R. L. Jenkins, A. F. Carley, et al., *Nature Chemistry* **2011**, *3*, 551–556.

[9] R. A. Sperling, W. J. Parak, *Philosophical Transactions. Series A, Mathematical, Physical, and Engineering Sciences* **2010**, *368*, 1333–1383.

[10] N. Yan, J. Zhang, Y. Tong, S. Yao, C. Xiao, Z. Li, Y. Kou, *Chemical Communications* **2009**, 4423–4425.

[11] I. Favier, M. Gómez, G. Muller, D. Picurelli, A. Nowicki, A. Roucoux, J. Bou, *Journal of Applied Polymer Science* **2007**, *105*, 2772–2782.

[12] K. S. Han, M. Lee, *Journal of the Korean Magnetic Resonance Society* **2009**, *13*, 135–142.

[13] R. Narayanan, M. A. El-Sayed, *Journal of the American Chemical Society* **2004**, *126*, 7194–7195.

[14] S. T. Marshall, M. O'Brien, B. Oetter, A. Corpuz, R. M. Richards, D. K. Schwartz, J. W. Medlin, *Nature Materials* **2010**, *9*, 853–858.

[15] B. Wu, H. Huang, J. Yang, N. Zheng, G. Fu, *Angewandte Chemie International Edition* **2012**, *51*, 3440–3443.

[16] F. Bonet, V. Delmas, S. Grugeon, R. Herrera Urbina, P.-Y. Silvert, K. Tekaia-Elhsissen, *Nanostructured Materials* **1999**, *11*, 1277–1284.

[17] M. Gurrath, T. Kuretzky, H. P. Boehm, L. B. Okhlopkova, A. S. Lisitsyn, V. A. Likholobov, *Carbon* **2000**, *38*, 1241–1255.

[18] N. Mahata, V. Vishwanathan, *Journal of Catalysis* **2000**, *196*, 262–270.

[19] H. Liu, H. Niu, J. Gao, *Chinese Journal of Polymer Science* **2003**, *21*, 1–4.

[20] P. Rodriguez, E. Herrero, J. Solla-Gullon, F. J. Vidal-Iglesias, A. Aldaz, J. Feliu, *Electrochimica Acta* **2005**, *50*, 4308–4317.

[21] W. Qi, B. Huang, M. Wang, *Nanoscale Research Letters* **2009**, *4*, 269–273.

[22] Y. Wang, M. Du, J. Xu, P. Yang, Y. Du, *Journal of Dispersion Science and Technology* **2008**, *29*, 891–894.

[23] K. Tedsree, T. Li, S. Jones, C. W. A. Chan, K. M. K. Yu, P. A. J. Bagot, E. A. Marquis, G. D. W. Smith, S. C. E. Tsang, *Nature Nanotechnology* **2011**, *6*, 302–307.

[24] A. R. Tao, S. Habas, P. Yang, *Small* **2008**, *4*, 310–325.

[25] A. P. Umpierre, E. de Jesús, J. Dupont, *ChemCatChem* **2011**, *3*, 1413–1418.

[26] F. Menegazzo, M. Signoretto, T. Fantinel, F. Pinna, P. Canton, N. Pernicone, *Sciences at Ca' Foscari* **2012**, *3*, 87–94.

[27] M. Crespo-Quesada, J. M. Andanson, A. Yarulin, B. Lim, Y. Xia, L. Kiwi-Minsker, *Langmuir* **2011**, *27*, 7909–7916.

[28] L. Marks, *Reports on Progress in Physics* **1994**, *57*, 603–649.

[29] C. Makowka, C. Slichter, J. Sinfelt, *Physical Review B* **1985**, *31*, 5663–5679.

[30] X. Zhou, Y. Huang, W. Xing, C. Liu, J. Liao, T. Lu, *Chemical Communications* **2008**, 3540–3542.

[31] K. W. Zilm, L. Bonneviot, G. L. Haller, O. H. Han, M. Kermarec, *The Journal of Physical Chemistry* **1990**, *94*, 8495–8498.

[32] N. Hoshi, M. Nakamura, K. Kida, *Electrochemistry Communications* **2007**, *9*, 279–282.

[33] J. S. Bradley, E. W. Hill, S. Behal, C. Klein, A. Duteil, B. Chaudret, *Chemistry of Materials* **1992**, *4*, 1234–1239.

[34] J. Parsons, M. Milberg, *Journal of the American Ceramic Society* **1960**, *54*, 326–330.

[35] J.-Y. Wang, Y.-Y. Kang, H. Yang, W.-B. Cai, *The Journal of Physical Chemistry C* **2009**, *113*, 8366–8372.

[36] S.-W. Ting, S. Cheng, K.-Y. Tsang, N. van der Laak, K.-Y. Chan, *Chemical Communications* **2009**, 7333–7335.

[37] K. Tedsree, C. W. A. Chan, S. Jones, Q. Cuan, W.-K. Li, X.-Q. Gong, S. C. E. Tsang, *Science (New York, N.Y.)* **2011**, *332*, 224–228.

[38] H. P. Choo, K. Y. Liew, H. Liu, *Journal of Materials Chemistry* **2002**, *12*, 934–937.

[39] H. Hirai, N. Yakura, Y. Seta, S. Hodoshima, *Reactive and Functional Polymers* **1998**, *37*, 121–131.

[40] C. D. Taboada, J. Batista, A. Pintar, J. Levec, *Applied Catalysis B: Environmental* **2009**, *89*, 375–382.

[41] R. Liu, B. Tesche, H. Knozinger, *Journal of Catalysis* **1991**, *129*, 402–413.

[42] J. H. Ryu, S. S. Han, D. H. Kim, G. Henkelman, H. M. Lee, *ACS Nano* **2011**, *5*, 8515–8522.

[43] R. Van Hardeveld, F. Hartog, *Surface Science* **1969**, *15*, 189–230.

[44] B. Zaidman, H. Wiener, Y. Sasson, *International Journal of Hydrogen Energy* **1986**, *11*, 341–347.

[45] J. He, T. Kunitake, A. Nakao, *Chemistry of Materials* **2003**, *15*, 4401–4406.

[46] B. V. Crist, *Handbook of The Elements and Native Oxides*, Wiley, **2000**.

[47] I. V. Yudanov, R. Sahnoun, K. M. Neyman, N. Rösch, J. Hoffmann, S. Schauermann, V. Johánek, H. Unterhalt, G. Rupprechter, J. Libuda, et al., *The Journal of Physical Chemistry B* **2003**, *107*, 255–264.

[48] M. B. Boucher, B. Zugic, G. Cladaras, J. Kammert, M. D. Marcinkowski, T. J. Lawton, E. C. H. Sykes, M. Flytzani-Stephanopoulos, *Physical Chemistry Chemical Physics: PCCP* **2013**, *15*, 12187–12196.

[49] C.-W. Yi, K. Luo, T. Wei, D. W. Goodman, *The Journal of Physical Chemistry B* **2005**, *109*, 18535–18540.

[50] B. Hammer, J. Nørskov, *Advances in Catalysis* **2000**, *45*, 71–129.

[51] T. Bligaard, J. K. Nørskov, *Electrochimica Acta* **2007**, *52*, 5512–5516.

[52] S. Zhang, Ö. Metin, D. Su, S. Sun, *Angewandte Chemie International Edition* **2013**, *52*, 3681–3684.

[53] I. Hussain, S. Graham, Z. Wang, B. Tan, D. C. Sherrington, S. P. Rannard, A. I. Cooper, M. Brust, *Journal of the American Chemical Society* **2005**, *127*, 16398–16399.

[54] A. Boddien, B. Loges, H. Junge, M. Beller, *ChemSusChem* **2008**, *1*, 751–8.

[55] B. Loges, A. Boddien, H. Junge, M. Beller, *Angewandte Chemie International Edition* **2008**, *47*, 3962–3965.

[56] C. Fellay, P. J. Dyson, G. Laurenczy, *Angewandte Chemie International Edition* **2008**, *47*, 3966–3968.

Chapter 5

Support Modification

Chapter 5 Support Modification 135

5.1 Background 136

5.2 Objectives 138

5.3 Experimental details 139

5.4 Results and discussion 140

5.4.1 Silica functionalisation 140

5.4.2 Silica supported palladium 145

5.4.3 Alumina functionalisation 153

5.4.4 Alumina supported palladium 159

5.5 Conclusion 166

5.6 References 167

5.1 Background

As seen in chapter 4, the adsorption of functional groups onto the surface of Pd nanoparticles can drastically affect the electronic and geometric properties of the particles, with corresponding changes in the activity and selectivity for formic acid decomposition observed. Addition of poly(allylamine) –a polymer containing primary amine pendent groups– to a supported Pd/C catalyst resulted in a substantial increase in activity through electronic donation, but did not provide the geometric modification observed with polymer stabilised colloidal particles. After washing the polymer modified Pd/C the promotional effects were reduced, indicating some of the polymer chains were washed away as reported by Hutchings *et al.* for poly(vinyl alcohol).[1]

Thus the modification of metal nanoparticles through the adsorption of organic groups shows significant potential for altering catalytic properties, but the use of polymers to perform this function has displayed some issues such as severe blocking of active sites and the polymer being washed from the metal, etc. An alternate method for introducing organic functional groups to supported catalysts has been through the functionalisation of the support surface.[2–4] An example of this is the refluxing of carbon based electro-catalyst supports in acid, which is widely used to produce oxygen containing species on the surface that increase conductivity and interactions between metal nanoparticles and support.[5] However, this method does not give a high degree of control over the groups produced on the surface and is limited to producing functional groups containing carbon and oxygen derivatives.

The introduction of a wide variety of functional groups to the surface of catalyst supports has been demonstrated using diazonium salts (that couple directly with the carbon surface) or through derivatising surface bound carboxylic acid groups produced from acid treatment.[3,4,6–

[8] The subsequent synthesis of supported metal nanoparticles using these functionalised materials as the support has shown significant alterations in the physical and chemical properties of the particles. Lee and co-workers attached different sulphur containing functional groups to the surface of carbon nanotubes and found the particle size, oxidation state, and activity for the Sonogashira coupling reaction of supported Pd nanoparticles corresponded with the functional group attached to the support.[4] The longer functional groups, containing more sulphur, increased the abundance of oxidised Pd which resulted in lower coupling activities. Tsang *et al.* also investigated the effects of chemical modification of carbon materials on the electro-oxidation of formic acid by supported Pd nanoparticles.[3] The activity of the supported particles is found to correlate with the electron donating ability of the functional groups, as such the activity was found to double from -Cl to –OH (or $–O^-$). A less significant increase in activity was observed for functionalised Vulcan carbon than for carbon nanotubes, attributed to a lower degree of functionalisation caused by the low surface area and less well defined carbon surface. As a result of the limited functionalisation of carbons typically used as heterogeneous catalyst supports, most studies of carbon based surface functionalised catalysts uses nanotubes or graphene.[9,10]

The introduction of high quantities of organic groups to the surface of more cheaply available catalyst supports is widely reported for metal oxides.[11–13] Typically, this is achieved through the coupling of silane reagents to hydroxyl species present on the surface of metal oxides.[12,14] Silanes are commercially available with many different functional groups, and this technique has been used to functionalise a large number of materials and surfaces.[15,16] Due to the widespread use of amine functionalised high surface area silica as carbon dioxide capture materials, a large number of studies have reported methods to maximise amine coverage whilst maintaining high surface areas.[17] The use of these surface bound functional

groups has recently been reported to heterogenise Ru and Pd based homogeneous formic acid decomposition catalysts.[13] Silanes with amine, thiol, or diphenylphosphine groups were attached to a high surface area silica support, which acted as ligands attaching the metal salt – that was subsequently added– to the support. The activity of these catalysts was highly dependent on both metal and functional group/ligands on the support surface but required high temperatures (85°C) and sodium formate or other additives to achieve high activities.

However, the use of support bound organic groups has also recently been reported to modify heterogeneous catalysts for formic acid decomposition. Xu *et al.* used the formation of a silica shell around small Au particles to produce a yolk-shell structure with their particles encapsulated in a "nanoreactor".[2] Using amine functionalised silanes to produce this shell, the activity of the catalyst was dramatically increased with the formic acid decomposition rate three times faster than for the Au encapsulated in a silica shell with no amine. This agrees with previous reports that amines are required to achieve high formic acid decomposition activity with Au, but also indicates the potential of groups tethered to the support surface to modify heterogeneous catalysts.[18] Whilst these results show the potential of surface bound modifiers to enhance formic acid decomposition, high temperatures are still required. Additionally, it is found that total encapsulation of the Au particles is crucial, as Au on an amine modified commercial silica shows almost no activity for formic acid decomposition.

5.2 Objectives

The electronic and geometric influence of organic molecules on metal nanoparticles is widely reported, however their binding on the nanoparticle surface is often reversible, limiting their potential use in many heterogeneous catalytic systems. In this chapter the ability of functional

groups bound to the catalyst support to modify supported Pd nanoparticles will be examined, along with the effects these electronic and geometric alterations have on the activity and selectivity for formic acid decomposition. The aim is to produce an organic modified Pd catalyst that is a highly active and selective formic acid dehydrogenation catalyst, with highly stable, permanently attached functional groups. Thus improving on the highly active catalysts observed in chapter 4, by overcoming limitations of the polymer modified system including the polymer washing off.

5.3 Experimental details

Extensive experimental details of the synthesis procedures, characterisation methods and catalysis testing are given in chapter 3; a brief summary of catalyst synthesis is given here. Metal oxides were functionalised using a method similar to Harlick and Sayari, before functionalising the metal oxide was dried at 150°C under vacuum for 24 hours. Dry metal oxide was dispersed in dry toluene and heated to 85°C under nitrogen, if required 0.3 mL g^{-1} of water was added and allowed to mix for one hour. Silane was added and the reaction left for 16 hours, before filtering and washing with hot toluene. Synthesis of supported Pd used a modified precipitation-deposition method, similar to that of Cho *et al.* but with a solution phase hydrogen reduction. $Pd(NO_3)_2$ and support were mixed in water and stirred for 1 hour, before the pH was increased using NaOH. After stirring for 30 min, hydrogen was bubbled through the solution, and the reaction was heated to 85°C for 1 hour. After cooling the catalyst was removed by filtration, washed extensively with water and dried at 80°C in air.

5.4 Results and discussion

5.4.1 Silica functionalisation

From the studies on polymers in chapter 4, amines were found to be the most electronically donating functional group of those tested. Additionally, amine groups displayed a preference for adsorption on low coordinate sites when Pd particles were synthesised in their presence, which resulted in the blocking the un-favoured dehydration of formic acid. As such, an amine containing functional group was selected to be grafted onto the surface of the support. Due to the extensive studies of silica surface functionalisation using silane coupling agents and the stability of the attached functional groups, this method was selected to produce amine functionalised surfaces. The silane used was (3-aminopropyl)trimethoxysilane (APTMS), which contains a primary amine attached to the coupling trimethoxysilane via a propyl chain. A commercial silica (Davisil® 643) with a surface area of 300 m^2 g^{-1} was used as the support. The extensive studies of the functionalisation of silica with amine derivitised silanes has resulted in a wide range of techniques using a variety of different solvents, temperatures, reaction times, etc., with the degree of functionalisation varying dramatically.

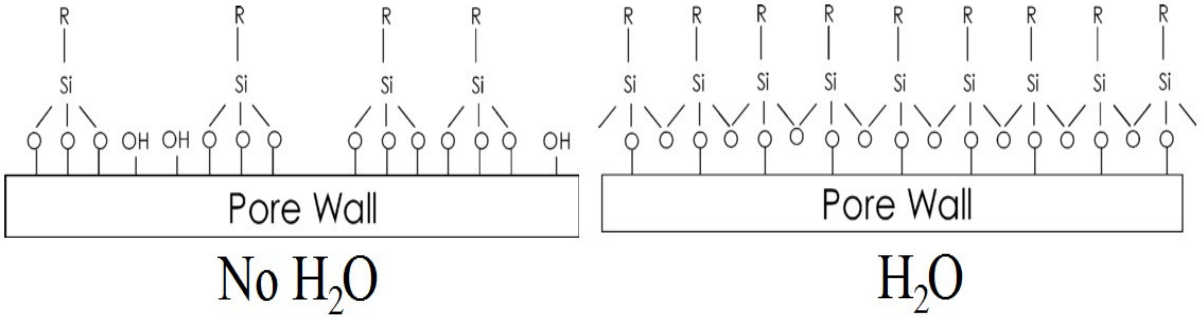


Figure 5.1– Schematic of silane functionalised surface with and without water.
Modified from reference[17]

The ability of the methoxy groups of the trimethoxysilane to react with water, producing methanol and Si-OH, means that functionalisation is traditionally performed under water-free

conditions. But as displayed in figure 5.1 the addition of small amounts of water can increase the degree of functionalisation, as it facilitates the formation of cross-linking bonds between the individual silane molecules on the surface, resulting in a much denser coverage of functional groups. Harlick and Sayari investigated the dependence of the functionalisation on content of water added and found the optimum amount of water, under their conditions, was 0.3 mL $g(SiO_2)^{-1}$.[17] Higher concentrations of water meant that the methoxy groups on the silane would react directly with water, producing Si-OH groups that would not couple to the surface. Lower concentrations resulted in the amount of surface OH species limiting the amount of silane that could attach. By drying silica under vacuum, and using dry solvents, the quantity of water could be highly controlled and optimised to achieve maximum silane coverage.

Following the method of Harlick and Sayari, functionalised silica materials were produced and the amount of functionalisation was varied through the controlled addition of water. Figure 5.2 shows the TGA of silane functionalised silica with and without the addition of water. For unmodified silica the weight loss observed up to ~150°C is attributed to the loss of water adsorbed on the surface and trapped in pores. From 200-900°C further weight loss is observed, which is attributed to the loss of surface hydroxyl species and organic impurities. For both functionalised supports a similar degree of weight change is observed as with the un-modified silica up to ~300°C, again attributed to removal of water or other residual solvent. Above 300°C, significant additional weight loss is observed for the functionalised supports compared to unmodified silica. Assuming the SiO_3 section is not lost from the surface after modification, the additional weight change above 300°C is attributed to loss of the propylamine from the surface.

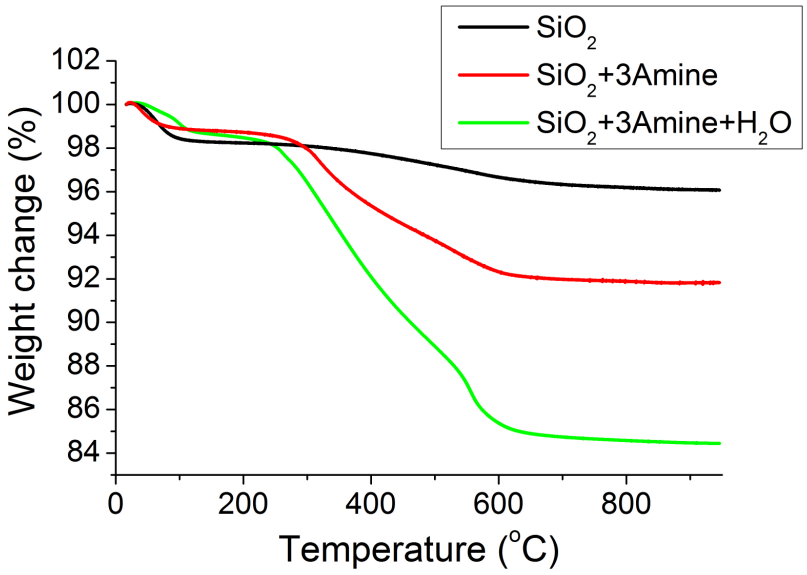


Figure 5.2– TGA of SiO_2 and (3-aminopropyl)trimethoxysilane functionalised SiO_2 with and without the addition of water

For analysis the TGA profile was divided into two regions: the first between 0-200°C is independent of the degree of functionalisation, with the second region (200-900°C) dependent on changes in the number of functional groups attached to the silica. Table 1 displays the weight changes of the supports over the two regions. Figure 5.2 and table 1 both indicate that functionalisation had taken place and in agreement with the literature reports, the degree of functionalisation is dramatically increased with addition of water.

Table 1– Summary of weight loss and resulting functional group content of silica and functionalised silicas

	Weight loss (%)			Amine Content	
	0-200°C	200-900°C	FG loss[a]	mmol(FG) g^{-1} [b]	µmol(FG) m^{-2} [c]
SiO_2	1.77	2.14	N/A	N/A	N/A
+3Amine	1.28	6.90	4.76	0.821	2.737
+3Amine+H_2O	1.53	14.00	11.86	2.045	6.817

[a]% weight loss calculated from the difference in the weight loss (200-900°C) between functionalised and un-functionalised silica; [b]Moles of propylamine M_w=58; [c]Calculated using silica surface area of 300 m^2 g^{-1}.

The number of functional groups (moles per gram) attached to the silica surface are similar to the values reported in the literature, with the addition of water resulting in approximately a 2.5 times increase in the number of amine groups on the support. Harlick and Sayari reported 2.04 mmol g^{-1} on a much higher area support (950 m^2 g^{-1}) and Tsang *et al.* achieved 1.7 mmol g^{-1} of propylamine on a 200 m^2 g^{-1} silica support, both used a functionalisation method involving the addition of water and are in good agreement with our level of functionalisation.[12,17] Interestingly, the coverage of functional groups (moles per m^2) is much higher than that observed by Harlick and Sayari (2.15 µmol m^{-2}), whose method was the basis of our method, but much closer to the reports of Tsang *et al.* (8.5 µmol m^{-2}). This is attributed to the degree of functionalisation being dependent on the surface area of the support, likely due to changes in the ability of the silane to access the pores of the support.

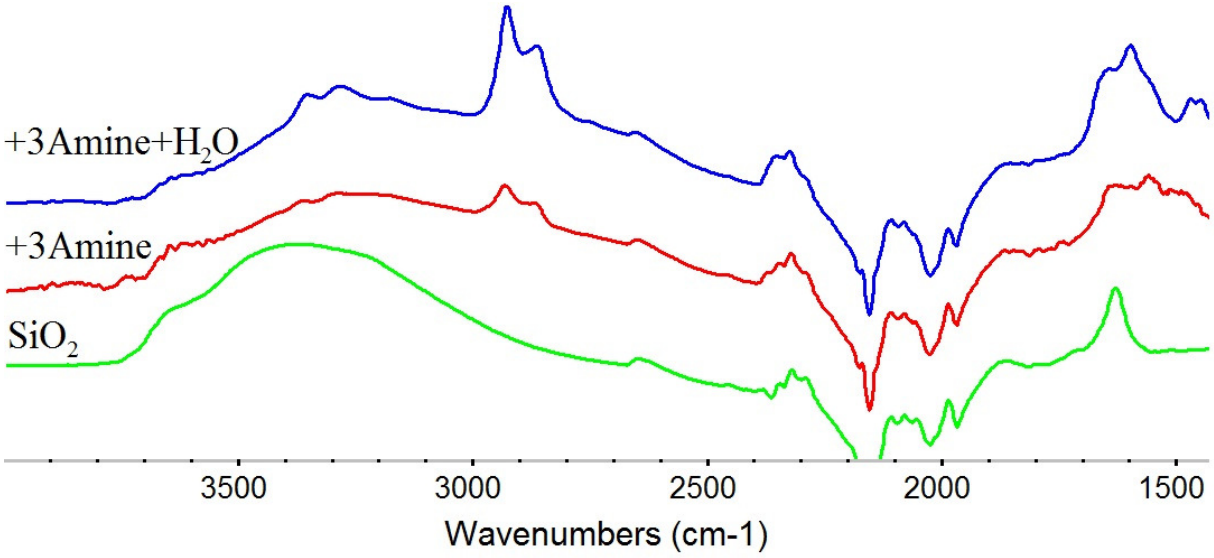


Figure 5.3– FTIR of SiO_2 and functionalised SiO_2

To further understand the nature of functional groups on the surface of the support they were examined using FTIR (figure 5.3). A number of peaks are observed in all the spectra due to features of the silica surface; the broad peak around 3400 cm^{-1} is attributed to the OH stretch of surface hydroxyl groups and those of adsorbed water molecules, the peak at 3750 cm^{-1} is assigned to isolated surface hydroxyl species and the peak at 1630 cm^{-1} is assigned to deformation vibrations of adsorbed water.[19,20] For the modified supports additional peaks are clearly present, the peaks at 2900 cm^{-1} are assigned to C-H vibrations with the peaks at 3300 cm^{-1} indicating N-H bonds.[20,21] These peaks indicate the presence of the amine containing functional groups on the surface and show that the aminopropyl group has not decomposed under the functionalisation or drying conditions. The increase in intensity for the C-H and N-H peaks for SiO_2+3Amine+H_2O confirms that the increased weight loss, observed by TGA, is due to an increase in surface functionalisation. Additionally, the decreased intensity of the broad hydroxyl region with increasing functionalisation demonstrates the conversion of surface Si-OH to Si-O-Si bonds through attachment to the silane molecules.

5.4.2 Silica supported palladium

A number of methods were investigated for the synthesis of supported palladium particles similar to those typically used in the literature.[22–25] The deposition of preformed nanoparticles onto the supports, although ideal as all the particles would have the same initial physical properties, was not possible as the stabiliser could not be removed without potentially damaging the surface organic groups.[25,26] Additionally, one of the major benefits of the amine groups was their preference to selectively block low coordinate sites, which was only observed when the particles were synthesised in the presence of the amine. Therefore a modified precipitation-deposition method was used, similar to that of Cho *et al.* but with a solution phase hydrogen reduction.[24] First, Pd was precipitated onto the support in the form of $Pd(OH)_2$ - by raising the pH to 11 with NaOH - that was then, with the support still dispersed in solution, reduced by bubbling hydrogen. Room temperature hydrogen has been shown to reduce $Pd(OH)_2$ on carbon to metallic Pd (details in chapter 6), but as the stabilisation of metal ions by transition metal surfaces is widely reported, the temperature of reduction was increased (85°C) to promote Pd reduction.[27,28]

Additionally, due to the silica support having a lower surface area (300 $m^2 g^{-1}$) than typical carbon supports, similar to that of the support for 87L used in chapter 4, the metal loading of the catalysts was reduced to 5%. The lower loadings will also increase the ratio of surface functional groups to Pd, which should enhance the influence the groups can have on the Pd surface. The silica and modified silica catalysts were characterised by XRD, a typical spectrum for 5% Pd/SiO_2 is shown in figure 5.4.

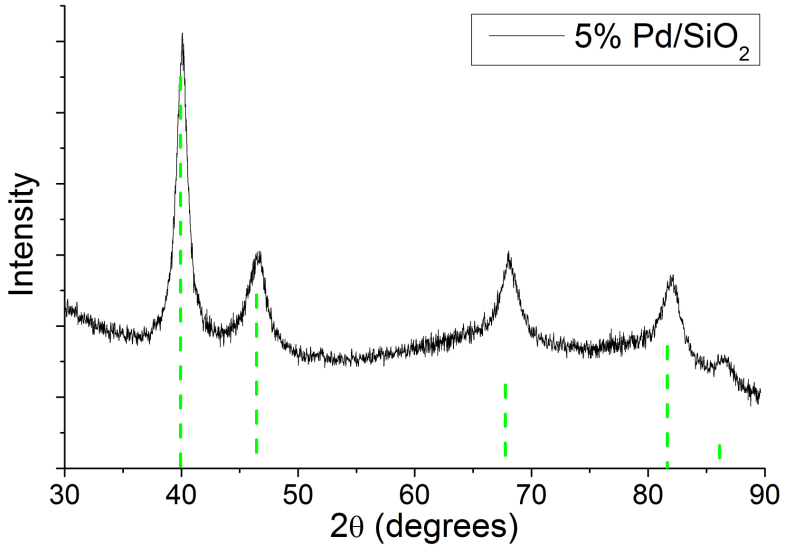


Figure 5.4– XRD of 5% Pd on silica and position of Pd metal peaks from ICSD

The strong agreement between the observed peaks and those reported for Pd metal in the Inorganic Crystal Structure Database (REF 064920), along with the lack of any other species, indicate that $Pd(OH)_2$ has been reduced. For all three supported Pd catalysts, very similar diffraction patterns were obtained with only the peak broadness altered. From the (220) peak the size was calculated as 5.8 nm, 5.4 nm, and 5.2 nm for 5% Pd supported on silica, silica+3Amine, and silica+3Amine+H_2O, respectively. The decreasing size of Pd indicates that the amine functional groups are aiding the dispersion of the Pd, which is expected from the common use of amine containing molecules as nanoparticle stabilisers.[29] From TEM of the silica and silica+3Amine+H_2O supported Pd catalysts (figure 5.5 and 5.6) the average size was found to be 4.8 nm and 3.6 nm respectively, this discrepancy between XRD and TEM is expected due to the detection limit of XRD, preventing it from accounting for very small particles.

The size distribution histograms clearly demonstrate that the size of the Pd particles on the amine stabilised support is significantly reduced with respect to the Pd on the unmodified silica, indicating the amine groups are stabilising the Pd particles and restricting their growth.

Also apparent is the broader size distribution of the Pd/SiO_2+3Amine+H_2O catalyst, which may indicate that the amine is not evenly coated over the silica surface resulting in some highly stabilised (small) particles and some weakly stabilised (large) particles. The TEM images also display that the Pd particles on silica are more aggregated than those on the functionalised support, again indicating the amine groups play a role in stabilising the particles and maintaining their dispersion.

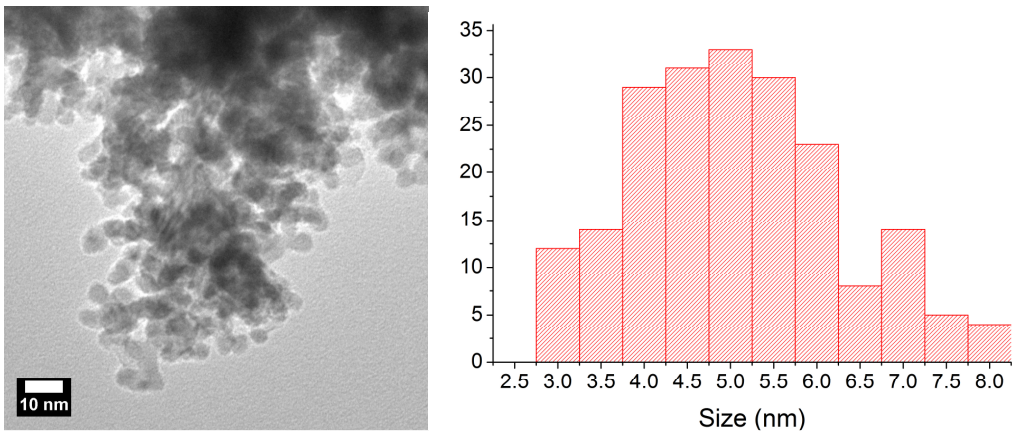


Figure 5.5– TEM micrograph of 5% Pd/SiO_2 and size distribution histogram

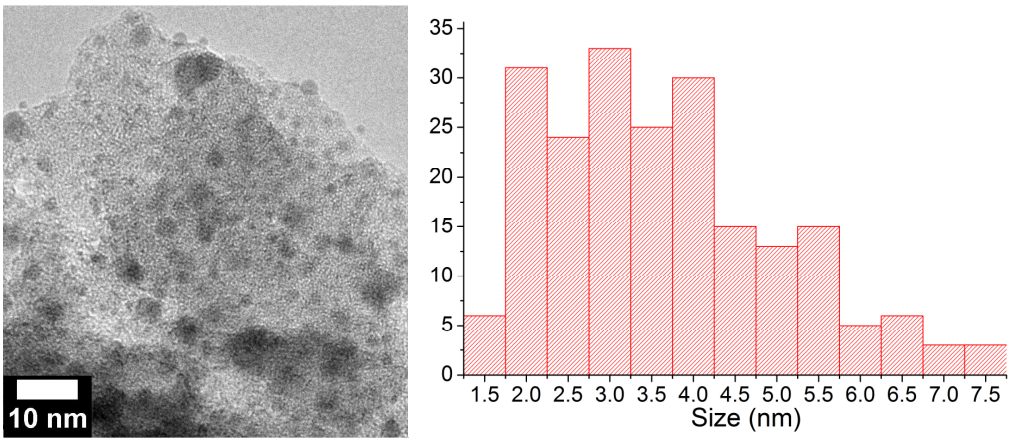


Figure 5.6– TEM micrograph of 5% Pd/SiO_2+3Amine+H_2O and size distribution histogram

The metal surface area of these catalysts was determined by CO chemisorption, providing a measure of metal dispersion and the degree of metal surface blocked through interaction with amine groups. The metal surface areas were dramatically lower than was expected, even for

Pd on the unmodified silica, with values of 25.4 m^2 $g(Pd)^{-1}$, 15.3 m^2 $g(Pd)^{-1}$, and 14.6 m^2 $g(Pd)^{-1}$ for 5% Pd supported on silica, silica+3Amine and silica+3Amine+H_2O, giving theoretical particle sizes of 16.4 nm 27.2 nm and 28.5 nm, respectively. For 5.8-5.2 nm Pd particles the metal surface area is expected to be approximately 70-80 m^2 g^{-1}. Clearly there is a large discrepancy between the measured metal surface area and the particle size from XRD and TEM, but it is important to note that the surface area measurement only detects un-blocked metallic Pd surface. As such, the trend of decreasing metal surface area with more amine is expected as the amine blocks the surface, but this cannot account for the large discrepancies between particle size and surface area, which are in stark contrast to the differences in size and dispersion observed by TEM.

Whereas the aggregated nature of the Pd/SiO_2 may explain the difference between Pd surface area and size results, the differences in the well dispersed Pd on amine modified supports clearly cannot be explained by this argument. Whilst Pd^{2+} is clearly being reduced and forming particles, as detected by XRD and TEM, under the conditions of measuring metal surface area (after a pre-reduction at 40°C) the surface Pd is not necessarily metallic. In the previous chapter we found that the PdO species in type 87L Pd/C will reduce under hydrogen at room temperature; but it has been reported that, on metal oxides, a higher temperature can be required for total reduction, particularly for small Pd particles.[27,28] Therefore it is expected that the oxides formed on the surface of small Pd particles upon exposure to air or during catalyst drying are not being reduced prior to surface area measurement. The differences in the metal surface area expected from the XRD and TEM particle size and the metal surface area measured by CO chemisorption, is thus expected to be due to the formation of Pd particles with oxide surfaces. To explore this proposal a sample of 5% Pd on silica+3Amine+H_2O was pre-treated under hydrogen at 350°C (just below the amine

decomposition temperature) before measuring the CO chemisorption. The resulting metal surface area was greatly increased compared to the sample pre-treated at 40°C, confirming our belief that oxide formation was preventing CO adsorption. The higher metal surface area of 163.8 m^2 $g(Pd)^{-1}$ indicates a particle size of 2.5 nm, slightly lower than the 3.6 nm found by TEM, which is reasonable as the measurement of very small particles < 2 nm is often difficult due to their low contrast in bright field TEM.

The supported 5% Pd catalysts were then tested for formic acid decomposition, but were not reduced at a high temperature to prevent any decomposition of the functional groups. Thus, the Pd surface area of the tested catalysts is expected to be that measured by CO chemisorption, and as a result the overall activity of the catalysts ($g(Pd)^{-1}$) will be lower than other catalysts as a significant proportion of the metal is inactive due to being coated in an inert oxide layer. However, the activities of the samples ($g(Pd)^{-1}$) displayed in figure 5.7 are all comparable due to the similar metal surface areas and the TOFs allow a precise comparison with other systems.

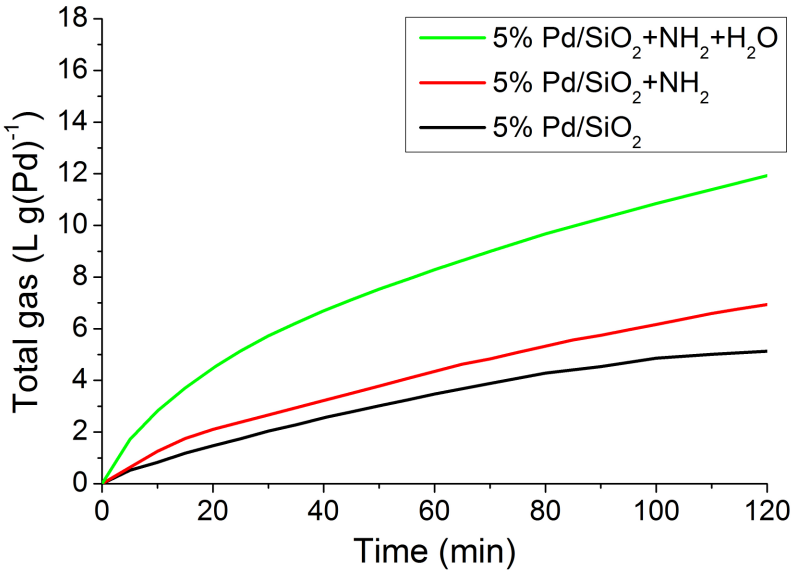


Figure 5.7– Activity plot of 5% Pd on silica supports, 4.25 mg of Pd stirred in 10.575 mL of 1.4 M formic acid at 25°C

Figure 5.7 displays that all catalysts result in a similar profile, with an initially high rate that decreases over time indicative of deactivation due to the formation of CO from formic acid dehydration. The clear deactivation of the amine containing catalysts indicates that the amine groups have not totally blocked the low coordinate sites; otherwise a constant activity would be expected. Although both amine containing catalysts have lower Pd surface areas than the unmodified catalyst they both show a greater activity, with Pd/SiO_2+3Amine+H_2O resulting in over twice the volume of gas produced over two hours. The large increase in initial rate for Pd/SiO_2+3Amine+H_2O is clearly evident, indicating that Pd is substantially more electron rich than in Pd/SiO_2 and overcoming the 40% loss in metal surface area. The TOF of Pd/SiO_2, Pd/SiO_2+3Amine and Pd/SiO_2+3Amine+H_2O (from the full two hours), are 107, 240 and 432 h^{-1}, respectively. Thus, introduction of the amine has resulted in more than a two fold increase in TOF, with the maximum amine content resulting in a four times increase in activity. Comparing these results with the results of the previous chapter, it is apparent that the activity ($g(Pd)^{-1}$) is dramatically lower, with the activity of the best modified silica being less than half that of unmodified type 87L. But the TOF of Pd/SiO_2 (107 h^{-1}) is comparable with that of type 87L (169 h^{-1}) over two hours and the polymer promotion results in a similar degree of increase in activity with type 87L+PAAmine 1:5 showing a 3.6 times higher TOF than type 87L.

Whilst the role of the amine appears to be similar to that of the polymer modification, the lack of geometric blockage effects and changing degree of electronic donation required further examination. As was found highly useful in the previous chapter, FTIR was used to examine a colloidal Pd-PVP catalyst with chemisorbed CO. To model the effects of the propylamine groups in the modified silica supported Pd catalysts, small quantities of molecular amines were added to the Pd-PVP particles before exposing them to CO. Thus, any geometric or

electronic modification of the surface caused by the amines could be observed by the changes in the peak positions and ratios.

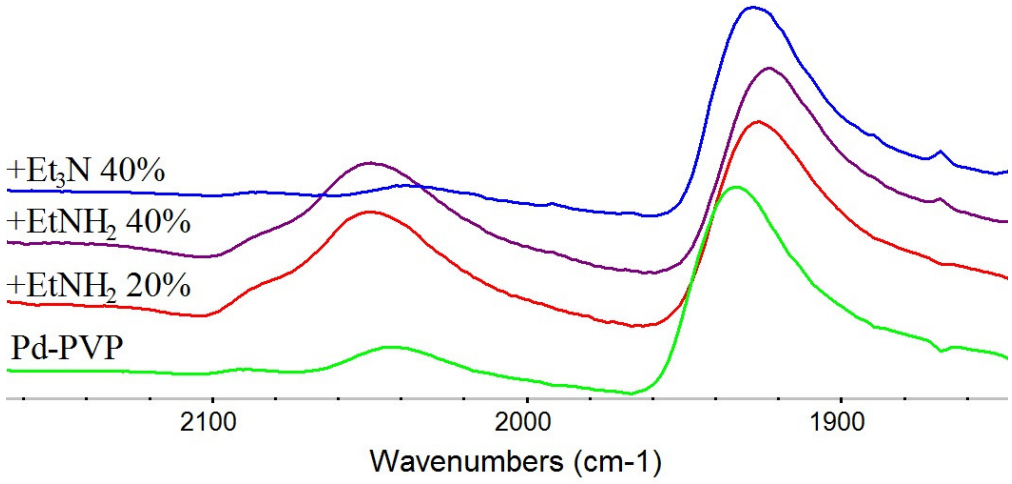


Figure 5.8– FTIR of CO adsorbed on Pd-PVP with ethylamine or triethylamine. Intensity normalised by bridging CO peak

Figure 5.8 displays the FTIR spectra of CO adsorbed on amine modified Pd-PVP particles, the amine contents are displayed as a percentage of the total Pd in the sample. The Pd-PVP particles were synthesised as in chapter 4, with a 1:10 ratio of PVP and using ethylene glycol reduction, resulting in 3.2 nm particles. Assuming a cubo-octahedral shape (lowest surface energy) and using the calculations of van Hardeveld and Hartog the number of surface atoms was calculated (calculation details are provided in chapter 6).[30,31] Initially a primary amine (ethylamine) was used to represent the propylamine attached to the support surface; the amount of amine was selected to give approximately half and total coverage of the particle surface, 20% and 40% of the total Pd atoms respectively. From figure 5.8, increasing the amount of ethylamine clearly increases the electronic modification of the surface, with the bridging CO peak shifting to lower wavenumbers indicating increased back donation from Pd to CO. On the other hand, little shift is seen in the linear CO peak due to the low coordinate sites being decoupled from the bulk Pd atoms.[32]

Surprisingly the geometric modification is not what was expected from the reports of Ryu *et al.*, in both cases the increased intensity of the linear CO peak relative to the bridging peak indicates that ethylamine is preferentially adsorbing onto terrace sites.[33] It is also apparent that the amine is not fully bound to the surface or is partially displaced by CO, because CO peaks are observed when the surface should be fully covered with ethylamine. Whilst ethylamine does not show the same geometric effects that we observed for amine containing polymers (chapter 4), the literature proposes a reason. A wide range of molecules have been reported to form self-assembled monolayers (SAM) on the surface of nanoparticles and single crystals; in these layers the head groups bind to the surface with the tail groups all aligned away from the surface, resulting in a tightly packed single layer of the molecular species.[34] From these results, it is reasonable to expect that upon ethylamine adsorption via N, a similar layer may form from the ethyl tail groups, thus binding on terrace sites would be favoured to maximise interactions between the chains, which would not be possible with the polymers discussed in chapter 4.

To prevent the formation of SAM's a sterically hindered tertiary amine was used to modify the surface; this resulted in the expected site selective blocking on the metal surface. Unfortunately, the selective binding of triethylamine does not clarify whether all amines prefer to bind on low coordinate sites (if they did not form SAMs) or if the site selectivity is purely due to the steric hindrance for the tertiary nitrogen atom, favouring the least hindered low coordinate sites. The steric hindrance of the nitrogen atom also appears to reduce the amount of amine molecules able to bind to the surface of the Pd particles. The electronic donation would be expected to increase with more electron donating groups on the nitrogen, 1° < 2° < 3°, but the shift in the bridging CO peak for 40% coverage by triethylamine is

approximately equivalent to only 20% coverage by ethylamine. This indicates that much less of the tertiary amine can bind than the primary amine in ethylamine.

Thus, from the FTIR results it appears that by using tertiary amines on the surface of the support, selective blockage of low coordinate sites will be favoured but binding to the particle is also expected to be reduced. Unfortunately, the intrinsic properties of silica to stabilise oxide formation on small Pd nanoparticles make it unsuitable for further studies of the effects of support modification and another material should be investigated.[27,28]

5.4.3 Alumina functionalisation

The addition of amine functional groups to the surface of the support has clearly had substantial promotional effects on the activity of Pd for formic acid decomposition, but even though this results in a catalyst with high TOF the activity ($g(Pd)^{-1}$) is still low, requiring a high quantity of metal to achieve substantial levels of gas production. As much of the expensive metal content is wasted as oxide and the high temperatures required to fully reduce the PdO on silica may damage the functional groups, silica is not an ideal support for use in this system.[28] Thus, another support material was required; in the literature almost every Pd based catalyst for the solution phase decomposition of formic acid, uses a carbon support.[25,35,36] But as the functionalisation of the surface by silane requires surface hydroxyl species, carbon would likely result in very low levels of surface functionalisation, so is not an ideal material to study. An ideal catalyst support would have a high density of hydroxyl species on the surface and a reasonably high surface area to facilitate the use of higher metal loadings.

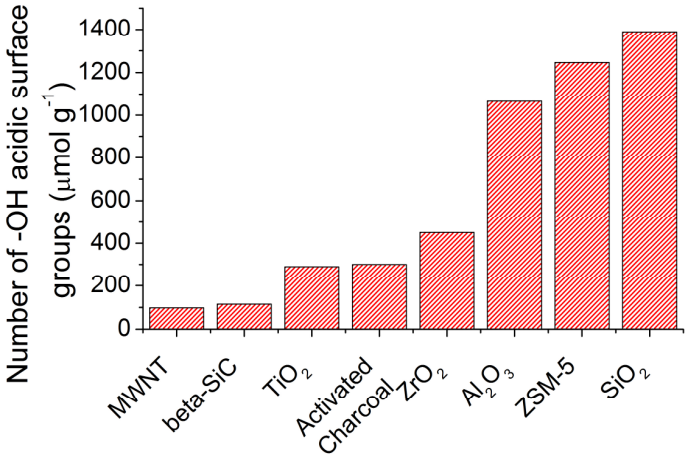


Figure 5.9– Quantity of acidic -OH groups of the surface. Modified from reference[14]

The results of Keller *et al.* (figure 5.9) display the number of acidic hydroxyl species on the surface of a range of materials.[14] The number of hydroxyl groups on a known mass of sample was determined using mass spectrometry to monitor H/D exchange between the surface and D_2O vapour. From their results, γ-alumina was found to have quite a high number of hydroxyl groups, only 25% less than silica and as alumina has been reported to be functionalised using silane coupling, it was an ideal candidate for use as another support to modify.[16] Additionally Chang *et al.* report that, after calcination at 400°C to decompose the Pd salt, Pd is fully reduced by 65°C when supported on Al_2O_3, which agrees with the results of Tsang *et al.* who found reduction at similar temperature.[27,28]

As such γ-Al_2O_3 was selected as another support to modify with amine groups, to provide further insight into the role of the support and clarify the potential ability of surface functionalised supports to produce highly active and selective formic acid decomposition catalysts. From the results in section 5.4.2 it is clear the highest coverage of amine groups is desirable, and as the ability of silane to couple to the surface is determined by the presence of hydroxyl groups, increasing their number should facilitate further coupling. A number of

methods have been reported to increase the surface hydroxyl group concentration of alumina materials, typically involving stirring in water or a basic solution.[16] As such, a number of these methods were performed on γ-Al_2O_3, with the change in the number of hydroxyl species analysed by TGA (figure 5.10).

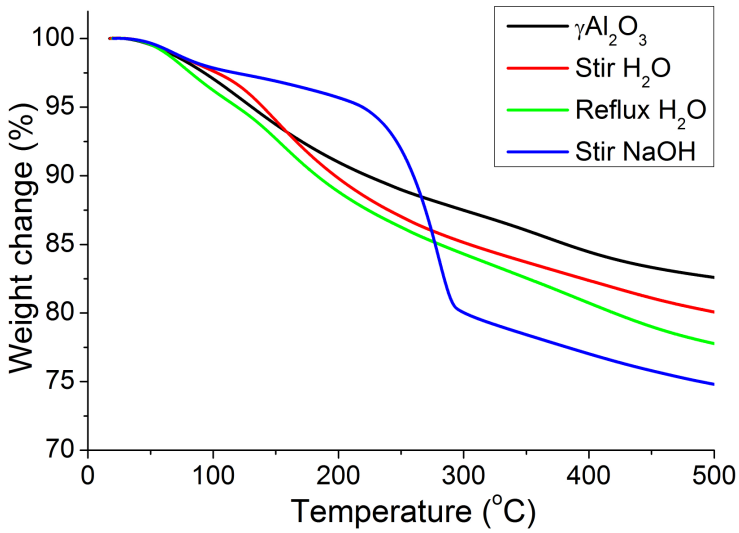


Figure 5.10– TGA of γ-alumina and γ-alumina treated in water or NaOH

Clearly in the case of γ-Al_2O_3 the weight loss is less well defined than with SiO_2, and a continual weight loss is observed between 50-500°C and above. This is assigned to the wide range of different water and hydroxyl surface sites on γ-Al_2O_3 decomposing at various temperatures.[37,38] The only sample that shows a significantly different profile is the γ-Al_2O_3 stirred in a pH 11 sodium hydroxide solution, which displays very little weight loss until ~250°C when there is a rapid change; this is reported to be due to the decomposition of $Al(OH)_4$. Whilst it would appear that this high number of hydroxyl groups would be ideal, it is found that the volume change upon forming $Al(OH)_4$ results in blockage of the support's pores, dramatically reducing surface area. Refluxing γ-Al_2O_3 in water does not result in a significant increase in the number of hydroxyl species compared to room temperature stirring in water, and as such, only dry γ-Al_2O_3 and γ-Al_2O_3 stirred in water, designated "γ-Al_2O_3(+H_2O)", were used for silane modification

Table 2 displays the weight changes over two regions for γ-Al_2O_3 and a range of modified γ-Al_2O_3 samples. Due to the high amount of weight loss observed for γ-Al_2O_3 (from water loss) the temperature range for solvent effects was increased to 300°C, which was still below the silane decomposition temperature. In addition to the pre-treatment of γ-Al_2O_3, the addition of water to the dry metal oxide dispersed in dry toluene was also examined, again using 0.3 mL g(γ-Al_2O_3)$^{-1}$ that was found optimal for increasing the functional groups on silica.[17]

Table 2– Summary of weight loss and resulting functional group content of γ-Al_2O_3 and the functionalised γ-Al_2O_3 samples

	Weight loss (%)			Group Content	
	0-300°C	300-950°C	FG loss[a]	mmol(N) g^{-1} [b]	µmol(N) m^{2} [d]
γ-Al_2O_3	12.87	15.93	N/A	N/A	N/A
+3Amine	8.06	18.80	2.87	0.495	2.75
+3Amine+H_2O	11.83	21.60	5.67	0.978	5.43
(+H_2O)+3Amine	12.94	19.40	3.47	0.598	3.32
+NEt_2+H_2O	11.14	18.89	2.96	0.260[C]	1.44

[a]% weight loss calculated from the difference in the weight loss (200-900°C) between functionalised and un-functionalised γ-Al_2O_3; [b]Moles of propylamine M_w=58; [c]Moles of $C_7H_{16}N_1$ M_w=114; [d]Calculated using γ-Al_2O_3 surface area of 180 m^2g^{-1}.

The number of amine groups per gram of support is clearly lower than when the same methods were used to functionalise silica, but they result in similar densities of groups on the surface of the supports. This agrees with the literature that indicates surface area has an important role in determining the number of functional groups per gram of support.[17] The addition of a controlled amount of water to the dry reaction mixture again results in over

twice the functional groups attaching to the surface, expected to be through the same method reported for the functionalisation of silica (figure 5.1). The pre-treatment of γ-Al_2O_3 in water, which resulted in a small increase in hydroxyl or adsorbed water species on the surface, only demonstrates a small increase in functionalisation over the vacuum dried sample. Overall the addition of water to the dry reaction mixture again results in the highest degree of functionalisation of the surface; but even though the number of groups (mmol g^{-1}) is decreased for the lower surface area γ-Al_2O_3 (180 m^2 g^{-1}) compared to silica (300 m^2 g^{-1}), the density of functional groups on the surface is similar, which should result in a similar degree of modification to the Pd.

In addition to the functionalisation with APTMS (a primary amine), a tertiary amine was also attached to the surface using silane coupling. As we saw in figure 5.8 tertiary amines displayed a strong site selectivity by only blocking low coordinate sites, and as these sites are responsible for formic acid dehydration producing catalyst poisoning CO their selective blocking would be highly favourable.[25] As such [3-(diethylamino)propyl]trimethoxysilane (DEAPTMS), which consists of two ethyl groups on the nitrogen of the propyl amine group of APTMS, was used to functionalise the surface using the conditions found to be optimal for APTMS functionalisation. The results of TGA analysis clearly show that only a low degree of functionalisation is achieved, which is likely due to the increased steric hindrance caused by the two ethyl chains limiting available support surface area.

An alternate technique was also used to attach a large number of tertiary amine groups to the surface of the γ-Al_2O_3, it involved two steps with the first functionalising the surface and the second derivatising the attached functional group.[15] Initially the surface was functionalised with the epoxide containing molecule (3-glycidoxypropyl)trimethoxysilane (GLYPTMS),

through silane coupling in a similar way to the previous method except without the addition of any water. The epoxide ring is then reacted with an amine; the overall reaction is displayed in figure 5.11.

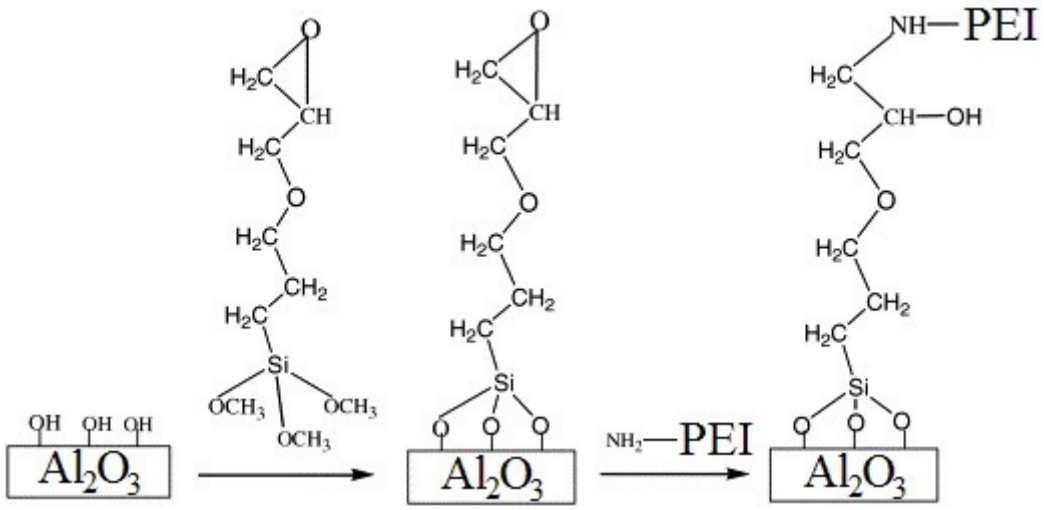


Figure 5.11– Mechanism of GLPTMS coupling to surface hydroxyl species and subsequent reaction with an amine group of PEI. Modified from reference[15]

From TGA analysis only a quite low degree of functionalisation by GLYPTMS is observed (0.198 mmol g^{-1}), which is again attributed to both the large functional group resulting in steric limiting effects and the fact that no water was added. Water was not added to ensure it could not react with the epoxide ring at the elevated temperature used for functionalisation. Due to the highly branched nature of PEI and its relatively high molecular weight (M_w= 35000), a large number of GLYPTMS linkers are not required to potentially attach large quantities of amines to the surface. After adding PEI the sample was extensively washed, thus ensuring only chemically bound PEI remains. TGA results indicate that 1.38 mmol(PEI monomer) g^{-1} and 7.67 µmol(monomer) m^{-2} of the polymer are strongly bound to the γ-Al_2O_3. Thus a range of supports with varying types and numbers of amine groups have been prepared to act as supports for Pd nanoparticle based formic acid decomposition catalysts.

5.4.4 Alumina supported palladium

5% Pd supported on the γ-Al_2O_3 samples were prepared using the same method as for the 5% Pd on silica samples, the only alteration was a reduction in the pH used to precipitate $Pd(NO_3)_2$ as $Pd(OH)_2$ from pH 11 to pH 8, because at pH 11 γ-Al_2O_3 was observed to form $Al(OH)_4$. From the literature, total reduction of Pd supported on γ-Al_2O_3 is expected around 70°C, so Pd should be totally reduced under the synthesis conditions with a hydrogen reduction at 85°C.[27,28]

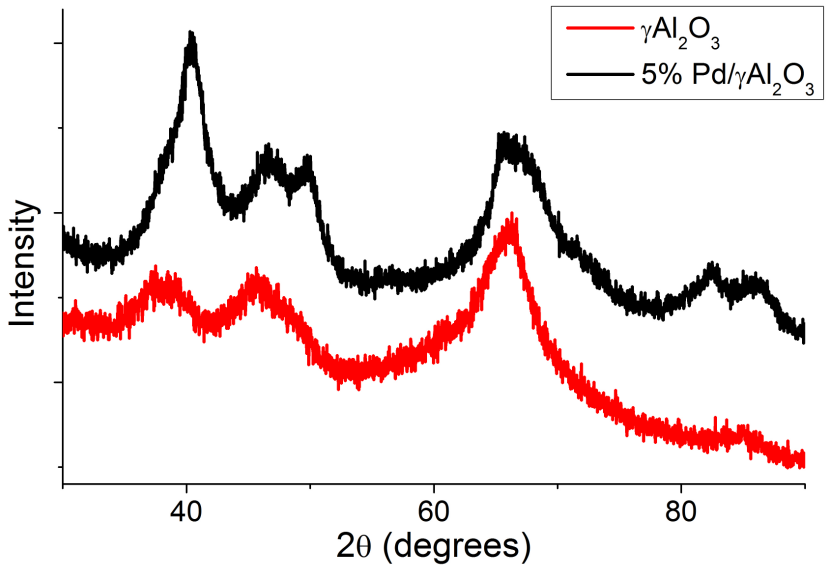


Figure 5.12– XRD pattern of γ-Al_2O_3 and 5% Pd/γ-Al_2O_3

After synthesis and drying, the 5% Pd on γ-Al_2O_3 and modified γ-Al_2O_3 samples were characterised. Whilst the overlap of the γ-Al_2O_3 peaks and metallic Pd peaks, apparent in figure 5.12, prevents the determination of Pd size by XRD it is clear from comparison with figure 5.4 of 5% Pd/SiO_2 and metallic Pd (ICSD 064920), that reduction of $Pd(OH)_2$ to Pd metal had indeed occurred. Thus, TEM was relied upon to give particle size and dispersion details (figures 5.13 and 5.14) and was compared with the metal surface area from chemisorption of CO.

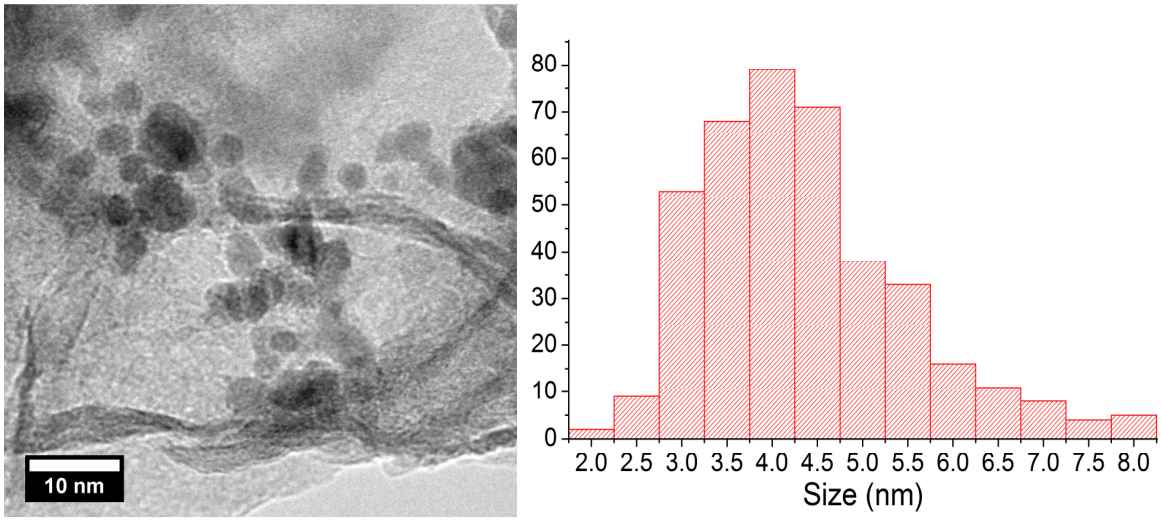


Figure 5.13– TEM micrograph and size distribution histogram of 5% Pd/γ-Al_2O_3

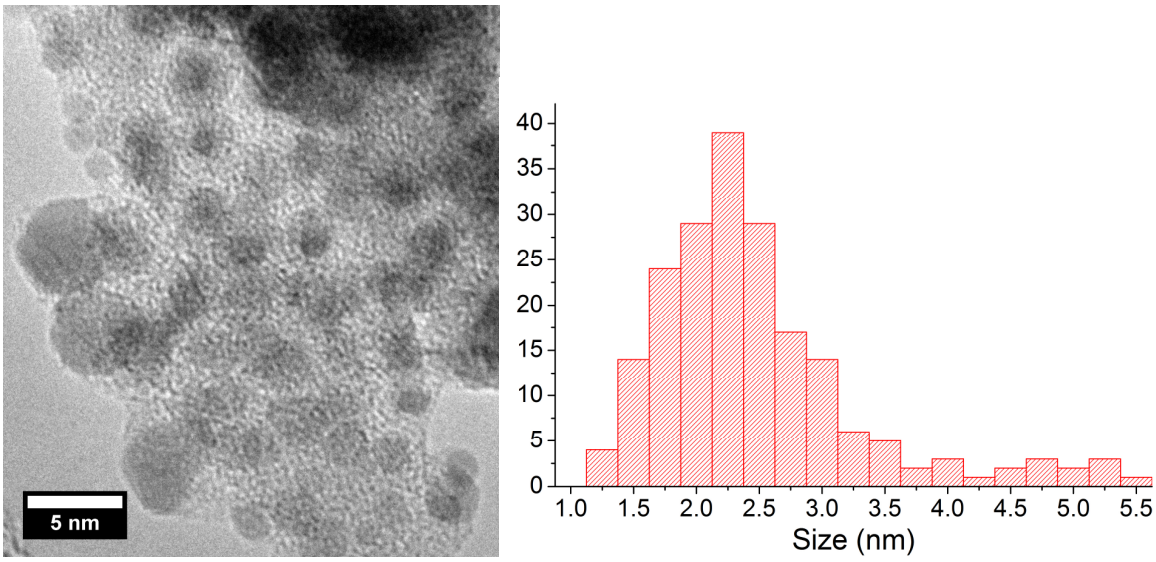


Figure 5.14– TEM micrograph and size distribution histogram of 5% Pd/γ-Al_2O_3+3Amine+H_2O

From TEM it can be seen that, similar to the case of the silica supported particles, the highly functionalised amine support results in much smaller particles, but in the case of 5% Pd/γ-Al_2O_3+3Amine+H_2O the size distribution is narrower indicating a more even coverage of the functional groups on the surface. Also in both cases the Pd particles on γ-Al_2O_3 supports are better dispersed than the silica supported samples. Comparing the sizes of the catalysts with the metal surface area measured by CO chemisorption proved highly informative for

understanding the low activities of Pd on silica catalysts, and so was performed for the γ-Al_2O_3 supported catalysts. 5% Pd/γ-Al_2O_3 has a metal surface area of 58 $m^2 g^{-1}$ which gives a particle size of 7.2 nm, slightly higher than the average size from TEM of 4.1 nm. This is a much smaller discrepancy than was observed with the silica supported samples, indicating that the Pd is mainly present as Pd^0 but it is possible that some small particles are still oxidised. On the other hand, a much larger discrepancy is observed for the Pd surface area and TEM size of 5% Pd/γ-Al_2O_3+3Amine+H_2O, the metal surface area is 33.1 $m^2 g^{-1}$ which gives a size of 12.6 nm and TEM size much lower at 2.4 nm, this almost six times difference is much larger than was observed with any of the silica samples.

Prasad and co-workers studied alumina supported Pd particles and found at low loadings, after calcination, two reduction peaks were observed at higher temperatures than those reported by Tsang *et al.* and Chang *et al.* Samples with an average size below 3 nm displayed a peak at 100°C in TPR ascribed to the reduction of small PdO particles with a strong support-interaction and a high temperature peak is observed around 400°C, attributed to the reduction of a two-dimensional PdO surface phase. Thus it appears that whilst the stabilisation of PdO species is less pronounced for γ-Al_2O_3, it is still a significant problem particularly with small particles. As with the Pd on silica samples, in order to avoid the potential for damage/decomposition of the surface functional groups, the catalysts were tested without a high temperature reduction and as such the varying amount of active metallic Pd must be kept in mind. Table 3 displays the activity data for a range of support modified catalysts as well as some of the highly active polymer modified catalysts from the previous chapter.

Table 3– Formic acid decomposition activity of Pd on different supports

Pd Support	Initial Rate[a] (L g(Pd)$^{-1}$ min^{-1})	Final Rate[b] (L g(Pd)$^{-1}$ min^{-1})	Deactivation[c]	Total Gas[d] (L g(Pd)$^{-1}$)	TOF (h^{-1})
SiO_2 +3Amine+H_2O	0.282	0.054	5.2	11.93	432
γAl_2O_3	0.522	0.040	13.1	14.59	133
γAl_2O_3 +3Amine+H_2O	1.459	0.209	7.0	53.22	851
γAl_2O_3+NEt_2	0.798	0.087	9.2	26.09	237
γAl_2O_3+PEI	0.526	0.258	2.0	42.91	366
Type 87L	0.534	0.122	4.4	27.12	169
Type 87L+PEI	0.944	0.129	7.3	36.33	303
Type 87L+ PAAmine	1.665	0.351	4.7	81.97	616

[a]Rate of gas production in the first 10 min; [b]Rate of gas production in the final 20 min; [c]Calculated from initial rate divided by final rate; [d]Total gas produced in 2 hours (~4.25 mg of Pd in 10.575 mL of 1.4 M formic acid stirred at 25^{o}C); [e]TOF calculated from total moles of H_2 divided by moles of Pd per hour.

For γ-Al_2O_3 it is again seen that the introduction of propylamine functional groups to the surface of the support results in a dramatic electronic effect, as the metal surface area of 5% Pd/γAl_2O_3+3Amine+H_2O is decreased by almost 50% compared to 5% Pd/γAl_2O_3, but the initial rate has increased three-fold. The deactivation of 5% Pd/γAl_2O_3+3Amine+H_2O is also substantially decreased, indicating that the amine molecules are blocking some low coordinate sites, and as such the TOF is increased by six times over the Pd on un-functionalised support. On the other hand, for 5% Pd/γAl_2O_3+NEt_2 a much smaller increase in activity is observed over 5% Pd/γ-Al_2O_3. The Pd surface area of the 5% Pd/γ-Al_2O_3+NEt_2 catalyst (58.2 m^2 g^{-1}) is very similar to that of 5% Pd/γ-Al_2O_3, indicating the low number of functional groups on the

support and/or the sterically hindered nitrogen (due to the two ethyl groups) prevents the tertiary amine functionalised surface from stabilising the Pd particles and reducing their size. However, an interaction between the amine and the metal surface is still observed, with a 50% increase in initial activity and a 30% decrease in deactivation combining to produce almost double the volume of gas over two hours. The changes in initial rate and amount of deactivation over two hours clearly indicate electron donation from the amine to the Pd particles and some of the low coordinate sites are blocked to reduce poison formation, however substantially less than in the case of the primary amine.

Surprisingly, the 5% Pd/γAl_2O_3+PEI catalyst does not show any increase in the initial rate, but over the two hours there is a significant increase in the volume of total gas produced. This indicates that either there is no electronic promotion to the Pd or that any electronic promotion does not overcome the loss in metal surface area. From CO chemisorption the Pd surface area is 62.0 $m^2\ g^{-1}$, lower than expected from the particle size observed by TEM (4.1 nm); this difference in size and surface area may be due to some oxide formation but could also be due to the polymer blocking surface sites, which in chapter 4 was observed to cause a substantial decrease in the surface area of type 87L. As the metal surface area and initial activity of both the 5% Pd/γAl_2O_3+PEI and 5% Pd/γAl_2O_3 samples are similar, no electronic modification of the Pd particles is apparent; however the substantial change in deactivation indicates that PEI is still interacting with the particles. The dramatically decreased deactivation clearly indicates that the low coordinate sites of the Pd particles are blocked, agreeing with the site preference observed for tertiary amines in figure 5.8. Combining the low deactivation with the lack of electronic modification indicates that PEI is almost solely binding to low coordinate sites, resulting in reduced poisoning but limited electronic modification due to the electronically decoupled nature of these sites.[32]

From TGA analysis the molar ratio of Pd to PEI monomer units in the 5% Pd/γAl_2O_3+PEI sample is 1:2.8, lower than the 1:5 ratio used to modify type 87L and the 1:15 ratio used for colloidal Pd-PEI. This low ratio of Pd to PEI in 5% Pd/γAl_2O_3+PEI may mean there is only sufficient PEI to bind on the favoured low coordinate sites, limiting electronic promotion, whereas in PEI modified type 87L, only electronic modification is observed with no site selective binding. Not until the very high ratio used for colloidal Pd-PEI are both electronic promotion and reduced deactivation observed simultaneously, suggesting an optimal ratio of Pd to PEI is higher than can be achieved with 5% Pd loading.

The levels of deactivation of the metal oxide supported catalysts are all higher than those of type 87L, agreeing with TEM that the particle size is reduced, resulting in particles with a higher proportion of corner and edge sites that facilitate CO formation. The exception to this, and in significant contrast to the other metal oxide based catalysts, is 5% Pd/γAl_2O_3+PEI which has deactivation reduced by almost seven times from that of 5% Pd/γAl_2O_3. This stark difference between the ability of PEI and the other surface bound amines to block low coordinate sites is likely attributed to the higher mobility of PEI. Thus the limited decrease in deactivation observed for amines connected to the surface by propyl chains may be due to their inability to encapsulate the particles leaving many corner and edge sites unblocked.

Comparing these metal oxide supported catalysts with the results of type 87L in the previous chapter, it is clear that although amine functionalisation of the support increases the activity, none of the catalysts result in activities close to that of PAAmine modified 87L per gram of catalyst, likely due to the presence of Pd oxide species. However, the TOF's of metal oxide and 87L based catalysts are similar, and the promotion effects increase comparably. The

relative increase in TOF of 5% Pd/γAl_2O_3+3Amine+H_2O from 5% Pd/γAl_2O_3 is almost double that seen upon modifying 87L with PAAmine 1:5. This is a potential indication that the number of support amine groups interacting with the particle is more than with the polymer, highlighting the ability of this method to affect supported nanoparticles.

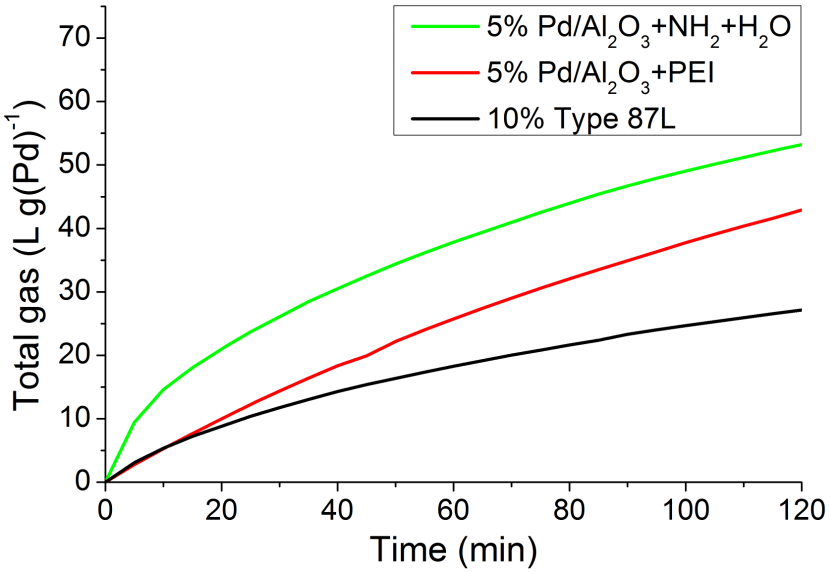


Figure 5.15– Activity plot for formic acid decomposition of a range of supported Pd catalysts. 4.25 mg of Pd stirred in 10.575 mL of 1.4 M formic acid at 25°C

The activity profiles displayed in figure 5.15 for the PEI and propylamine functionalised γ-Al_2O_3 based catalysts compared with that of type 87L clearly demonstrate the two different methods of promotion. The high initial rate of 5% Pd/γAl_2O_3+3Amine+H_2O combined with rapid deactivation is indicative of a high degree of electronic promotion on smaller particles but with limited geometric effects to reduce poison formation. This is in stark contrast to 5% Pd/γAl_2O_3+PEI, for which the much straighter line for gas production clearly indicates little poison production. Thus, two different methods have been developed to produce more active catalysts than type 87L, and although they do not result in more active catalysts than some of the polymer modified type 87L catalysts per gram of Pd, the TOF's are found to be similar or higher.

5.5 Conclusion

The results in this chapter have again highlighted the ability of organic functional groups to modify the catalytic properties of metal nanoparticles. Even though these functional groups are attached to the surface of a support, their ability to electronically modify supported particles is apparent. Geometric modification is also observed, but in all cases except for PEI modified γAl_2O_3, it is to a much lesser extent than for colloidal Pd-PEI particles. The limited geometric effects are attributed to the short alkyl chain inhibiting the amine from blocking all low coordinate sites. The turnover frequencies of these catalysts are high, rivalling those of the polymer modified type 87L in chapter 4, with the advantage that the organic groups are not lost upon washing. However, the ability of the metal oxide surfaces to stabilise PdO results in low activities per gram of Pd, limiting the current ability of these catalysts to be used for formic acid decomposition, which can potentially be overcome by alternate reduction methods or careful reduction of the Pd at elevated temperatures (just below amine decomposition temperature).

Although a number of issues still exist, such as how to reduce small metal particles without damaging the functional groups, the abilities of the support bound functional groups to modify the electronic and geometric properties of a supported catalyst is clear. As such, through tailoring the reduction conditions, functional groups, and support material, along with a range of other factors, this modification method may provide a route to highly active catalysts tuned for specific reactions, which can be operated in standard reactors at moderately elevated temperatures with typical flow rates.

5.6 References

[1] J. A. Lopez-Sanchez, N. Dimitratos, C. Hammond, G. L. Brett, L. Kesavan, S. White, P. Miedziak, R. Tiruvalam, R. L. Jenkins, A. F. Carley, et al., *Nature Chemistry* **2011**, *3*, 551–556.

[2] M. Yadav, T. Akita, N. Tsumori, Q. Xu, *Journal of Materials Chemistry* **2012**, *22*, 12582–12586.

[3] P. Luksirikul, K. Tedsree, M. G. Moloney, M. L. H. Green, S. C. E. Tsang, *Angewandte Chemie International Edition* **2012**, *51*, 6998–7001.

[4] J. Y. Kim, K. Park, S. Y. Bae, G. C. Kim, S. Lee, H. C. Choi, *Journal of Materials Chemistry* **2011**, *21*, 5999–6005.

[5] M. Carmo, M. Linardi, J. Poco, *Applied Catalysis A: General* **2009**, *355*, 132–138.

[6] C. A. Dyke, M. P. Stewart, F. Maya, J. M. Tour, *Synlett* **2004**, 155–160.

[7] J. L. Bahr, M. James, *Chemistry of Materials* **2001**, *13*, 3823–3824.

[8] M. Delamar, R. Hitmi, J. Pinson, J. M. Saveant, *Journal of the American Chemical Society* **1992**, *114*, 5883–5884.

[9] H. Leinonen, M. Lajunen, *Chemical Engineering Journal* **2011**, *172*, 557–563.

[10] L. Wan, X. Wang, S. Wang, S. Li, Q. Li, R. Tian, M. Li, *Journal of Physical Organic Chemistry* **2009**, *22*, 331–336.

[11] R. Chatti, A. K. Bansiwal, J. A. Thote, V. Kumar, P. Jadhav, S. K. Lokhande, R. B. Biniwale, N. K. Labhsetwar, S. S. Rayalu, *Microporous and Mesoporous Materials* **2009**, *121*, 84–89.

[12] K. M. K. Yu, I. Curcic, J. Gabriel, H. Morganstewart, S. C. Tsang, *The Journal of Physical Chemistry A* **2010**, *114*, 3863–3872.

[13] Y. Zhao, L. Deng, S. Tang, D.-M. Lai, B. Liao, Y. Fu, Q. Guo, *Energy & Fuels* **2011**, *25*, 3693–3697.

[14] G. Koehl, N. Keller, F. Garin, V. Keller, *Applied Catalysis A: General* **2005**, *289*, 37–43.

[15] L. Yang, Y. Li, *Biosensors & Bioelectronics* **2005**, *20*, 1407–1416.

[16] S. H. Hyun, S. Y. Jo, B. S. Kang, *Journal of Membrane Science* **1996**, *120*, 197–206.

[17] P. J. E. Harlick, A. Sayari, *Industrial & Engineering Chemistry Research* **2007**, *46*, 446–458.

[18] Q.-Y. Bi, X.-L. Du, Y.-M. Liu, Y. Cao, H.-Y. He, K.-N. Fan, *Journal of the American Chemical Society* **2012**, *134*, 8926–8933.

[19] M. Hair, *Journal of Non-Crystalline Solids* **1975**, *19*, 299–309.

[20] R. Al-Oweini, H. El-Rassy, *Journal of Molecular Structure* **2009**, *919*, 140–145.

[21] H.-S. Jung, D.-S. Moon, J.-K. Lee, *Journal of Nanomaterials* **2012**, *2012*, 1–8.

[22] W.-J. Shen, M. Okumura, Y. Matsumura, M. Haruta, *Applied Catalysis A: General* **2001**, *213*, 225–232.

[23] Z. Wang, B. Li, M. Chen, W. Weng, H. Wan, *Science China Chemistry* **2010**, *53*, 2047–2056.

[24] H. Cho, J. Park, B. Hong, Y. Park, *Bulletin of the Korean Chemical Society* **2008**, *29*, 328–334.

[25] K. Tedsree, T. Li, S. Jones, C. W. A. Chan, K. M. K. Yu, P. A. J. Bagot, E. A. Marquis, G. D. W. Smith, S. C. E. Tsang, *Nature Nanotechnology* **2011**, *6*, 302–307.

[26] M. Crespo-Quesada, J. M. Andanson, A. Yarulin, B. Lim, Y. Xia, L. Kiwi-Minsker, *Langmuir* **2011**, *27*, 7909–7916.

[27] T. Chang, J. Chen, C. Yeh, *Journal of Catalysis* **1985**, *96*, 51–57.

[28] N. Acerbi, S. Golunski, S. C. Tsang, H. Daly, C. Hardacre, R. Smith, P. Collier, *The Journal of Physical Chemistry C* **2012**, *116*, 13569–13583.

[29] C. Pan, K. Pelzer, K. Philippot, B. Chaudret, F. Dassenoy, P. Lecante, M. J. Casanove, *Journal of the American Chemical Society* **2001**, *123*, 7584–7593.

[30] R. Van Hardeveld, F. Hartog, *Surface Science* **1969**, *15*, 189–230.

[31] C. Henry, *Surface Science Reports* **1998**, *31*, 231–325.

[32] K. W. Zilm, L. Bonneviot, G. L. Haller, O. H. Han, M. Kermarec, *The Journal of Physical Chemistry* **1990**, *94*, 8495–8498.

[33] J. H. Ryu, S. S. Han, D. H. Kim, G. Henkelman, H. M. Lee, *ACS Nano* **2011**, *5*, 8515–8522.

[34] A. Ulman, *Chemical Reviews* **1996**, *96*, 1533–1554.

[35] X. Zhou, Y. Huang, W. Xing, C. Liu, J. Liao, T. Lu, *Chemical Communications* **2008**, 3540–3542.

[36] S. Zhang, Ö. Metin, D. Su, S. Sun, *Angewandte Chemie International Edition* **2013**, *52*, 3681–3684.

[37] M. Digne, P. Sautet, P. Raybaud, P. Euzen, H. Toulhoat, *Journal of Catalysis* **2002**, *211*, 1–5.

[38] D. Maciver, H. Tobin, R. Barth, *Journal of Catalysis* **1963**, *2*, 485–497.

Chapter 6

Metal Decoration

Chapter 6 Metal Decoration 170

6.1 Background 171

6.2 Objectives 173

6.3 Experimental details 174

6.4 Results and discussion 174

6.4.1 Decorated colloidal palladium 174

6.4.2 Bismuth decorated colloidal palladium 184

6.4.3 Silver decorated colloidal palladium 191

6.4.4 Silver decorated supported palladium 195

6.5 Conclusion 203

6.6 References 205

6.1 Background

The addition of a second metal to modify both the electronic and geometric properties of monometallic particles is widespread, with the majority of work focused on bimetallic particles with alloyed structures.[1–5] Bimetallic systems with alloy, core-shell and heterojunction (two attached particles) structures have been developed, which also display significantly modified catalytic properties.[6–9] An alternate method for modifying catalytic performance, widely used in electro-catalysis, is the decoration of metal surfaces with a sub-monolayer coverage of a foreign metal, producing a heterojunction-like structure with atoms or clusters of atoms of the second metal dispersed on the first.[10,11] Along with the electronic effects associated with the formation of an interface between the two metals, this technique has also been used for geometric modification via the decoration of specific sites on single crystal and metal nanoparticle surfaces.[12–14]

The deposition of a sub-monolayer of foreign atoms on metal and nanoparticle surfaces has provided significant insight into electro-chemical reaction mechanisms, although its use in heterogeneous modification has been limited.[15] The precise control of reduction in electrochemistry, by controlling the applied voltage, provides a high degree of control over the sites that some aqueous metal salts deposit onto, due to different activities of the surface sites to reduce the aqueous species.[13] This level of control is often not available in traditional heterogeneous catalyst synthesis, where the ability of metals to deposit preferentially onto a particular site of a metal surface can be highly dependent on the reaction conditions.

The effect of surface decoration on catalysis by metal surfaces is widely reported, but the majority of studies involve the destruction of large surface ensembles or electronic modification as the key mechanisms for enhancing activity or selectivity.[16,17] The site

selective modification of metal nanoparticles for enhanced performance as heterogeneous catalysts has been reported but is a much less widely used technique.[12,14]

Gauthard and co-workers studied the effects on nitrate reduction resulting from the deposition of Cu, Ag, and Au onto γ-alumina supported Pt and Pd nanoparticles.[17] Using a surface controlled reduction technique to ensure the deposited metal formed on the Pt or Pd particles, a high degree of interaction between the metals was achieved in all cases. This was demonstrated through significant changes in the IR peaks of adsorbed CO and the temperature-programmed reduction profiles from those of the monometallic catalysts. The reduction in the proportion of bridging CO on the Pd/Al_2O_3 catalyst after addition of Cu indicated it was selectively deposited onto terrace sites. On the other hand, Ag resulted in a similar decrease in both the linear and bridging CO peaks, indicating random coverage of the surface. Although the activities of the decorated catalysts are found to depend on the ability of the deposited metal to reduce nitrate, rather than any modification of the Pd or Pt surface, the effects of decoration are apparent nonetheless.

In contrast to nitrate reduction, geometric modification through the selective decoration of a particular surface site was found to be key for selectivity changes in 1-hexyne hydrogenation.[14,17] Anderson *et al.* found that decoration of low coordinate sites on the Pd surface, in a $Pd/\gamma Al_2O_3$ catalyst, by Bi was highly influential in determining the products of the hydrogenation of 1-hexyne.[14] The TOF for the initial hydrogenation of 1-hexyne to 1-hexene was not affected by the blockage of these sites, but the subsequent hydrogenation and isomerisation of the desired 1-hexene product was greatly suppressed. As the double bond shift of terminal alkenes occurs preferentially on edge and corner sites, selective decoration of these sites through Bi modification increased selectivity for the desired product, 1-hexene.

Tsang *et al.* found decoration of Pt nanoparticles with Co also selectively blocks low coordinate sites, observed by IR of adsorbed CO.[12] Under their reduction conditions, only low coordinate sites could take up Co, even with a large excess of Co^{2+} in solution. These decorated particles demonstrated increased selectivity for C=O hydrogenation over C=C hydrogenation in cinnamaldehyde hydrogenation. Interestingly for the decorated Pt, the larger particles show a lower selectivity than smaller particles, even though all low coordinate sites should be blocked in both cases. The additional selectivity effects are attributed to a concurrent electronic promotion of the surface, involving electronic donation from the Co to Pt. The δ^- Pt destabilises C=C adsorption and the δ^+ Co attracts the carbonyl group. The higher selectivity of smaller particles is attributed to the limited range of this electronic modification, with all of the area between the Co doped corner sites effectively modified. Whereas for larger particles, the limited range prevents complete electronic modification of the terrace sites, decreasing their selectivity.

6.2 Objectives

As previous reports have demonstrated, the decoration of metal nanoparticles can result in both electronic and geometric modification of metal surfaces. From the proposed mechanism of formic acid decomposition and the results discussed in chapters four and five, the performance of formic acid dehydrogenation catalysts can be enhanced by both of these methods. Firstly, increasing electron density on Pd promotes the rate determining C-H cleavage. Secondly, the blockage of low coordinate sites prevents formic acid dehydration, reducing the formation of poisoning CO and the associated deactivation.

As such, the aim of this chapter is to tailor the surface of Pd nanoparticles, through the deposition of a second metal, to enhance their activity and selectivity for formic acid dehydrogenation.

6.3 Experimental details

Extensive experimental details of the synthesis procedures, characterisation methods and catalyst testing are given in chapter three; a brief summary of catalyst synthesis is given here. Pd particles stabilised by PVP were synthesised using a similar method to that used by Bonet *et al.*, involving ethylene glycol reduction of $Pd(NO_3)_2$, with a 1:10 molar ratio of Pd to PVP monomer units.[18] Supported Pd on carbon was synthesised using a precipitation-deposition method, with room temperature hydrogen reduction. Decoration of these particles followed the method of Gauthard *et al.*, using a hydrogen pre-treatment of the preformed particles but with an additional reduction step.[17] The modified Pd-PVP particles were precipitated using an acetone/hexane mixture, washed with acetone and dried in air at room temperature. Pd/C modified catalysts were filtered, washed extensively with water and dried in air at 85°C.

6.4 Results and discussion

6.4.1 Decorated colloidal palladium

A range of metals were selected to decorate preformed PVP stabilised Pd nanoparticles; the metals have all been reported to selectively decorate sites on nanoparticle or single crystal surfaces, or have been used to enhance the activity of Pd nanoparticles for formic acid

decomposition. These metals are Cu, Ag, and Au all reported to enhance Pd activity for formic acid decomposition, and Co, Sn, Te, and Bi reported to decorate specific sites.[5,12,14,15]

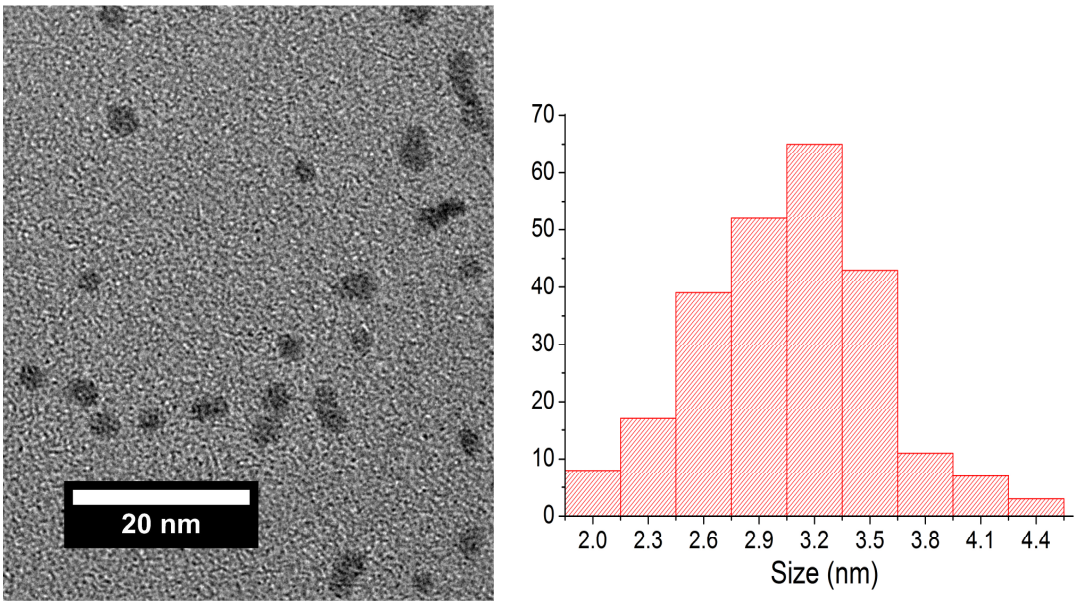


Figure 6.1– TEM micrograph and size distribution histogram of Pd-PVP 1:10

The synthesis of Pd particles with a 1:10 ratio of PVP was confirmed by XRD, further details are given in chapter 4. From XRD the size was calculated as 3.2 nm, in good agreement with TEM which found the size to be 3.0 nm. TEM also demonstrated a relatively narrow size distribution, with the particles having mainly spherical/cubo-octahedral shape. From the work of van Hardeveld and Hartog the number of low coordinate sites - marked as C(9,7), C(6,6), and C(5,7) in figure 6.2 - was calculated, using a 3.2 nm Pd cubo-octahedron to model the synthesised particles.[19] The percentage of corner, edge, and terrace atoms was 5.2%, 22.8%, and 72.0% of the surface and 2.0%, 8.7%, and 27.5% of the total atoms in the particle, giving ~38% of the total atoms on the nanoparticle surface.

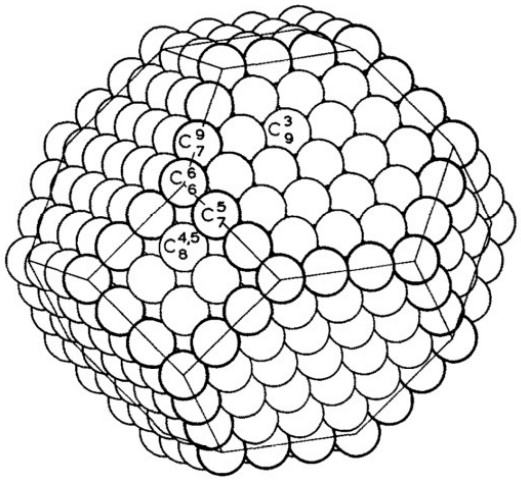


Figure 6.2– Model cubo-octahedral nanoparticle reproduced from reference[19]

As 10.7% of the total atoms in a particle are calculated to be in low coordinate sites, a 1:0.15 molar ratio of Pd to decorating metal (equivalent to 15% of the Pd atoms) was selected to modify the samples. This ratio allows more than sufficient decorating metal to cover all low coordinate sites, assuming a 1:1 coverage. Particles were decorated by treating the un-precipitated Pd-PVP particles with hydrogen, to produce a Pd hydride surface, followed by addition of, and stirring with, the relevant metal precursor. During this time, sacrificial reduction of the metal salt onto the particle surface is expected to produce a surface bound metal species. The sacrificial reduction is followed by re-heating in ethylene glycol to ensure the metal salt is completely reduced. XRD analysis was performed on the samples to ensure that formation of separate particles had not occurred and no single metal phases of decorating metal were observed.

Table 1 – Formic acid decomposition activity of Pd-PVP nanoparticles decorated with a 1:0.15 molar ratio of decorating metal.

Catalyst	Initial Rate[a] (L g(Pd)$^{-1}$ min^{-1})	Final Rate[b] (L g(Pd)$^{-1}$ min^{-1})	Deactivation[c]	Total Gas[d] (L g(Pd)$^{-1}$)
Pd-PVP	0.106	0.0066	16.06	2.81
+Cu	0.035	0.0069	5.07	1.67
+Ag	0.264	0.0250	10.56	8.98
+Au	0.094	0.0066	14.24	2.36
+Co	0.035	0.0053	6.60	1.47
+Sn	0.049	0.0056	8.75	1.83
+Bi	0.070	0.0200	3.50	3.80
+Te	0.010	0.0038	2.63	0.59

[a]Rate of gas production in the first 10 min; [b]Rate of gas production in the final 20 min; [c]Deactivation calculated from initial rate divided by final rate; [d]Total Gas produced in 2 hours ($0.15x10^{-3}$ moles of Pd in 15.860 mL of 1.4 M formic acid stirred at 25^{o}C)

The decorated particles were tested for formic acid decomposition over two hours, with the results displayed in table 1. Decoration with a 1:0.15 ratio would, assuming a monolayer coverage and 1:1 atom blockage, result in loss of 40% of the Pd surface area; as such the activity of the particles is expected to be reduced proportionally, with total gas production reduced to approximately 1.7 L g(Pd)$^{-1}$. In all cases except Au, the decorating metals have been found to be inactive for formic acid decomposition with no reports in the literature of monometallic particles demonstrating activity.

The total volume of gas produced over two hours by a number of the decorated samples (Cu, Co, Sn) strongly corresponds to that expected from a 40% loss of surface area, indicating the decrease in Pd surface area dominates any promotional effects of the decorating metal. Au decoration results in a similar volume of total gas production as the un-decorated Pd-PVP, as well as similar initial and final rates, indicating the modifying effect of Au overcomes the loss in Pd surface area. The effects of Au decoration are complicated by the reports that small gold nanoparticles are active for formic acid decomposition, making it difficult to isolate the promotional effects to Pd from their own catalytic activity.[20,21]

The three other decorating metals show the most extreme effects; Ag and Bi result in an increased gas production, overcoming the loss of Pd surface area, whereas Te demonstrates a dramatic decrease in gas production, much more than is expected from loss in Pd surface area alone. To examine the reasons behind the changes in activity of the decorated Pd-PVP particles, all samples were examined using FTIR of chemisorbed CO. In all cases (except for Te) the intensity has been normalised by the bridging CO peak.

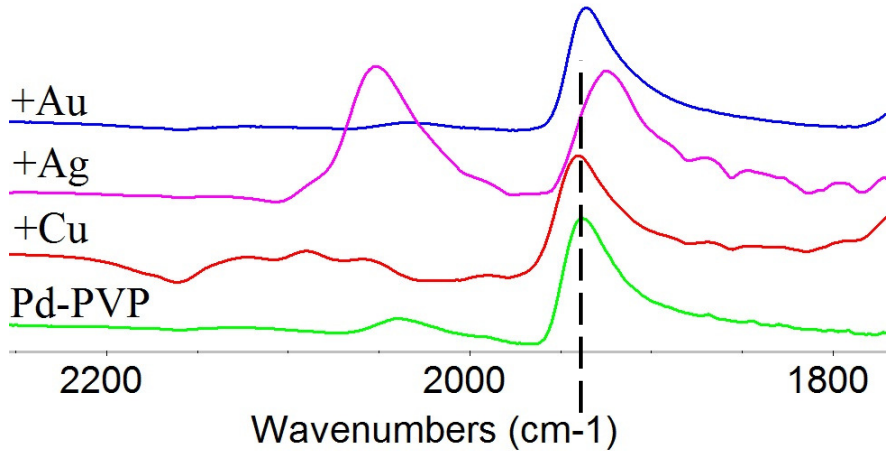


Figure 6.3– FTIR of CO adsorbed on Pd-PVP decorated with a 1:0.15 molar ratio of group 11 metals

Figure 6.3 displays the CO FTIR of particles decorated with group 11 metals, which have all been reported to promote formic acid decomposition activity when alloyed with Pd.[5] A clear

shift to lower wavenumbers is observed for the bridging peak of CO on Ag decorated Pd-PVP, with a much smaller shift seen for Au decoration. Cu decoration results in a very slight shift to higher wavenumbers. As the shift of CO in FTIR is related to the electron density on the Pd surface, it indicates that Ag and Au decoration result in electronic donation to Pd (Au decoration only has a small donation), whereas Cu decoration results in a small withdrawing effect. The reports of Tsang *et al.* demonstrate the degree of electron transfer correlates with the relative work function of the metal compared to Pd (5.12 eV), electron transfer occurs from the low to high work function metal.[22] The different shifts of bridging CO on the decorated particles can be explained by comparing the work functions; Ag (4.26 eV) is much lower than Pd, resulting in a high degree of electron transfer, whereas Au (5.1 eV) results in only a small amount.[22] On the other hand, Cu (4.65 eV) would be expected to cause a shift between those of Ag and Au. [22] As Cu nanoparticles are readily oxidised, oxide formation is expected and is likely the cause of electron withdrawal from Pd.[23] The initial rates of formic acid decomposition and the volumes of total gas produced correlate with the shifts observed by FTIR, with Ag and Au showing promotional effects over the Pd-PVP with 15% surface area lost, and Ag resulting in a much higher degree of promotion than Au.

Comparison of the intensity of the linear peak can indicate any site preference in metal deposition, but unfortunately the FTIR of CO adsorbed on Cu and Ag mask observation of the linear bound CO on Pd for these samples.[24,25] This prevents determination of site specific decoration, but comparison of the deactivation results (table 1) indicate that Ag is not selectively deposited as the degree of deactivation seen over two hours is not significantly altered. Cu shows a greatly decreased deactivation, but as seen in chapter 4, this occurs when the activity is dramatically lower than the initial catalyst. Gauthard *et al.* report that Cu deposits selectively onto terrace sites on the Pd surface, but from FTIR of adsorbed CO a

bridging species is still observed indicating total blockage of the terrace sites has not occurred.[17] The close agreement between the activity of Cu modified Pd-PVP and that expected from the non-selective loss of 40% of the Pd surface area also indicates no preferential site blockage. Although in the case of Au, the linear peak is significantly weakened and the deactivation is similar to that of undecorated Pd-PVP, demonstrating that Au suppresses linearly bound CO formation, but not through blockage of the low coordinate sites. A low proportion of linear CO was also observed by Tsang *et al.* for Au@Pd nanoparticles.[25]

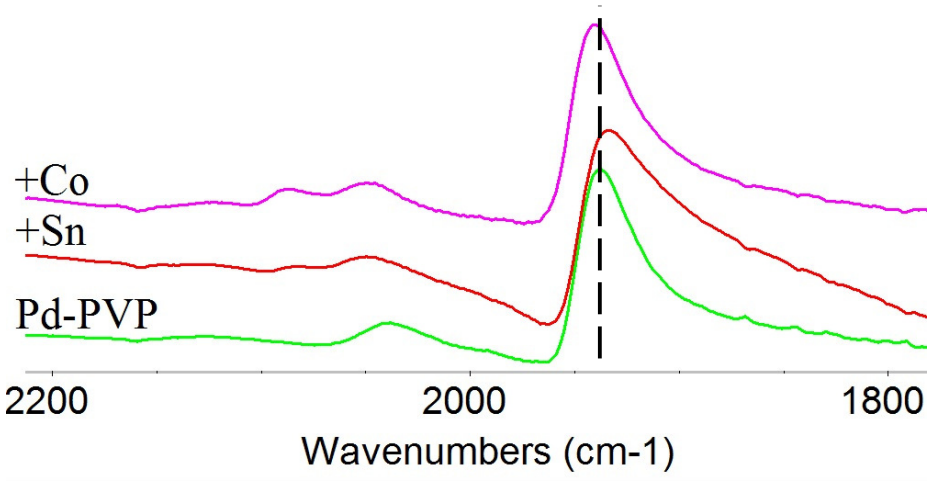


Figure 6.4– FTIR of CO adsorbed on Pd-PVP decorated with a 1:0.15 mole ratio of Sn and Co

The gas production for Co and Sn decorated Pd-PVP particles show a slightly lower and higher activity than expected for Pd-PVP particles with 40% of the surface blocked. The difference in activity can be explained from the observed shift of bridging CO from FTIR, figure 6.4, with Sn shifted to lower wavenumbers and Co shifted slightly higher indicating electron donation and withdrawal effects, respectively. In both cases the linear and bridging species are present in agreement with the observed deactivation, indicating no selective site blockage has occurred. Sn and Co decoration result in approximately 60% of the undecorated Pd-PVP's deactivation as would be expected from random coverage of 40% of the surface,

covering both low coordinate and terrace sites. The non-selective deposition of Co conflicts with previous reports where it is shown to decorate low coordinate sites, but this may be due to the very different reduction conditions and a different metal precursor.[12]

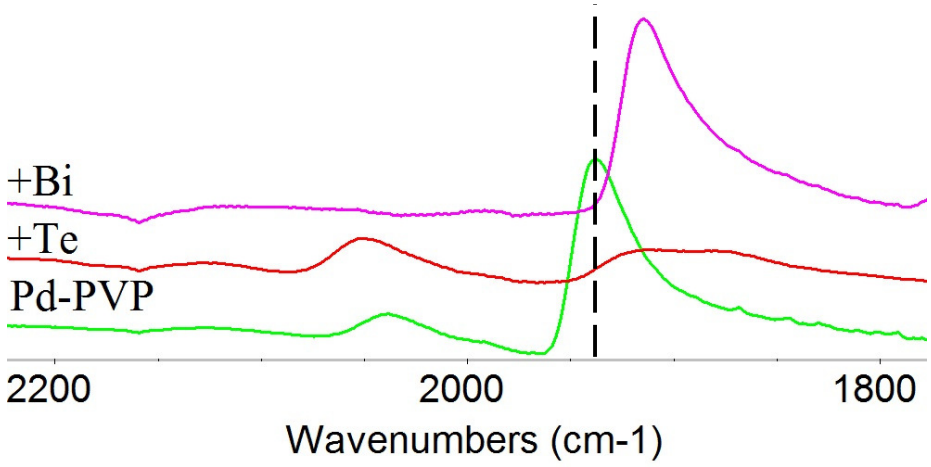


Figure 6.5– FTIR of CO adsorbed on Pd-PVP decorated with a 1:0.15 mole ratio of Te and Bi

In figure 6.5, a strong site selective modification is observed with the decoration of Pd-PVP by Te and Bi, with Bi appearing to reduce preferentially on the low coordinate sites and Te on terrace sites. The very low deactivation observed with Bi decorated particles (3.5) compared to undecorated Pd-PVP (16.06) indicates the blocking of low coordinate sites (responsible for linearly bound CO) is preventing the dehydration reaction pathway that causes catalyst poisoning. This blockage of low coordinate sites is in agreement with the reports of Anderson *et al.*, who observed a similar effect on supported Pd particles.[14] A clear electronic modification of the surface is also apparent for Bi decorated Pd-PVP, with a downshift of the bridging CO peak observed in agreement with the work functions (Bi = 4.22 eV, Pd = 5.1 eV). In the case of Te decoration, bridging CO is largely blocked, which correlates with the drastically decreased activity due to suppression of the dehydrogenation reaction pathway. Comparison between the linear CO peaks on Pd-PVP and Pd-PVP+Te indicates electron withdrawal from the metal is also occurring, which is surprising as the work function of Te

(4.95 eV) is lower than that of Pd. However, the decoupled nature of the low coordinate sites makes them unreliable for determining the electronic properties of the overall nanoparticle.[26]

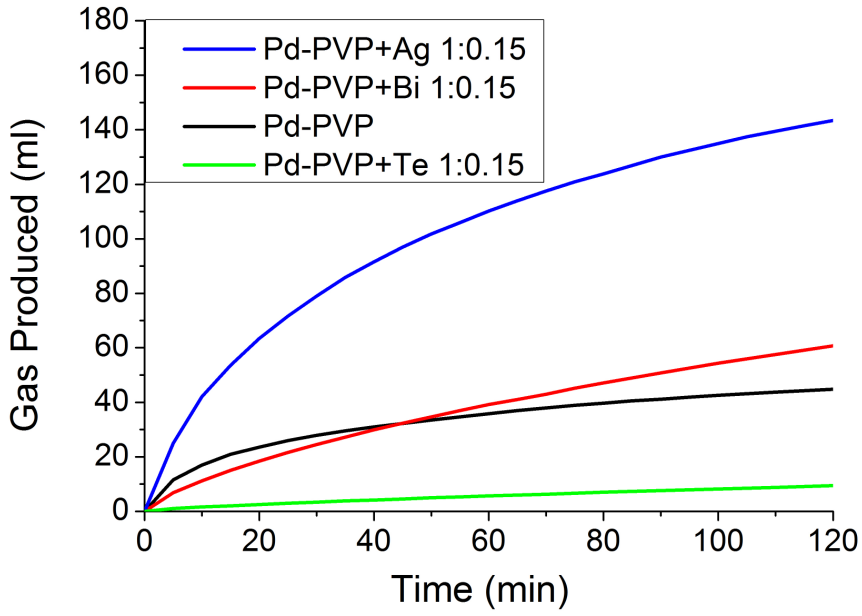


Figure 6.6– Activity plot of Pd-PVP decorated with 1:0.15 molar ratios of Ag, Bi, and Te. $0.15x10^{-3}$ moles of Pd in 15.860 mL of 1.4 M formic acid stirred at 25°C

The formic acid decomposition results, and corresponding CO-FTIR results, clearly highlight three very interesting cases of decorated Pd-PVP. Firstly, the addition of Ag displays dramatic electronic donation effects which overcome the loss of Pd surface area to produce a highly active catalyst. Secondly, Bi decoration appears to decrease deactivation through suppression of the formic acid dehydration reaction. Finally, decoration with Te appears to prevent the dehydrogenation of formic acid, resulting in a low activity catalyst due to competitive blocking of terrace sites.

In the case of Te decoration, an additional reduction step was required to observe the decreased activity for formic acid decomposition. After ethylene glycol reduction, the activity of the Te decorated particles was very similar to that of the undecorated particles, but the FTIR shows blockage of bridging CO sites. If $NaBH_4$ reduction was performed after

sacrificial reduction, the activities displayed in table 1 and figure 6.6 are observed. It appears that ethylene glycol reduction at 120°C does not fully reduce Te^{4+} to Te^{0}, resulting in a species that is removed in dilute formic acid, whereas $NaBH_4$ forms Te^{0} which is stable in formic acid. Addition of $NaBH_4$ to preformed Pd-PVP particles, without Te addition, does not result in significant changes in activity.

Clearly these results pose two important questions: Why do some metals show site selective decoration? What determines a metals preferred decoration site? Gauthard *et al.* attributed the selective deposition of Cu on terrace sites to the surface controlled reduction method and the +2 state of the Cu ion.[17] The surface controlled reduction uses a surface metal-hydride species to reduce the metal salt, thus for Cu^{2+} two adjacent metal-hydrides are required for full reduction so terrace sites are preferred. Whereas the Ag^{+} salt only requires a single metal-hydride site to reduce, and will decorate the surface indiscriminately.

Gauthard's mechanism for site selective deposition does not stand for the wider range of metals used in this study. In this work, Co, Sn, and Cu were all in the +2 oxidation state and the oxidation states for Ag, Au, Bi, and Te were +1, +3, +3, and +4, respectively. From Gauthard's proposal, all +2 salts would be expected to decorate terrace sites, which is not observed from FTIR or decomposition results. From the results in chapter 4 and the reports of Ryu *et al.*, atoms with a single lone pair are expected to show a preference for binding on corner sites.[27] Thus, we propose that the electron arrangement of the metal salt is an important factor in determining the favoured adsorption site.

The preference of post-transition metals (PTM) to bind selectively to different sites is widely reported in the literature, in agreement with our observations for Bi and Te.[14,15] A key

property of these PTM species, widely noted to affect their crystal structures, is the presence of stereo-chemical lone pairs, akin to the lone pairs of the molecular nitrogen and sulphur species studied by Ryu.[27,28] Thus, we predict that directional lone pairs have a key role in determining the site specificity of deposition.

We found that Bi^{3+}, with one stereo-chemical lone pair, binds selectively on low coordinate sites in a similar manner to nitrogen as discussed in chapter 4. In the case of Te^{4+} -with a higher reduction potential than Bi^{3+} (0.57 eV versus 0.317 eV) and a possible Te^{2+} state- partial reduction to Te^{2+} with two stereo-chemical lone pairs is envisaged that would preferentially bind in a bridging mode on terrace sites. This partial reduction step is proposed due to the requirement of $NaBH_4$ reduction. If no $NaBH_4$ reduction is performed, an adsorbed Te species (possibly Te^{2+}) is present on the terrace sites and no bridging CO is observed. But upon testing in formic acid, the adsorbed species is removed resulting in an activity similar to unmodified Pd-PVP. In the case of the transition metal salts, with no stereo-chemical lone pairs, random deposition is expected.

6.4.2 Bismuth decorated colloidal palladium

Decoration of Pd-PVP with Bi demonstrated both site selective modification and electronic donation effects enhancing formic acid decomposition, so was investigated further to gain an understanding of the importance of each factor. A range of Pd-PVP+Bi ratios were prepared and characterised by XRD; figure 6.7 displays the position of the (111) peak plotted against Bi content and the calculated peak position for PdBi alloys with a range of ratios. The alloy (111) peak positions were calculated using Vegards law by substituting Bi into the Pd lattice, similar to the method reported by Fairclough *et al*.[29]

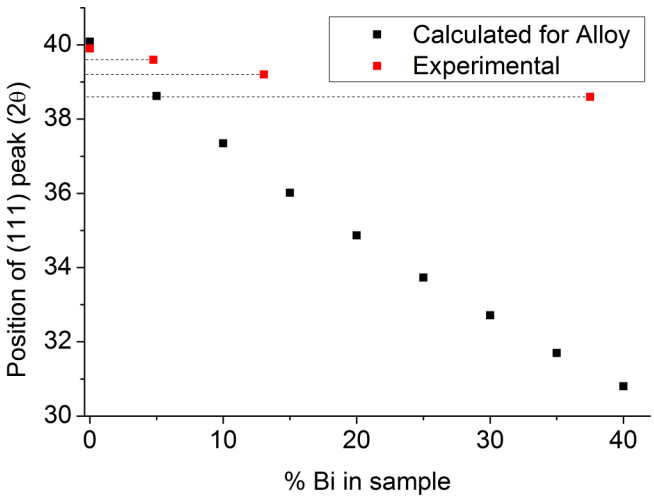


Figure 6.7– Position of the (111) peak for Pd-PVP, decorated Pd-PVP+Bi particles and the calculated position of the (111) peak for PdBi alloys

It can clearly be seen that, whilst some degree of peak shift is observed for the experimental Pd-PVP+Bi particles, it is much less than expected for total alloying of Bi with Pd-PVP. For the Pd-PVP+Bi 1:0.6 (37.5% Bi) particles, a maximum of 5% of the Bi is alloyed, indicating the vast majority is still present on the surface of the particles. In the case of the other Pd-PVP+Bi ratios, a similarly low proportion of the Bi is potentially alloyed. The observed shift in the (111) peak could also be due to strain induced by the difference in lattice parameters of the Pd particle surface and the decorating Bi.[30] Additionally, Wenkin *et al.* noted the preference of Bi to diffuse to the surface of a mixed PdBi phase due to the lower surface energy than Pd; this is in agreement with the results in figure 6.7, indicating that Bi does not favourably alloy with Pd.[31]

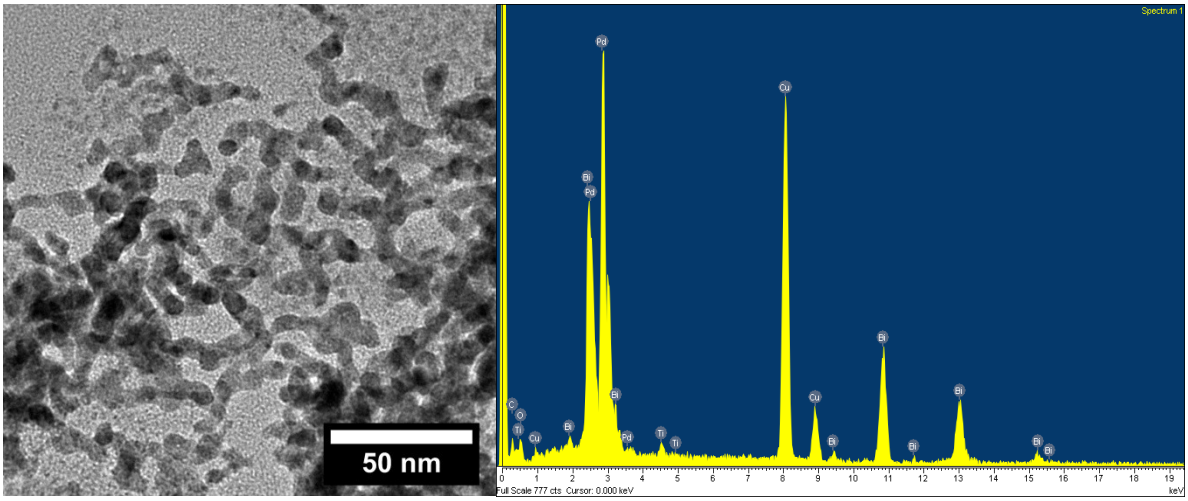


Figure 6.8– TEM micrograph and EDX spectrum of Pd-PVP+Bi 1:0.60

TEM analysis in table 2 clearly demonstrates the particles have grown with increasing Bi content, and EDX results illustrate that the Pd to Bi ratio is very close to the synthesised value in all cases, except for 1:0.60. For Pd-PVP+Bi 1:0.60, some Bi rich regions were identified indicating that Bi had not been totally reduced onto the surface of the particles, likely due to the ratio producing over a monolayer coverage. As such, a portion of the Bi was prevented from undergoing sacrificial reduction onto the Pd surface and formed Bi particles. The significant growth of the particles observed from TEM conflicts with sizes calculated by XRD (which indicate minimal size change) indicative of strain effects in the larger particles resulting in additional broadening of the XRD peaks.

Table 2 – Size and composition details of Bi decorated Pd-PVP particles

Sample	Pd:Bi ratio[a]	Size XRD (nm)[b]	Size TEM (nm)[c]
Pd-PVP	N/A	3.2	2.95
Pd-PVP+Bi 1:0.05	1:0.055	3.3	3.47
Pd-PVP+Bi 1:0.15	1:0.170	3.6	4.93
Pd-PVP+Bi 1:0.60	1:0.470	3.3	7.17

[a]Ratio of Pd and Bi from EDX; [b]Particle size calculated from the Pd (220) peak; [c]Particle size from the average of at least 200 particles

The particles with the desired Bi ratios of surface decoration were then characterised by CO-FTIR, figure 6.9. The relative intensities of linear and bridging species appear to correlate very well with the modelled number of sites on the particle surface. With a Pd to Bi ratio of 1:0.05, there is insufficient Bi to cover all low coordinate sites and a peak from linear CO is still observed, although decreased in intensity. With a 1:0.15 ratio –calculated to be sufficient to cover all low coordinate sites– no linear CO species is observed indicating total blockage of the low coordinate sites. At Pd to Bi ratios above 1:0.15, Bi is expected to deposit on the terrace sites and at a 1:0.60 ratio –more than sufficient to cover the particle surface– no CO is observed indicating all surface sites are blocked.

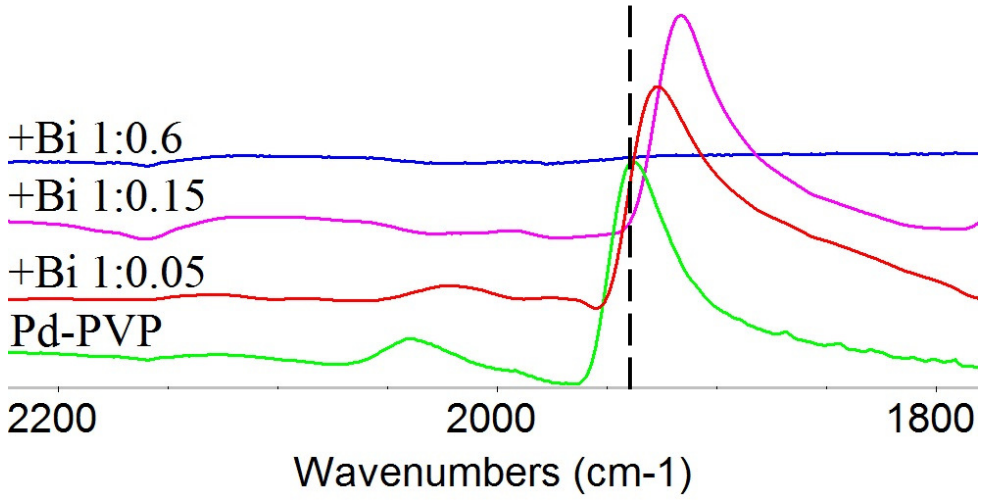


Figure 6.9– FTIR of CO adsorbed on Pd-PVP decorated with various ratios of Bi

In figure 6.9, an increasingly large electronic donation to the Pd surface is clearly seen with increasing Bi coverage. Interestingly, as was shown in table 2, this electronic effect does not overcome the loss in surface area and a decrease in initial rate is observed. However for Ag, the electronic promotion can clearly overcome the lost surface area resulting in an increased initial rate. This result can be explained by the report of Tsang *et al.*, who found that the range of electronic modification for Co decorating Pt corners was limited over the terrace sites.[12] Taking this into account, it would be expected that whilst the low work function of Bi does result in a large electron donation to Pd, it is localised close to the corner and edge sites. The position of the CO bridging peak is thus averaged with the bridging species that are not electronically modified in the middle of the terraces. As shown in figure 6.10, more of the available terrace sites become modified electronically with increasing Bi coverage, explaining the increasing shift of bridging CO observed with increasing Bi. In contrast to this, the random dispersion of Ag over the Pd surface electronically influences the surface sites indiscriminately, allowing the loss in surface area to be overcome even though the work function for Ag suggests the electronic effect should be slightly less than for Bi.

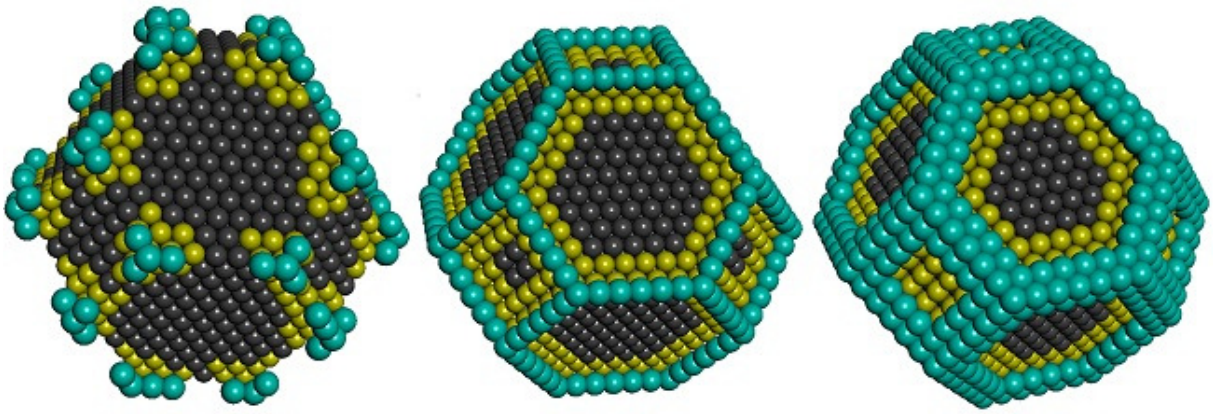


Figure 6.10– Schematic of the electronic effects at different levels of Bi decoration on Pd nanoparticles. Grey, yellow and turquoise atoms represent Pd, electronically modified Pd, and Bi, respectively

The Pd-PVP particles decorated with various ratios of Bi were tested for formic acid decomposition and the total gas produced over 2 hours is shown in figure 6.11.

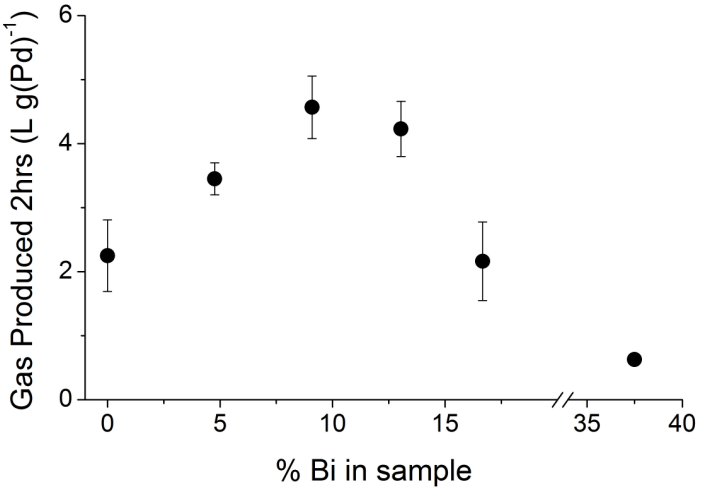


Figure 6.11– Total gas production over 2 hours for Pd-PVP decorated with various ratios of Bi. $0.15x10^{-3}$ moles of Pd in 15.860 mL of 1.4 M formic acid stirred at 25°C

The clear volcano relationship displayed in figure 6.11 typically indicates a trade-off between two competing factors, in this case prevention of poison formation and the blocking of active sites for formic acid dehydrogenation. For low Pd to Bi ratios the decrease in initial rate is low, indicating highly selective blockage of low coordinate sites. The initial rate for Pd-PVP is 0.106 L $g(Pd)^{-1}$ min^{-1} and only decreases to 0.098 L $g(Pd)^{-1}$ min^{-1} for Pd-PVP+Bi 1:0.10.

Above this ratio the initial rate drops significantly to 0.070 L $g(Pd)^{-1}$ min^{-1} for Pd-PVP+Bi 1:0.15, indicating the terrace sites are starting to become blocked. Deactivation is also dramatically decreased giving a much straighter activity profile, as demonstrated in figure 6.6, but does not decrease significantly above a Pd to Bi ratio of 1:0.10. As a result of the changes in initial rate and levels of deactivation, the total gas production over 2 hours gives the volcano relationship in figure 6.11, with maximum gas production observed for a 1:0.10 ratio of Pd to Bi. The 9.09% Bi content of the 1:0.10 sample is very similar to the calculated percentage of corner and edge sites on a 3.2 nm Pd particle (10.7%). Above the 1:0.10 ratio terrace sites start to be blocked and activity is decreased until at a 1:0.60 ratio, almost all Pd is covered resulting in very little gas production.

6.4.3 Silver decorated colloidal palladium

Although the Ag decorated particles displayed no site selective blockage, they showed the largest increase in activity and so were investigated further to understand the promotion mechanism. A range of ratios were prepared and characterised by XRD, in figure 6.12 the peak position of the Pd (111) peak is plotted against Ag content in the Pd-PVP particle.

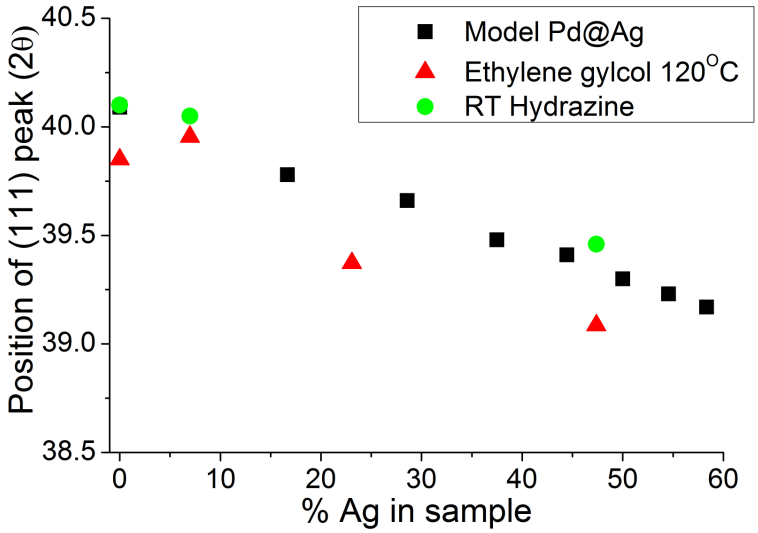


Figure 6.12– Position of (111) peak for Pd-PVP+Ag particles, with Ag reduced by ethylene glycol at 120°C or N_2H_4 at room temperature, and calculated Pd@Ag core-shell particles

The shift of the (111) peak observed with increasing Ag content matches quite closely with that expected of a PdAg alloy, calculated using Vegards law, and both correlate with values of PdAg alloys reported in the literature.[4] Due to the limited difference in the crystal structures of Ag and Pd (both FCC and with lattice parameters of 4.090 Å and 3.8907 Å respectively), the peak shift calculated for alloying is substantially less than that for PdBi alloys. Pd and Ag are reported to undergo facile alloy formation and with the Ag reduction occurring at 120°C, there was potential for alloying.[32] To reduce atom mobility, and as such to reduce the potential for alloy formation, Pd-PVP+Ag samples were prepared as in 6.4.1, but with a room

temperature N_2H_4 reduction used to ensure total reduction of Ag, rather than the 120°C ethylene glycol reduction used previously. Figure 6.12 clearly shows that these room temperature decorated particles, show a similar trend in Pd (111) peak shift as the ethylene glycol reduced samples, even though alloy formation was not expected with the low amount of available energy.

To gain further insight into the effects of adding Ag atoms to the surface of a Pd-PVP particle, Pd@Ag core-shell particles were computationally modelled with different levels of Ag coverage. Strain from the lattice mis-match was included in the model particle and the XRD pattern calculated from this particle, using the same method that has been reported in the literature for core-shell particles.[29,33] The results of the simulation can be observed in figure 6.12 and demonstrate the significant shift even low coverages of Ag can have on the Pd (111) peak. The Pd@Ag core-shell model shows strong agreement with our room temperature N_2H_4 decorated Pd-PVP+Ag particles and, if variation in the undecorated Pd-PVP samples is taken into consideration, a good agreement with the Pd-PVP+Ag reduced in ethylene glycol at 120°C sample is also found. The shift observed in undecorated Pd-PVP particles is due to instrumentation variation or small quantities of interstitial β-H still present in some of the samples. The lattice expansion of Pd caused by interstitial atoms, especially hydride, is widely reported and although all β-H should be decomposed above ~80°C, the presence of ethylene glycol may stabilise these species.[34]

Thus, the decorated nature of the Pd-PVP+Ag particles (using the 120°C ethylene glycol reduction to ensure full Ag reduction) is strongly suggested by XRD, from the good agreement with both the low temperature samples and the computational modelling of core-

shell structures. As such, further characterisation was performed using CO-FTIR to gain an understanding of electronic modification.

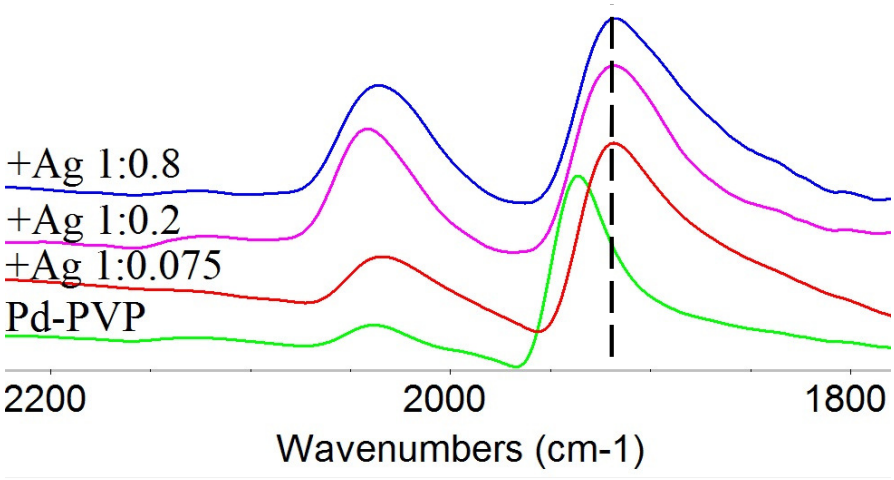


Figure 6.13– FTIR of CO adsorbed on Pd-PVP decorated with various ratios of Ag

In stark contrast to the FTIR of CO adsorbed on Bi decorated particles, no increase in electronic donation to Pd is observed with increasing Ag content. As we mentioned previously, the linear CO peak from Pd is obscured by CO adsorption on Ag, but site selective deposition of Ag was ruled out due to the similar level of deactivation as the undecorated particles, in dramatic contrast to the site selective Bi and Te decoration. The random deposition of Ag on the surface of Pd-PVP is also supported by the constant shift observed in the bridging CO peak with increasing coverage. We have seen from Bi decoration and the reports of Tsang *et al.* that the range of electronic modification is limited, thus for Ag electronic modification to be constant it must be well dispersed over the surface.[12] The fact that with high ratios of Pd to Ag, a Pd bridging peak is still observed even though there is sufficient Ag to more than totally cover the surface indicates the formation of Ag clusters rather than layered coverage.

A range of Ag decorated Pd-PVP particles with Pd to Ag ratios of 1:0.075, 1:0.15, 1:0.30, 1:0.45 and 1:0.90 were prepared, resulting in 7%, 13%, 23%, 31% and 47% Ag in each

sample, respectively. These particles were tested for formic acid decomposition over 2 hours. The theoretical surface coverage, assuming a 1:1 Ag on Pd adsorption and monolayer formation, would range from 20% to over twice total coverage.

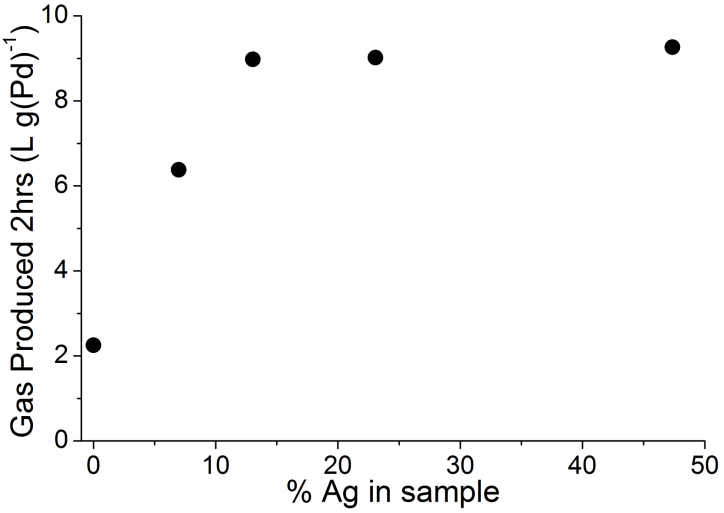


Figure 6.14– Total gas production over 2 hours for Pd-PVP decorated with various ratios of Ag. 0.15×10^{-3} moles of Pd in 15.860 mL of 1.4 M formic acid stirred at 25°C

A significant difference is observed between the effects of increasing Ag content in figure 6.14 and increasing Bi content in figure 6.11. In the case of Ag, maximum activity requires a Pd to Ag ratio of 1:0.15 (slightly higher than with Bi decoration) that would result in ~40% surface coverage, if Ag formed a monolayer. If Ag is highly dispersed on the Pd surface, the electronic modification of all surface sites can be envisaged, even with a short modification range. Whilst increasing Ag content is found not to result in increased electronic modification, the high activity is maintained even at ratios where total surface coverage could be achieved, agreeing with FTIR that Ag cluster formation prevents total coverage of the Pd surface.

Comparing the initial rates of the Ag decorated catalysts for formic acid decomposition, it is found that all ratios result in a promotion over Pd-PVP, but the Pd-PVP+Ag 1:0.075 catalyst displays a lower initial activity than the higher ratio catalysts (which are all constant). This

indicates increased electronic donation at higher Ag ratios, in contrast with the FTIR results. The deactivation observed over two hours is quite constant for all Pd-PVP+Ag samples; a small decrease is observed compared to undecorated Pd-PVP, indicative of random Ag deposition blocking some of the low coordinate Pd sites. As deactivation does not continue to decrease with higher ratios of Ag, deposition appears to shift from random coverage of the surface to the formation of clusters which do not cover much more of the surface. The lower activity of Pd-PVP+Ag 1:0.075, as compared to the other Ag decorated catalysts, appears to be due to a slightly lower degree of electronic promotion, from the small amount of Ag on the Pd surface, which cannot be identified by FTIR.

6.4.4 Silver decorated supported palladium

Whilst alloys and core-shell structures of Pd and Ag have been widely reported to show an increased activity over monometallic Pd, the highest activity heterogeneous catalysts all involve supported metal nanoparticles with no stabilising polymer. The ability of Ag decoration to modify the activity of a supported Pd on carbon catalyst was thus examined. A Pd/C catalyst was synthesised using a precipitation-deposition method; first, $Pd(NO_3)_2$ and Norit GSX carbon were dispersed in water and thoroughly mixed before adjusting to pH 11 with NaOH, precipitating insoluble $Pd(OH)_2$ onto the support.[35] Then, in contrast to a number of similar methods, hydrogen was directly bubbled through the solution to reduce the $Pd(OH)_2$.

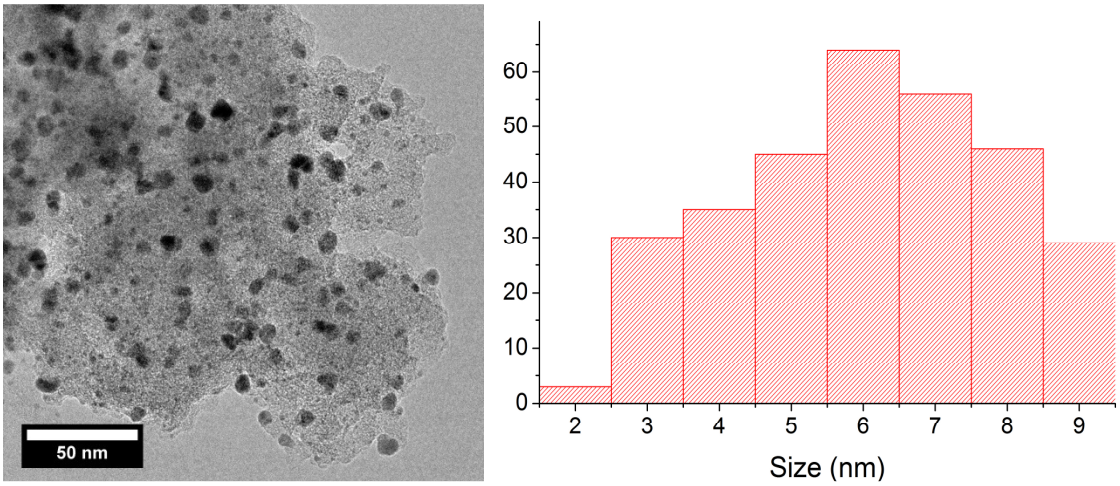


Figure 6.15– TEM micrograph and size distribution histogram of 10% Pd/C

The prepared Pd/C was characterised by TEM, XRD and CO chemisorption. The size from TEM, figure 6.15, was found to be 5.8 nm in good agreement with XRD that gave 5.5 nm. The dispersion and size distribution of the particles were not quite as good as Type 87L, used in chapter 4, but the performance for formic acid decomposition (detailed below) is very similar. From CO chemisorption the surface area was found to be 76 m^2 $g(Pd)^{-1}$, giving a calculated particle size of 5.5 nm. Whilst the details of Type 87L synthesis are unknown due to its commercial nature, the slow reduction of the synthesised Pd/C was used to produce particles with more thermodynamically stable surfaces, as we demonstrated this was a favourable feature of colloidal Pd-PVP particles in chapter 4. The larger size of the synthesised Pd/C (5.5 nm) should result in a larger proportion of terrace sites than for the Pd-PVP particles (3.2nm). Whilst the shape of the synthesised Pd/C catalyst was less controlled than that of the Pd-PVP particles, assuming a cubo-octahedral shape and using the model of van Hardeveld and Hartog the proportion of corner, edge, and terrace atoms was 1.6%, 14.7%, and 83.7% of the surface and 0.4%, 3.4%, and 19.7% of the total atoms in the particle.[19] The dispersion of the catalyst was 17% measured by CO chemisorption, in reasonable agreement with 23.5% of atoms on the nanoparticle surface predicted from the model.

The activity of the synthesised Pd/C is very similar to that of Type 87L used in chapter 4, with total gas productions of 26.6 L $g(Pd)^{-1}$ and 27.1 L $g(Pd)^{-1}$ resulting in TOFs of 185 h^{-1} and 169 h^{-1}, respectively.

The synthesised Pd/C was decorated with Ag using a similar method to that used for the colloidal particles; initial hydrogen treatment was followed by the addition of the decorating metal salt and a final reduction step. The final reduction step was performed by drop-wise addition of a N_2H_4 solution. The decorated catalyst was then filtered, extensively washed with water and dried at 85°C in air. The decorated Pd/C+Ag catalysts were characterised by XRD to determine if decoration had occurred.

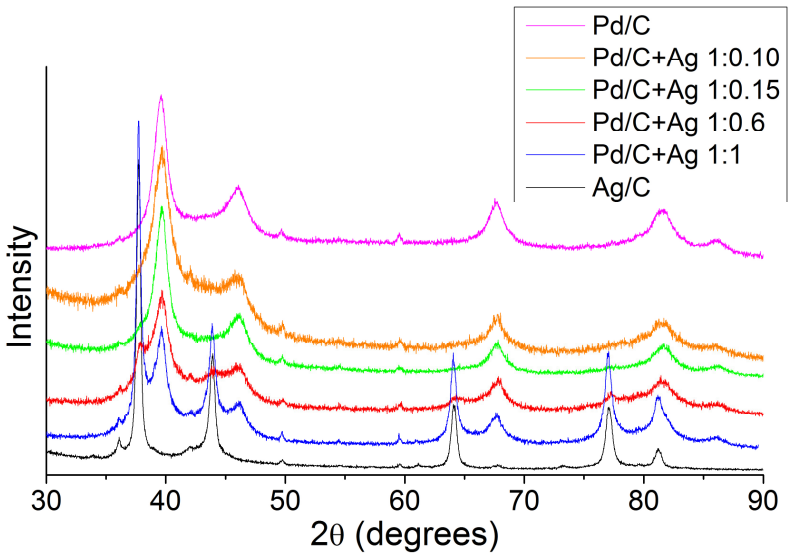


Figure 6.16– XRD pattern of Pd/C, Ag/C and Pd/C decorated with various ratios of Ag

Figure 6.16 shows the x-ray diffraction patterns of the Ag decorated Pd/C. At higher ratios of Ag, a separate Ag phase is clearly observed which matches that of a commercial Ag/C sample. The formation of Ag particles was not observed for the colloidal particles and is likely due to the higher surface coverages, preventing all of the Ag from being sacrificially reduced on to the Pd surface. The instability of Ag nanoparticles on carbon would also mean

that any Ag reduced onto the carbon support rather than the Pd surface will undergo growth to form large particles with a lower surface energy, making them more visible by XRD.[36] The position of the Pd(111), and where present Ag(111), peak was examined to identify if any alloy formation had occurred.

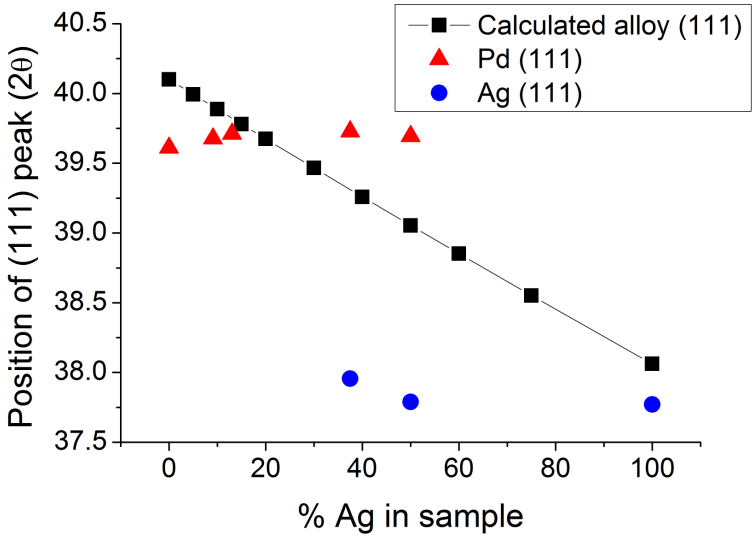


Figure 6.17– Position of Pd(111) peak of Pd/C+Ag particles, Ag(111) peak where present and calculated PdAg alloy (111)

In figure 6.17, no significant shift in Pd (111) or Ag (111) peak is observed for any of the ratios tested, the small variations are attributed to either incomplete removal of β-H from Pd or to instrument effects. The lack of observed shift is in stark contrast to the substantial shift of the Pd (111) peak in colloidal particles, attributed to strain induced by Ag on the surface. The contrast between Pd-PVP and Pd/C is attributed to the larger particles of Pd/C, with much lower surface to volume ratio, being less susceptible to distortion from surface strain effects. Strain effects are reduced with increasing distance from the strain-inducing interface, so the bulk of the larger particles will experience less distortion.[30] As we will see, the activity increase is still observed with Ag decoration of Pd/C, indicating that strain is not the cause of increased activity of the Pd-PVP particles.

As FTIR of adsorbed CO could not be performed on the supported catalysts, identification of site specific deposition and electronic modification could not be quantified. To ensure that there was an interaction between Pd and Ag, the catalysts were probed using XPS, figure 6.18 displays the spectra of Pd/C and Pd/C+Ag 1:0.60.

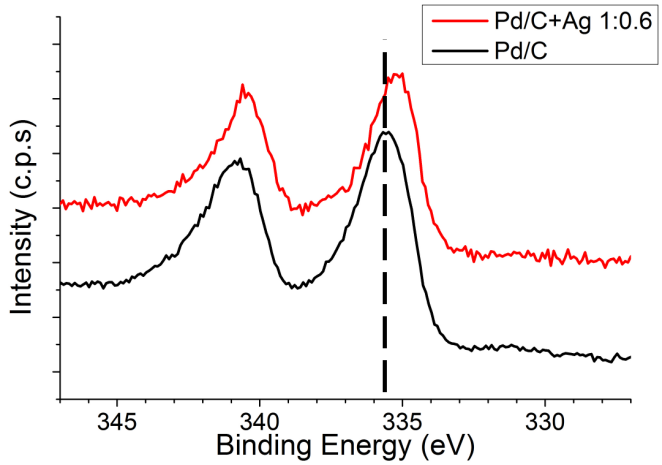


Figure 6.18– XPS spectra of Pd 3d region of Pd/C and Ag decorated Pd/C

In both samples the Pd $3d_{5/2}$ peak consists of two components attributed to Pd and oxidised Pd, with approximately 35% of Pd in an oxidised state. After Ag decoration with a 1:0.60 ratio of Pd to Ag, the Pd $3d_{5/2}$ peak is shifted by 0.4 eV to a lower binding energy, indicative of an increase in electron density on the Pd. This demonstrates that there is an interaction between Ag and Pd, suggesting that whilst no shift is observed in the Pd (111) peak by XRD, the Ag is decorating the Pd particles and the lack of Pd (111) peak shift is due to the greatly reduced strain effects on larger particles. As the decorated structure of the supported Pd/C+Ag particles has been confirmed, they were tested for formic acid decomposition and results are displayed in figure 6.19 and table 3.

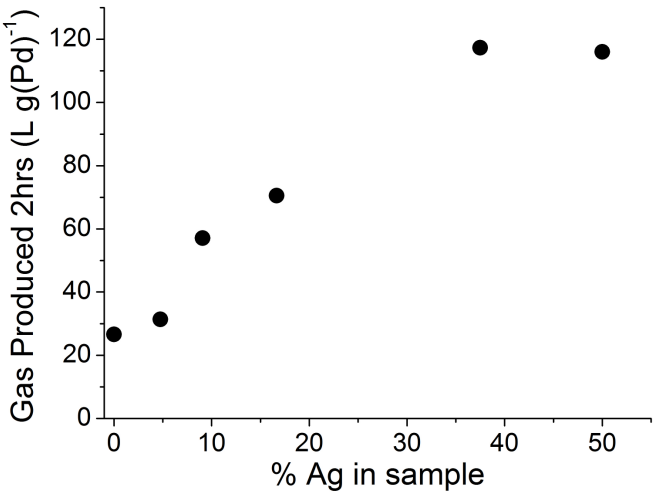


Figure 6.19– Total gas production over 2 hours for Pd/C decorated with various ratios of Ag. 4.25 mg of Pd in 10.575 mL of 1.4 M formic acid stirred at 25°C

As was seen with the decorated Pd-PVP particles, Ag greatly promotes formic acid decomposition activity and from comparison of figures 6.14 and 6.19 a similar trend between gas production and Ag content is also evident for Ag decorated Pd/C catalysts. However, the point at which maximum activity is achieved is at a much higher ratio for Pd/C+Ag (1:0.60) than in the case of Pd-PVP+Ag (1:0.15); it would be expected that the optimum coverage of the larger supported particles would require a lower ratio of Ag. The discrepancy between the optimum ratio of Pd to Ag on Pd-PVP and on Pd/C, and the identification of Ag peaks from XRD, clearly indicate that Ag is not depositing exclusively onto the Pd surface. As such, a higher ratio of Ag is required for the Pd/C to achieve a level of surface decoration equivalent to the optimum for the Pd-PVP particles.

Table 3 – Formic acid decomposition activity of Pd/C nanoparticles decorated with various ratios of Ag and an alloyed 1:1 PdAg/C catalyst

Catalyst	Theoretical surface coverage	Initial Rate[a] (L g(Pd)$^{-1}$ min^{-1})	Final Rate[b] (L g(Pd)$^{-1}$ min^{-1})	Deactivation[c]	Total Gas[d] (L g(Pd)$^{-1}$)
Pd/C	N/A	0.5454	0.1058	5.15	26.56
Pd/C+Ag 1:0.05	21%	0.6353	0.1623	3.91	31.34
Pd/C+Ag 1:0.10	42%	1.2049	0.2612	4.61	57.11
Pd/C+Ag 1:0.20	85%	1.4480	0.3089	4.69	70.50
Pd/C+Ag 1:0.6	255%	2.1031	0.4033	5.21	117.3
Pd/C+Ag 1:1	425%	2.1528	0.5176	4.16	116.0
Pd/C+Ag 1:5	2100%	0.5108	0.1682	3.04	34.24
PdAg/C 1:1 Alloy	N/A	1.4134	0.3337	4.24	70.25

[a]Rate of gas production in the first 10 min; [b]Rate of gas production in the final 20 min; [c]Deactivation calculated from initial rate divided by final rate; [d]Total Gas produced in 2 hours (4.25 mg of Pd in 10.575 mL of 1.4 M formic acid stirred at 25^{o}C)

From table 3 the increase in activity upon Ag decoration is again clear, but the gradual increase in initial rate for the ratios of 1:0.05 to 1:0.60 is in stark contrast to the results of Pd-PVP+Ag. All Ag decorated Pd-PVP samples had a similar initial rate as a result of the constant level of electronic donation, observed by FTIR of chemisorbed CO. The increase in initial activity with higher ratios of Ag for decorated Pd/C catalysts suggests an increasing degree of electronic modification, promoting the rate determining C-H cleavage step of formic acid dehydrogenation. This increase in electronic modification with increasing Ag for decorated Pd/C, is likely a result from Ag particle formation (observed by XRD figure 6.16) lowering the actual Ag coverage of the Pd particles. The amount of decorating Ag will therefore be below that expected from the specified ratios and below that of colloidal particles

decorated with similar ratios. Thus, the surface of the supported Pd is not all electronically promoted until a high ratio of Pd to Ag is used, and a surface coverage similar to that in the decorated Pd-PVP particles is achieved. At which point the entire surface is electronically modified and further increases of Pd to Ag ratio do not promote activity.

The decrease in deactivation is again attributed to the random deposition of Ag onto the Pd surface, blocking some of low the coordinate sites. At very high Pd to Ag ratios (1:5) almost complete coverage of the Pd surface is expected, thus the dramatic decrease in activity is assigned to the loss in Pd surface area. The requirement for a very high ratio, enough for more than 20 times monolayer surface coverage, before a decrease in activity is observed highlights two factors. Firstly, that Ag decoration forms clusters rather than a monolayer, otherwise total surface coverage would be observed with much lower ratios (<1:0.60). Secondly, that even though formation of separate Ag particles occurs, growth of the Ag clusters on the Pd surface continues with increasing Ag ratios.

Comparison of the activity of decorated particles for formic acid decomposition with that of a PdAg 1:1 alloy on carbon, synthesised by co-reduction, highlights the benefits of decoration over the widely used approach of alloying. The decorated particles, with a 1:1 ratio of Pd to Ag, results in almost a 50% increase in initial activity and a similar improvement in the overall gas production over the alloy. Exploring the proposed mechanism of formic acid dehydrogenation gives an insight into the reasons for the improved activity of the decorated particles. Whilst the alloyed structure is expected to result in maximum electronic modification of the Pd (due to the high degree of atomic mixing), it also breaks up the Pd atoms on the particle surface. The proposed intermediate of the dehydrogenation mechanism, a bridging formate species, requires two adjacent Pd atoms. Thus, an alloy structure will

greatly reduce the number of sites available to perform this reaction, whereas decoration with Ag clusters blocks some surface sites but leaves many Pd-Pd sites free to form active sites. The requirement for two adjacent Pd atoms may explain the recent results of Sun *et al.* who found that, for small AgPd alloy particles, the optimum catalyst was $Ag_{42}Pd_{58}$/C.[4] The Pd-rich nature of their catalyst clearly increases the probability of adjacent Pd atoms.

Turnover frequencies cannot be accurately determined due to both Pd and Ag adsorbing CO, preventing an accurate measurement of the active surface area (uncovered Pd) using pulse CO chemisorption. Using the Pd surface area of the initial undecorated Pd/C as the number of active sites, a representative TOF can be calculated. Whilst this value is an underestimation, due to a fraction of the Pd surface area covered with inert Ag, a TOF of 816 h^{-1} is calculated for the Pd/C+Ag 1:0.60 catalyst. This TOF is higher than most other PdAg catalysts even operating at elevated temperatures.[4,5]

6.5 Conclusion

In conclusion, three distinct effects of metal decoration on Pd nanoparticles have been observed. Firstly, through site selective deposition of Bi, blockage of the low coordinate sites has been achieved. This was confirmed by the loss of the linear CO peak in CO FTIR that is attributed to adsorption of CO on the low coordinate sites. The selective blockage of these sites prevented the dehydration of formic acid and thus the associated CO production. As such, poisoning of the catalyst was reduced and less deactivation was observed. Secondly the inverse effect was observed, Te decoration selectively covered terrace sites competing with the active sites for the dehydrogenation of formic acid. Thus, the Te decorated catalyst showed very little activity for formic acid decomposition. Finally, Ag decoration was not site

selective but the high degree of electronic promotion easily overcame the lost Pd surface area, which resulted in catalysts highly active for formic acid decomposition. Figure 6.20 gives an illustrative representation of the three cases of metal deposition.

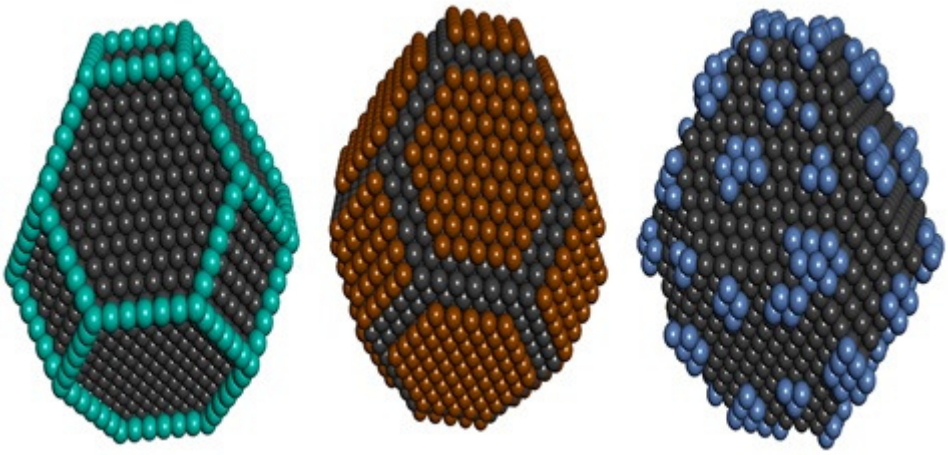


Figure 6.20– Illustration of Pd particles decorated with Bi, Te and Ag (left to right)

After optimisation of the Ag modified supported Pd catalyst, it is found that the activity can be increased over four times. The most active catalyst show a higher TOF than a range of PdAg alloy catalysts even when operating at elevated temperatures, demonstrating that decoration maybe a preferred method for the production of highly active Pd catalysts.

It has been demonstrated that decoration of preformed nanoparticle catalysts provides an effective method for the tuning of both the geometric and electronic properties of the existing metal surface. Through the optimisation of a catalysts' surface properties with the high degree of control offered by this technique, significant modifications in catalyst activities and selectivities are expected for a wide range of reactions that occur preferentially on specific surfaces.

6.6 References

[1] E. Antolini, *Materials Chemistry and Physics* **2003**, *78*, 563–573.

[2] M. B. Boucher, B. Zugic, G. Cladaras, J. Kammert, M. D. Marcinkowski, T. J. Lawton, E. C. H. Sykes, M. Flytzani-Stephanopoulos, *Physical Chemistry Chemical Physics: PCCP* **2013**, *15*, 12187–12196.

[3] S. K. Singh, Q. Xu, *Inorganic Chemistry* **2010**, *49*, 6148–6152.

[4] S. Zhang, Ö. Metin, D. Su, S. Sun, *Angewandte Chemie International Edition* **2013**, *52*, 3681–3684.

[5] X. Zhou, Y. Huang, W. Xing, C. Liu, J. Liao, T. Lu, *Chemical Communications* **2008**, 3540–3542.

[6] X. Guo, Q. Zhang, Y. Sun, Q. Zhao, J. Yang, *ACS Nano* **2012**, *6*, 1165–1175.

[7] C. Wang, H. Daimon, S. Sun, *Nano Letters* **2009**, *9*, 1493–1496.

[8] K. Tedsree, C. W. A. Chan, S. Jones, Q. Cuan, W.-K. Li, X.-Q. Gong, S. C. E. Tsang, *Science (New York, N.Y.)* **2011**, *332*, 224–228.

[9] S. Alayoglu, A. U. Nilekar, M. Mavrikakis, B. Eichhorn, *Nature Materials* **2008**, *7*, 333–338.

[10] T. Hartung, J. Willsau, J. Heitbaum, *Journal of Electroanalytical Chemistry and Interfacial Electrochemistry* **1986**, *205*, 135–149.

[11] D. Wang, H. L. Xin, Y. Yu, H. Wang, E. Rus, D. A. Muller, H. D. Abruña, *Journal of the American Chemical Society* **2010**, *132*, 17664–17666.

[12] S. C. Tsang, N. Cailuo, W. Oduro, A. T. S. Kong, L. Clifton, K. M. K. Yu, B. Thiebaut, J. Cookson, P. Bishop, *ACS Nano* **2008**, *2*, 2547–2553.

[13] J. Clavilier, J. Feliu, A. Aldaz, *Journal of Electroanalytical Chemistry and Interfacial Electrochemistry* **1988**, *243*, 419–433.

[14] J. Anderson, J. Mellor, R. Wells, *Journal of Catalysis* **2009**, *261*, 208–216.

[15] J. L. Haan, K. M. Stafford, R. I. Masel, *The Journal of Physical Chemistry C* **2010**, *114*, 11665–11672.

[16] G. A. Somorjai, *Journal of Catalysis* **1972**, *27*, 453–456.

[17] F. Gauthard, F. Epron, J. Barbier, *Journal of Catalysis* **2003**, *220*, 182–191.

[18] F. Bonet, V. Delmas, S. Grugeon, R. Herrera Urbina, P.-Y. Silvert, K. Tekaia-Elhsissen, *Nanostructured Materials* **1999**, *11*, 1277–1284.

[19] R. Van Hardeveld, F. Hartog, *Surface Science* **1969**, *15*, 189–230.

[20] M. Yadav, T. Akita, N. Tsumori, Q. Xu, *Journal of Materials Chemistry* **2012**, *22*, 12582–12586.

[21] Q.-Y. Bi, X.-L. Du, Y.-M. Liu, Y. Cao, H.-Y. He, K.-N. Fan, *Journal of the American Chemical Society* **2012**, *134*, 8926–8933.

[22] H. B. Michaelson, *Journal of Applied Physics* **1977**, *48*, 4729–4733.

[23] N. L. Pacioni, V. Filippenko, N. Presseau, J. C. Scaiano, *Dalton Transactions* **2013**, *42*, 5832–5838.

[24] M. K. Schröter, L. Khodeir, J. Hambrock, E. Löffler, M. Muhler, R. A. Fischer, *Langmuir* **2004**, *20*, 9453–9455.

[25] K. Tedsree, T. Li, S. Jones, C. W. A. Chan, K. M. K. Yu, P. A. J. Bagot, E. A. Marquis, G. D. W. Smith, S. C. E. Tsang, *Nature Nanotechnology* **2011**, *6*, 302–307.

[26] K. W. Zilm, L. Bonneviot, G. L. Haller, O. H. Han, M. Kermarec, *The Journal of Physical Chemistry* **1990**, *94*, 8495–8498.

[27] J. H. Ryu, S. S. Han, D. H. Kim, G. Henkelman, H. M. Lee, *ACS Nano* **2011**, *5*, 8515–8522.

[28] L. A. Olsen, J. López-Solano, A. García, T. Balić-Žunić, E. Makovicky, *Journal of Solid State Chemistry* **2010**, *183*, 2133–2143.

[29] S. M. Fairclough, E. J. Tyrrell, D. M. Graham, P. J. B. Lunt, S. J. O. Hardman, A. Pietzsch, F. Hennies, J. Moghal, W. R. Flavell, A. A. R. Watt, et al., *The Journal of Physical Chemistry C* **2012**, *116*, 26898–26907.

[30] P. Strasser, S. Koh, T. Anniyev, J. Greeley, K. More, C. Yu, Z. Liu, S. Kaya, D. Nordlund, H. Ogasawara, et al., *Nature Chemistry* **2010**, *2*, 454–460.

[31] M. Wenkin, P. Ruiz, B. Delmon, M. Devillers, *Journal of Molecular Catalysis A: Chemical* **2002**, *180*, 141–159.

[32] A. Ruban, H. Skriver, J. Nørskov, *Physical Review B* **1999**, *59*, 15990–16000.

[33] A. M. Smith, A. M. Mohs, S. Nie, *Nature Nanotechnology* **2009**, *4*, 56–63.

[34] A. Cabiac, T. Cacciaguerra, P. Trens, R. Durand, G. Delahay, A. Medevielle, D. Plée, B. Coq, *Applied Catalysis A: General* **2008**, *340*, 229–235.

[35] H. Cho, J. Park, B. Hong, Y. Park, *Bulletin of the Korean Chemical Society* **2008**, *29*, 328–334.

[36] J. Li, Y. Lin, B. Zhao, *Journal of Nanoparticle Research* **2002**, *4*, 345–349.

Chapter 7

Conclusions and Future Perspectives

Chapter 7 Conclusions and Future Perspectives..... 208

7.1 Conclusions..... 209

7.2 Future perspectives 210

7.3 References..... 211

7.1 Conclusions

Within this thesis, a range of methods have been developed to tune the geometric and electronic properties of Pd nanoparticles. These modifications show a dramatic impact on the activity and/or selectivity of Pd particles for the catalytic decomposition of formic acid to H_2 and CO_2, achieving some of the highest TOF's reported for heterogeneous catalysts at room temperature. The modification of preformed nanoparticles has been demonstrated with both organic and inorganic modifiers with common promotion mechanisms observed in both situations.

Organic modification of Pd particles using polymers and functional groups bound to the surface of the catalyst support has been demonstrated, through a range of characterisation methods, to result in electronic donation for all functional groups tested with maximum electronic effects observed with amine groups. Additionally, amines (particularly tertiary amines) showed a preference for selective blockage of low coordinate sites on Pd particle surfaces, which reduced catalyst poisoning by preventing the formation of CO from the unfavourable dehydration of formic acid.

For inorganic modification, through the decoration of Pd nanoparticles with sub-monolayers of a decorating metal, both donation and withdrawing electronic effects were observed on Pd correlating with the relative values of the work functions of the metals in agreement with previous reports of bimetallic particles.[1] Selective decoration of low coordinate sites was also observed in the case of Bi decoration, with the optimum activity occurring with ratios of Bi that correlated with the calculated fraction of low coordinate sites on a model Pd particle. The site selective decoration observed with Bi is proposed to be a consequence of its stereochemical lone pair, which favours binding on low coordinate sites in a similar manor to

that of the N lone pair in amines which was observed experimentally in this work and demonstrated computationally by Ryu *et al*.[2]

7.2 Future perspectives

Whilst modification of metal nanoparticles through alloying or changing the support are widespread techniques to alter the metals properties for a specific reaction, the methods presented in this thesis provide a range of highly selective techniques to tune the properties of the modified nanoparticles. The limitation of these techniques to moderate conditions, in order to prevent alloy formation or decomposition of the organic groups, is expected to be of reduced importance as interest in greener chemical processes using less energy increases.

The activity difference of different catalyst surface sites and their resulting abilities to promote different reaction pathways is widely reported for numerous reactions, resulting in substantial effects on catalyst selectivities. Thus modification methods selectively blocking specific surface sites have a vast range of potentially applicable reactions and the ability to modify preformed catalysts makes these methods ideal to easily enhance existing catalytic systems.

Additionally, the high activities and selectivities for formic acid dehydrogenation of some of the catalysts reported in this thesis, under ambient conditions, may highlight the potential ability of formic acid as a hydrogen storage material for small portable devices. Whilst significant advances are still required for the practical application of formic acid as a hydrogen storage material, the demonstrated effectiveness of the methods displayed in this thesis may provide potential techniques for further catalyst development.

7.3 References

[1] K. Tedsree, C. W. A. Chan, S. Jones, Q. Cuan, W.-K. Li, X.-Q. Gong, S. C. E. Tsang, *Science (New York, N.Y.)* **2011**, *332*, 224–228.

[2] J. H. Ryu, S. S. Han, D. H. Kim, G. Henkelman, H. M. Lee, *ACS Nano* **2011**, *5*, 8515–8522.